

T-4242

**APPLICATION OF MULTICOMPONENT VSP'S TO RESERVOIR
CHARACTERIZATION AT CEDAR HILL COAL BED METHANE FIELD,
SAN JUAN COUNTY, NEW MEXICO**

by

Gary T. Molinero

ProQuest Number: 10783830

All rights reserved

INFORMATION TO ALL USERS

The quality of this reproduction is dependent upon the quality of the copy submitted.

In the unlikely event that the author did not send a complete manuscript and there are missing pages, these will be noted. Also, if material had to be removed, a note will indicate the deletion.



ProQuest 10783830

Published by ProQuest LLC (2018). Copyright of the Dissertation is held by the Author.

All rights reserved.

This work is protected against unauthorized copying under Title 17, United States Code
Microform Edition © ProQuest LLC.

ProQuest LLC.
789 East Eisenhower Parkway
P.O. Box 1346
Ann Arbor, MI 48106 – 1346


T-4242

A thesis submitted to the Faculty and the Board of Trustees of the Colorado School of Mines in partial fulfillment of the requirements for the degree of Master of Science (Geophysics).

Golden, Colorado

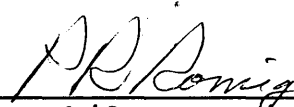
Date 4/8/92

Signed: 
Gary T. Molinero

Approved: 
Dr. Tom L. Davis
Thesis Advisor

Golden, Colorado

Date 8 April 1992


Dr. Phil R. Romig
Professor and Head,
Department of Geophysics

ABSTRACT

A set of near-offset Vertical Seismic Profiles (VSPs) (including one vertical P-wave vibrator source and two orthogonal horizontally polarized S-wave vibrator sources) and one far-offset vertical P-wave vibrator source all recorded into a multicomponent receiver sonde were conducted in the Hamilton #3 well, Cedar Hill Area, New Mexico. Three components of ground motion (vertical and two horizontal) were recorded by Schlumberger's five shuttle multicomponent VSP tool for each of the sources. A total of twelve wavefields were acquired. The purpose of the near-offset was to observe shear-wave birefringence caused by anisotropy above and within the coal bed methane formations, thus determining an open fracture orientation within the coals. The far-offset was used to orient the VSP tool and examine the continuity of the coal beds within the vicinity of the well. The VSPs were also used in planning a 3-D multicomponent survey in the Cedar Hill Field and then tying the major coal reflectors into the processed survey.

Two major coal beds identified on the high resolution density log, cumulative thickness greater than 16 feet, were observed on the near-offset P-wave corridor stack. Both coal intervals are producing zones in the Cedar Hill Field. Also,

there is a good correlation between the VSP and surface seismic data recorded in the area.

Four component rotation of the near-offset shear-wave data was necessary to place the data into its natural coordinate system. This process determined an open fracture orientation of 319 degrees from North or N41W. In comparing these results with a core analysis from the Hamilton #3 well (GRI/REI report, 1989), the polarization angle is parallel to the butt cleats in the coals.

To determine if there was a change in polarization direction with depth, layer stripping was applied to the near-offset shear-wave data. The results showed that the fracturing in the coals is at the same orientation as the fracturing detected at the near-surface.

The fast(S1) and slow(S2) shear wave corridor stacks showed a two-way time delay of approximately 20 msec at the coals. The S2 corridor stack has a slightly higher amplitude than the S1 corridor stack, due to differences in reflection coefficients. In the interpretation of the 3-D multicomponent survey, amplitude difference in the S2 versus S1 components could prove to be a useful in determining fracture density in the coal beds.

The results of processing the far-offset P-wave source data showed that the converted shear-wave data were of higher resolution in the coals beds than the upgoing P-wave data. A

slight dip in the coals is seen both on the far-offset VSP data and on the surface seismic data, possibly caused by draping of the coals over underlying channel sandstones.

The multicomponent VSPs were successful in determining an open fracture orientation parallel to the butt cleats and in evaluating the coal bed formations such as reflection and amplitude characteristics. By knowing this information, better enhanced recovery programs can be developed in the future.

TABLE OF CONTENTS

	Page
ABSTRACT.....	ii
LIST OF FIGURES.....	v
LIST OF TABLES.....	x
ACKNOWLEDGEMENTS.....	xi
INTRODUCTION.....	1
GEOLOGIC SUMMARY.....	5
BACKGROUND PRINCIPLES.....	10
VSP SURVEY.....	15
Acquisition.....	15
Preprocessing.....	18
NEAR-OFFSET COMPRESSIONAL VSP.....	19
TOOL ORIENTATION.....	30
NEAR-OFFSET SHEAR-WAVE VSPs.....	38
Birefringence.....	49
LayerStripping.....	54
Processing of fast- and slow- shear-wave data.....	56
BIREFRINGENCE AND GEOLOGY.....	65
FAR-OFFSET COMPRESSIONAL VSP.....	72
FUTURE STUDIES.....	94
CONCLUSIONS.....	95
REFERENCES.....	97

LIST OF FIGURES

	Page
1. Location map, Cedar Hill Field, New Mexico. (modified from GRI Report, 1989).....	3
2. High resolution density log showing coal intervals 1 and 2. (GRI report, 1989).....	6
3. High resolution density log showing coal interval 3. (GRI Report, 1989).....	7
4. High density resolution log showing coal interval 4, the basal Fruitland Formation. (GRI Report, 1989).....	8
5. Azimuthally anisotropic medium with a horizontal axis of symmetry. (after Kramer, 1991).....	11
6. Shear-wave splitting (birefringence) generated by a shear-wave entering an azimuthally anisotropic medium. (after Kramer, 1991).....	12
7. Phase velocities for compressional(qP), fast shear (qSR), and slow shear(qSP) waves propagating through a transversely isotropic medium. (White and Sengbush, 1983).....	14
8. Source locations with respect to the Hamilton #3 well. (after Kramer, 1991).....	16
9. Vertical (Z) component from the near-offset P-wave data.....	20
10. Down-going compressional data acquired through medianfiltering.....	21
11. Up-going compressional energy after subtraction of the down-going energy from the pre-median filtered data.....	23
12. Results of the down-going energy after applying the 10(24) - 100(36) Hz (dB/Oct) wavelet shaping filter to collapse the multiples.....	24

	Page
13. Results of the up-going energy after applying the 10(24) - 100(36) Hz (dB/Oct) wavelet shaping filter designed on the down-going energy.....	25
14. Unstacked and corridor stacked compressional data with a 10(24) - 90(36) Hz(dB/oct) bandpass filter.....	26
15. East-West line from the surface 3-D multicomponent seismic survey showing a tie with the near-offset compressional VSP corridor stack.....	28
16. North-South line from the surface 3-D multicomponent seismic survey showing a tie with the near-offset compressional VSP corridor stack.....	29
17. Horizontal (X) component from the far-offset P-wave data.....	32
18. Horizontal (Y) component from the far-offset P-wave data.....	33
19. Vertical (Z) component from the far-offset P-wave data.....	34
20. Azimuthal tool orientation angles (from true North) found through hodogram analysis of the for-offset P-wave X and Y data sets.....	35
21. Horizontal far-offset P-wave component oriented inline to the source receiver plane.....	36
22. Horizontal far-offset P-wave component oriented transverse to the source receiver plane. (contains SH energy generated from the P-wave source).....	37
23. Horizontal (X) component from the near-offset radial shear-wavedata.....	39
24. Horizontal (Y) component from the near-offset radial shear-wavedata.....	40
25. Vertical (Z) component from the near-offset radial shear-wavedata.....	41
26. Horizontal near-offset radial shear-wave component oriented inline to the source receiver plane.....	42

	Page
27. Horizontal near-offset radial shear-wave component oriented transverse to the source receiver plane.....	43
28. Horizontal (X) component from the near-offset transverse shear-wave data.....	44
29. Horizontal (Y) component from the near-offset transverse shear-wave data.....	45
30. Vertical (Z) component from the near-offset transverse shear-wave data.....	46
31. Horizontal near-offset transverse shear-wave component oriented inline to the source receiver plane.....	47
32. Horizontal near-offset transverse shear-wave component oriented transverse to the source receiver plane.....	48
33. Results after four component rotation of the near-offset shear-wave data.....	51
34. Azimuthal polarization angle (relative to the source-receiver plane) of the fast shear-wave (upper curve) and the time delay between the fast and slow shear-waves (lower curve).....	53
35. The layer stripping rationale used to determine a change in natural polarization direction with depth (after Winterstein and Meadows, 1990).....	55
36. Results of the near-offset shear-wave components after four component rotation using a polarization angle of 56 degrees.....	57
37. Azimuthal polarization angle (relative to the source-receiver plane) of the fast shear-wave (upper curve) and time delay between the fast and slow shear-waves (lower curve) after layer stripping the first 2630 feet and removing 10 ms time delay.....	58
38. Processing flow for near-offset fast and slow shear-wavedata.....	60
39. Unstacked and corridor stacked fast shear-wave data with a 10(124) - 50(36) Hz(dB/oct) bandpass filter....	61
40. Unstacked and corridor stacked slow shear-wave data with a 10(124) - 50(36) Hz(dB/oct) bandpass filter....	62

	Page
41. Comparison of the fast and slow shear-wave data in the coal interval.....	63
42. Results of subtracting the fast shear-wave data from the slow shear-wave data to show the amplitude difference.....	64
43. Rose diagram showing cleat orientation from core analysis and polarization angle from the VSP (modified from the GRI Report, 1989).....	66
44. Focal mechanisms of earthquakes in the Colorado Plateau, New Mexico. Solid circles are compressional; open circles are dilatational first motions. (after Humphrey and Wong, 1989).....	68
45. Gas production map in Cedar Hills area indicating the natural polarization within the coals. (modified from Mavor et.al., 1989).....	69
46. Structure map of the base of coal interval 4 in Cedar Hills indicating the natural polarization angle within the coals (modified from Johnson, 1991).....	71
47. Vertical incidence angles found through hodogram analysis of the far-offset P-wave inline (OHPF) and vertical (Z) components.....	73
48. Particle motions for downgoing waves after corrected tool orientations. (after Kramer, 1991).....	74
49. Vertical far-offset P-wave component oriented inline to the source receiver plane.....	76
50. Vertical far-offset P-wave component oriented transverse to the source receiver plane.....	77
51. Down-going compressional data computed by median filtering of the inline component (OVPF).....	78
52. Down-going SV data computed by median filtering of the crossline component (TVPF).....	79
53. Results after subtraction of the down-going P-wave energy from the pre-median filtered OVPF data.....	80
54. Results after subtraction of the down-going SV energy from the pre-median filtered TVPF data.....	81

	Page
55. Up-going compressional energy after time-variant orientation.....	83
56. Up-going SV energy after time-variant orientation.....	84
57. Results of the down-going energy after applying the 10(24) - 100(36) Hz (dB/Oct) wavelet shaping filter to collapse the multiples.....	87
58. Results of the up-going P-wave energy after applying the 10(24) - 100(36) Hz (dB/Oct) wavelet shaping filter designed on the down-going energy.....	88
59. Results of the up-going SV-wave energy after applying the 10(24) - 100(36) Hz (dB/Oct) wavelet shaping filter designed on the down-going energy.....	89
60. Results of the P-wave data after NMO correction and medianfiltering.....	90
61. Results of the SV data after NMO correction and medianfiltering.....	91
62. Final results of the P-wave data after horizontal moveoutcorrection.....	92
63. Final results of the converted S-wave data after horizontal moveout correction.....	93

LIST OF TABLES

	Page
Table I. Number of vibrator sweeps per receiver depth for each source location in the Cedar Hills VSP..	17
Table II. Velocity model used for the raytracing program in order to calculated the time variant angles...	82

ACKNOWLEDGEMENTS

I greatly appreciate the guidance and assistance I have received throughout my graduate program, especially:

Dr. Tom Davis, my thesis advisor, who provided the framework and guidance of my research. My committee members, Dr. Guy Towle and Dr. Andy Andersen, gave considerable amount of encouragement and advice.

Ted Shuck, graduate student, wrote Halliburton Geophysical Services' VSP software used in data processing. Ted was extremely helpful in every step of the way, both in processing and interpreting the VSP. In addition, Bob Benson gave helpful insight throughout the project.

The Colorado School of Mines Reservoir Characterization Project provided the funding for the research. The main contributors are as follows:

Advance Geophysical

AGIP

AMOCO

ARI Advanced Resources International Inc.

Canadian Hunter

Chinese Petroleum Corporation

CGG American Services Inc.

CNG Producing Company

Conoco

Elf Aquitaine
Exxon
Gas Research Institute
Golden Geophysical, Inc.
Halliburton Geophysical Services
INTEVEP, S.A.
Japan National Oil Corp.
Japan Petroleum Exploration Co. Ltd.
Marathon Oil Co.
Meridan Oil Co.
Mesa Limited Operation Partnership
Norcen Energy
Northern Geophysical of America
ORYX Energy Co.
Resource Enterprises, Inc.
Schlumberger Well Services
Texaco Inc.
Transworld Energy International
Union Pacific Resources Inc.
UNOCAL

Finally, I wish to express my deepest appreciation to my parents, Morris and Doris, whose encouragement and support have always been there in the pursuit of my goals.

INTRODUCTION

Due to government incentives and a need for a cleaner burning fuel, coal bed methane is an increasingly important resource. A crucial controlling factor in commercial coalbed methane reservoirs is fracture permeability (GRI/REI report, 1989). In the past, permeability determination has been a major problem. However, in the past decade shear-wave technology has proven to be a useful tool in determining permeability trends in fractured reservoirs. As a shear-wave propagates into a vertically fractured medium, splitting occurs into two shear-waves; one parallel to fracture orientation and one perpendicular to fracture direction (Crampin, 1985). This is known as shear-wave splitting or birefringence. Due to vertical fracturing in the coal beds, the intent of the Reservoir Characterization Project at Colorado School of Mines is to determine permeability direction and fracture intensity using shear-wave technology.

The study area is the Cedar Hill Field in New Mexico. The field, operated by Amoco Production Company, is located in the northwestern portion of San Juan basin (Figure 1) and has produced methane since 1977. In the producing coal zone (basal Fruitland Formation), there is a estimate of 313

million short tons (284 million t) of coal and 89 BCF (billion cubic feet) of gas in place. (Decker and others, 1988)

The portion of the project that I have been directly involved in is the interpretation of the multicomponent vertical seismic profiles (VSPs) and incorporating the VSPs with geologic information and surface seismic data in order to describe the heterogeneities in coalbed methane reservoirs, Cedar Hill Field, New Mexico. The multicomponent VSP was conducted in the Hamilton #3 well, owned and operated by Mesa Petroleum Company. The well is located at 1,184 feet from the south line, 1,112 feet from the west line of Section 30 of Township 32 North, Range 10 West of San Juan County, New Mexico (Figure 1).

In processing the near-offset multicomponent VSPs which includes two near-offset horizontal polarized shear-sources, I was able to observe velocity anisotropy in the subsurface. This gave insight into the dominant open fracture direction in the vicinity of the well. Also, the near-offset VSPs were used in observing reflection characteristics of the coal beds, both in the P- and S- wave data. In processing of the far-offset VSP, I was able to compare the P-wave and converted S-wave responses of the surrounding coal beds .

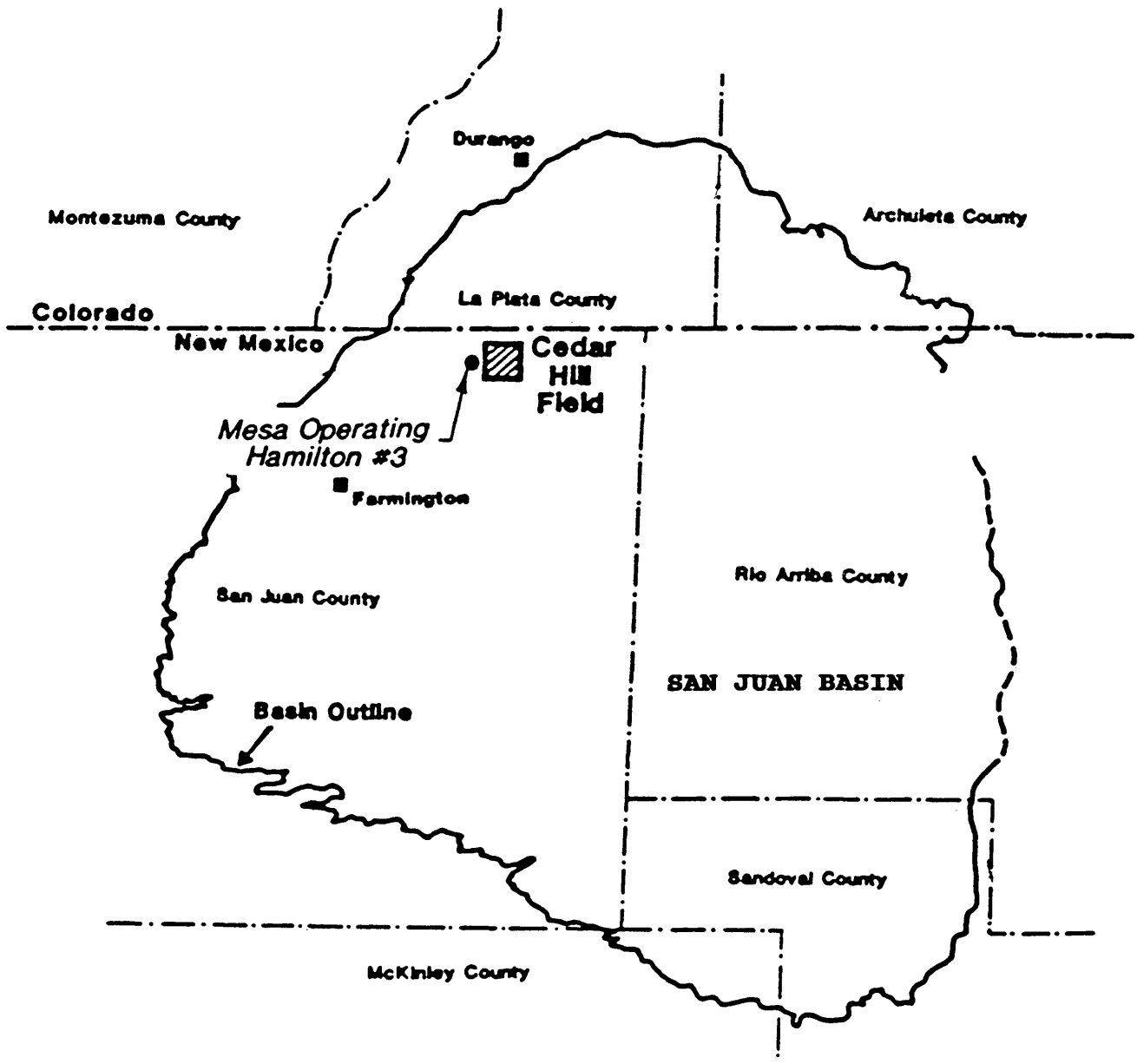


Figure 1: Location map, Cedar Hill Field, New Mexico.
(modified from GRI Report, 1989)

First, I describe the processing steps in the near-offset VSP data and the four component rotation required to find the natural polarization angle in the coal beds. Then, I explain the processing steps for the far-offset VSP. The results of the data are compared to the geologic information and surface seismic data that was available in Cedar Hill Area.

GEOLOGIC SUMMARY

The target zone for coal bed methane is the Cretaceous Fruitland Formation which is made up of coals, mudstones, and sandstones. The formation is located between the overlying Kirtland Shale and underlying Picture Cliffs Sandstone. The occurrence of coal beds within the sandstones suggest the coal formed in a middle coastal-plain to lower alluvial-plain setting (Ambrose and Ayers, 1991). The sandstones that override or underlie the coals are classified as channel-fill bodies.

A total of 45 feet of coal was found in the Hamilton #3 well. A high resolution density log, Figures 2-4, show four separate intervals of coals within the well (GRI/REI report, 1989). In some publications intervals 2, 3, and 4 are known as the upper, middle, and lower Fruitland formations. Interval IV contains the thickest section of coal, 20.9 feet in two major intervals and associated stringers. The basal Fruitland Formation, interval IV, is presently the main productive zone in the Cedar Hills Field.

The major control on productivity of the coals is the fracture system. The fractures in the coal-bearing intervals are classified by the following cleat types: 1) face cleats,

High Resolution Density Log Hamilton #3

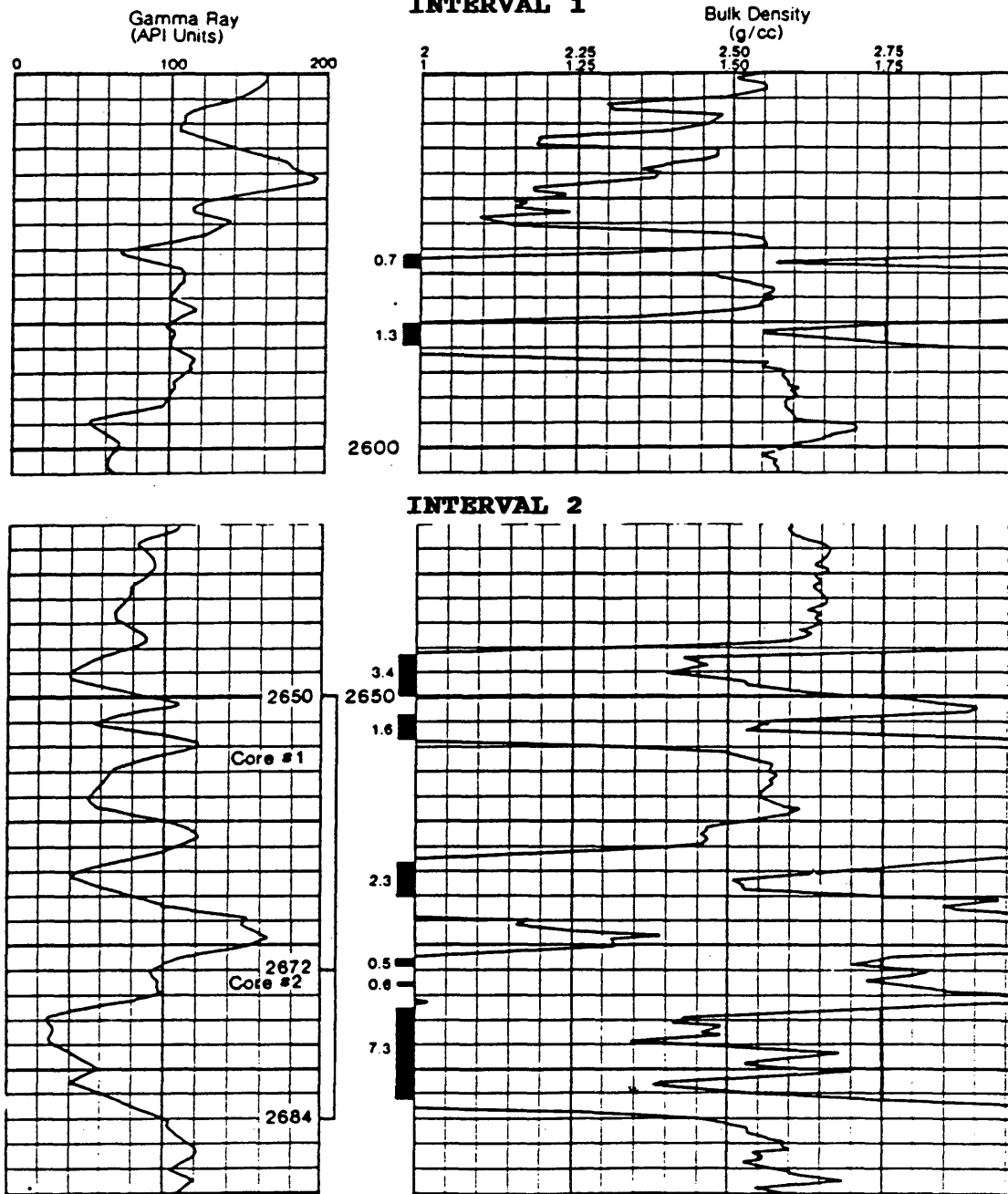


Figure 2: High resolution density log showing coal intervals 1 and 2. (GRI report, 1989)

High Resolution Density Log Hamilton #3 INTERVAL 3

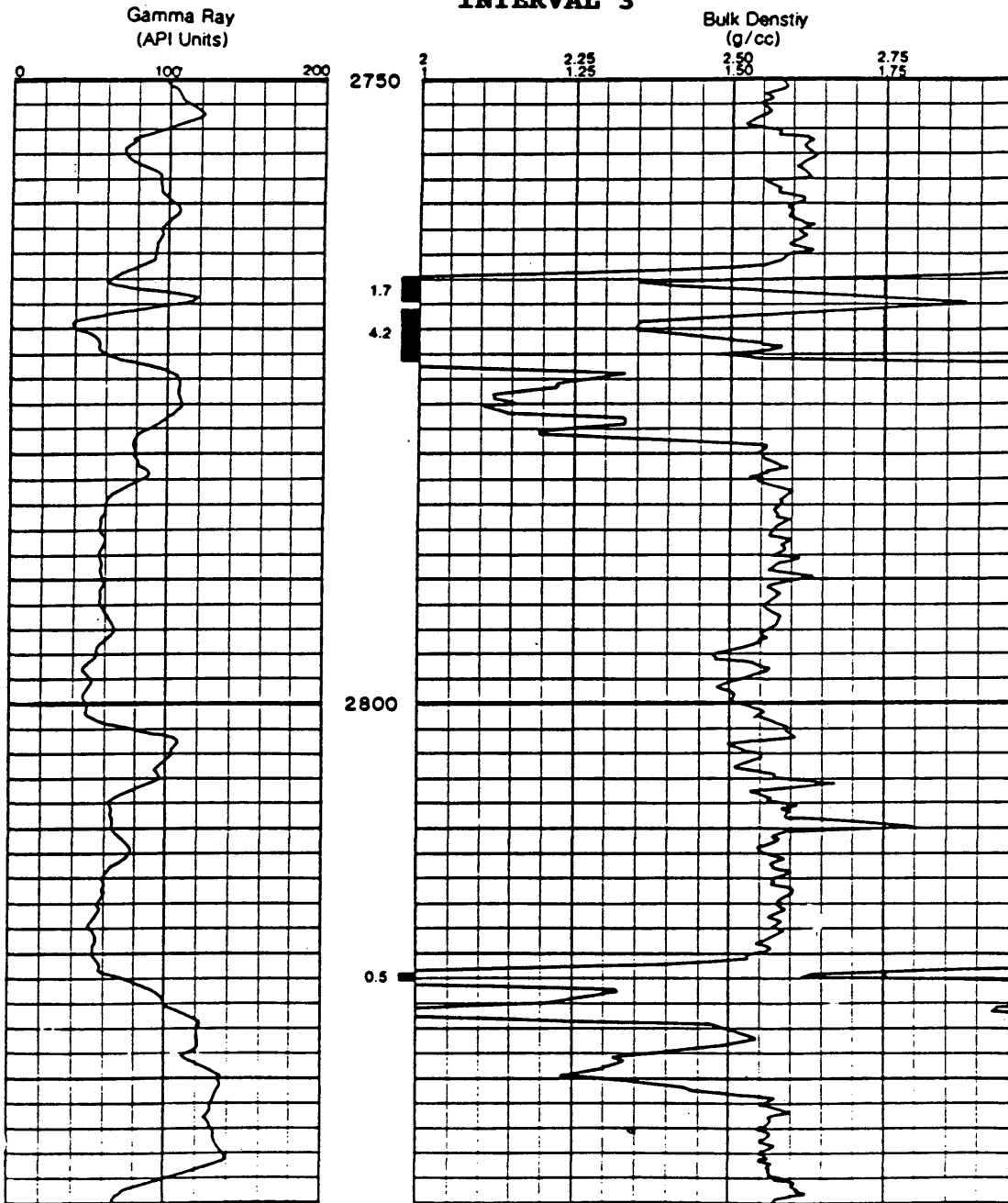


Figure 3: High resolution density log showing coal interval 3.
(GRI Report, 1989)

High Resolution Density Log Hamilton #3 **INTERVAL 4**

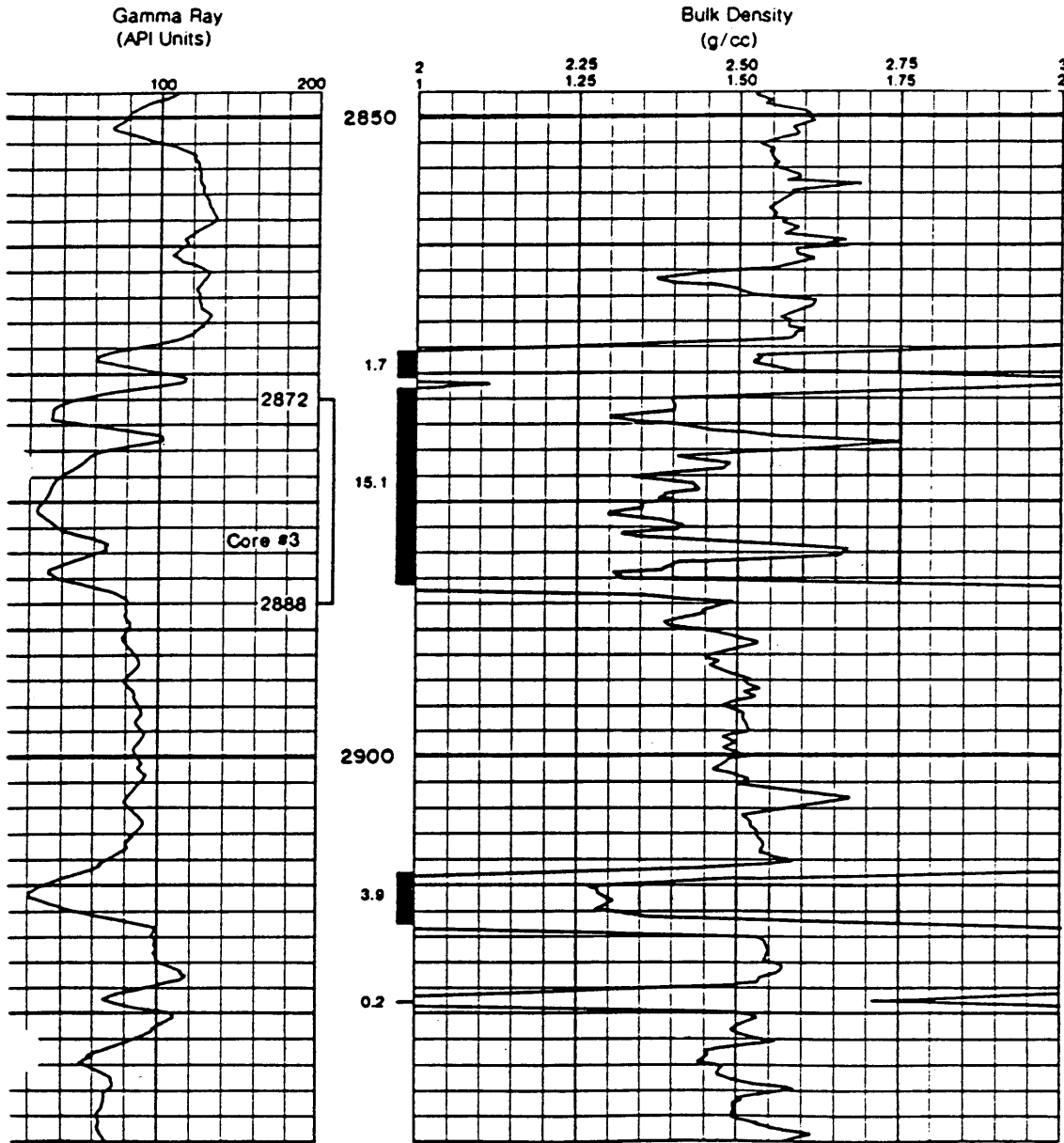


Figure 4: High density resolution log showing coal interval 4, the basal Fruitland Formation. (GRI Report, 1989)

2) butt cleats, or 3) diagonal cleats. Face cleats are characterized as being fully developed and through-going fractures, whereas butt cleats are less developed, smaller, and located orthogonal to the face cleats. Diagonal cleats are located at some angle to the face and butt cleats (TerraTek Core Services report, 1988).

The cleat system is believed to be a result of tectonic stresses applied during the time of coalification, during the Late Cretaceous. Also, the development of these cleats is believed to be influenced by interbedding of coals and non-coal materials (GRI/REI report, 1989).

The production rates within the Cedar Hills field are directly related to the intensity of open fracturing. The strata within the field are almost flat lying (dipping less than 10 feet\mile). However, the layers are faulted and folded, which causes an increase in fracturing within the coal beds (Ambrose and Ayers, 1991).

BACKGROUND PRINCIPLES

A reservoir made up of parallel vertical fractures can be described as being an azimuthally anisotropic medium with a horizontal axis of symmetry. A material exhibits velocity anisotropy if velocity varies with direction (Crampin, 1984). Figure 5 shows a display of the described medium where the axis of symmetry is horizontal.

As shear-waves propagate through such a medium, they are often polarized into natural coordinate frame of reference. This is why shear-wave technology is useful in the exploration of fractured reservoirs. As a shear-wave enters an azimuthally anisotropic medium, splitting occurs into two shear waves, one polarized parallel to fracture orientation (S1) and the other polarized perpendicular to fracture direction (S2), (Crampin, 1985). The only requirement is that the shear-wave must enter at an angle oblique to the fracture orientation. The separation of shear-waves into polarization directions is known as shear-wave birefringence or shear-wave splitting, (Figure 6).

The characteristics of shear-waves in an azimuthally anisotropic medium does depend on the angle of propagation within the medium. For instance, a shear-wave travelling at

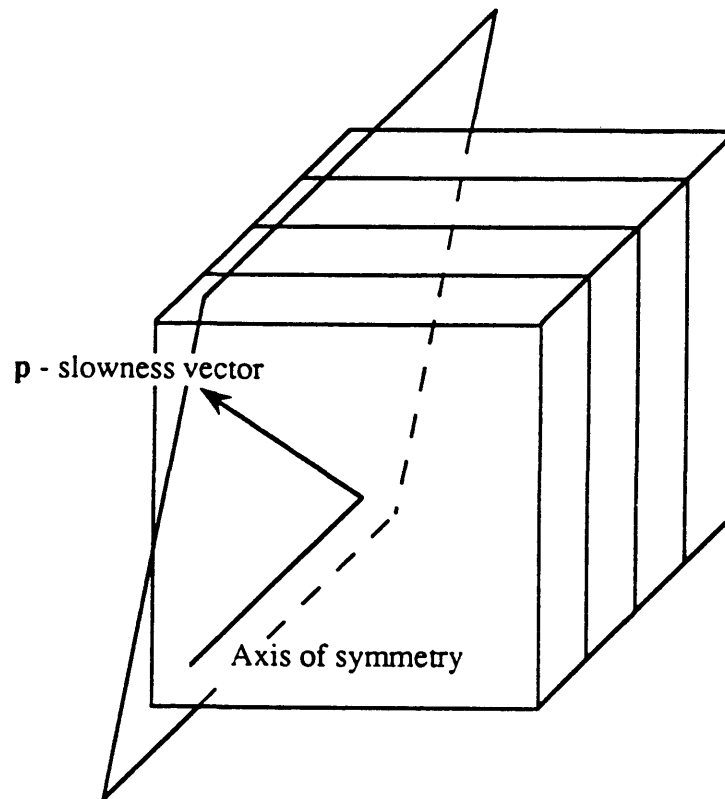


Figure 5: Azimuthally anisotropic medium with a horizontal axis of symmetry. (after Kramer, 1991)

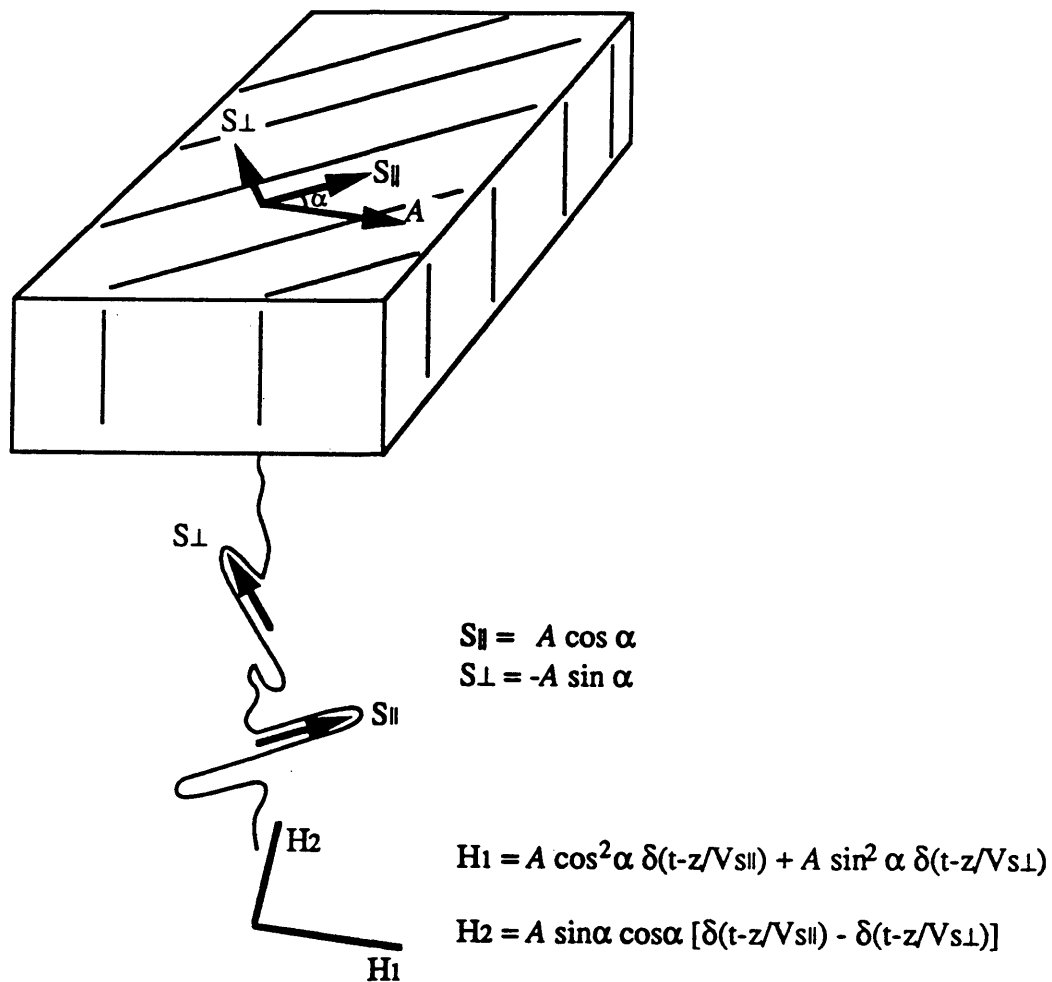


Figure 6: Shear-wave splitting (birefringence) generated by a shear-wave entering an azimuthally anisotropic medium. (after Kramer, 1991)

an angle 45 degrees from the axis of symmetry approaches a point of shear-wave singularity, where S1 and S2 have equivalent velocities (White and Sengbush, 1983). A plot showing the angle of propagation verses velocity is shown in Figure 7.

The S1 wave, parallel to fracture orientation, travels at a faster velocity than the S2 wave, perpendicular to fracture direction. The slow shear-wave velocity is dependent on the fractured medium (intensity of fracturing), whereas the fast shear-waves velocity is influenced by the unfractured medium (mineralogy, fluid constituent in effective void space), (Mueller, 1992). Because of the different travel velocities of the S1 and S2 waves, separate arrival times allow the recording of the polarized shear-waves.

A zero-offset multicomponent VSP and two horizontally polarized shear sources can be used to record shear-wave splitting within the subsurface. By determining the polarization of the shear-wave components, a fracture orientation is found.

Phase velocity for compressional and shear waves travelling through a transversely isotropic medium

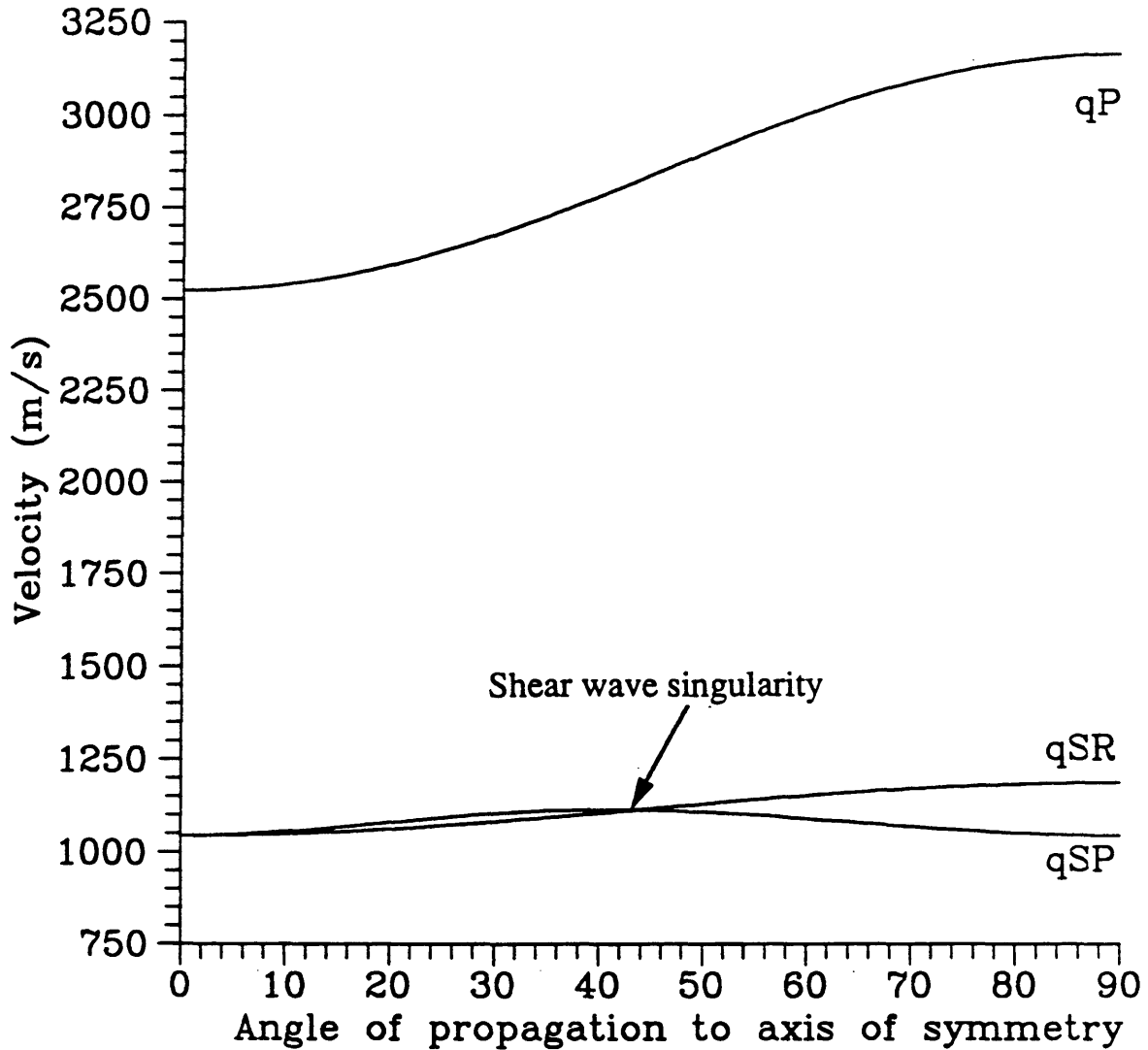


Figure 7: Phase velocities for compressional (qP), fast shear (qSR), and slow shear (qSP) waves propagating through a transversely isotropic medium. (White and Sengbush, 1983)

VSP SURVEY

Acquisition

A multicomponent VSP was recorded in the Hamilton #3 well, owned and operated by Mesa Petroleum Company. The initial vibrator tests were conducted on June 27, 1990, while the data acquisition occurred on June 28 and June 29. The objective of the VSP was to observe shear-wave birefringence and to determine the fracture orientation within the coal beds.

The source locations for the survey consisted of a far-offset and a near-offset. A Litton model 315 compressional source was used in the far offset, located 1529.31 feet from the borehole. The near-offset, 140 feet from the borehole, was made up of three sources; Litton model 315 compressional source, Mertz shear-wave source polarized radial to the borehole, and Mertz shear-wave source polarized transverse to the borehole. A diagram showing the relative position of the sources with respect to the borehole is shown in Figure 8. The sweep parameters for all four vibrators are as follows:

Compressional energy sources: 10-132.5 Hz, 14sec sweep length
Shear energy sources: 10-83.5 Hz , 14sec sweep length

The recording for the VSP was done with Schlumberger's

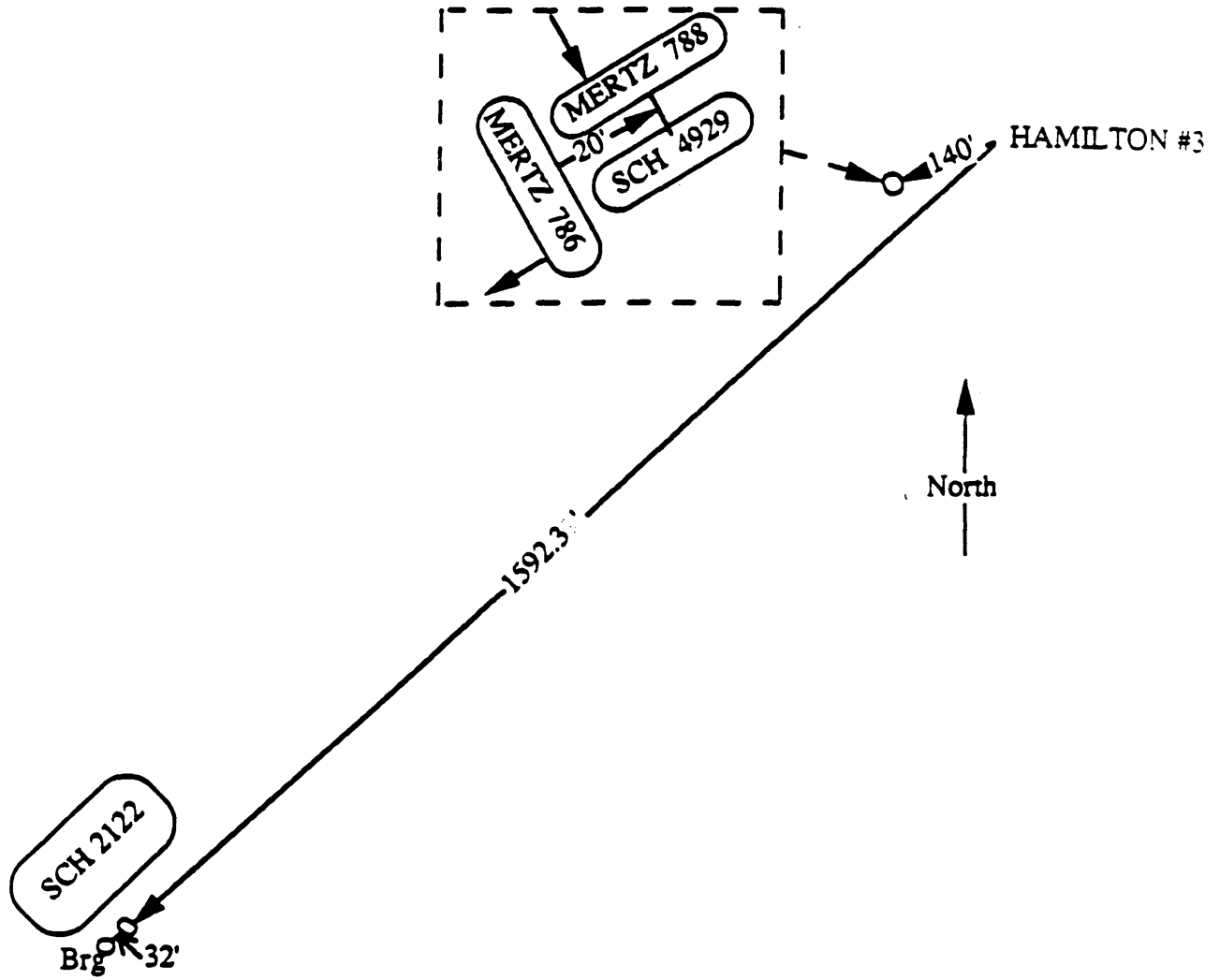


Figure 8: Source locations with respect to the Hamilton #3 well. (after Kramer, 1991)

new five shuttle multicomponent tool which measures two horizontal components (X and Y) and a vertical component (Z). The interval between receivers was 10 feet from depths 2970 feet to 2530 feet, 25 feet from depths 2525 feet to 1925 feet, and 50 feet from depths 1900 feet to 300 feet. Also, several receiver depths were repeated as the sonde was brought up the hole. Table I summarizes the number of vibrator sweeps per receiver depth for each source position.

Table I: Number of vibrator sweeps per receiver depth for each source location in the Cedar Hills VSP. NP is near-offset P-wave; NR is near-offset radial shear; NT is near-offset transverse shear; and FP is far-offset P-wave. * indicates repeated recording levels.

TRACE	DEPTH	NP	NR	NT	FP	TRACE	DEPTH	NP	NR	NT	FP
1	2970	7	7	7	7	45	2530	7	7	7	7
2	2960	7	7	7	7	46	2525	5	5	5	5
3	2950	7	7	7	7	47	2500	5	5	5	5
4	2940	7	7	7	7	48	2475	5	5	5	5
5	2930	7	7	7	7	49	2450	5	5	5	5
6	2920	7	7	7	7	50	2425	5	5	5	5
7	2910	7	7	7	7	51	2400	5	5	5	5
8	2900	7	7	7	7	52	2375	5	5	5	5
9	2890	7	7	7	7	53*	2350	5	5	5	5
10	2880	7	7	7	7	54*	2325	5	5	5	5
11	2870	7	7	7	7	55	2300	5	5	5	5
12	2860	7	7	7	7	56	2275	5	5	5	5
13	2850	7	7	7	7	57	2250	5	5	5	5
14	2840	7	7	7	7	58	2225	5	5	5	5
15	2830	7	7	7	7	59	2200	5	5	5	5
16	2820	7	7	7	7	60	2175	5	5	5	5
17	2810	7	7	7	7	61*	2150	5	5	5	5
18	2800	7	7	7	7	62*	2125	5	5	5	5
19	2790	7	7	7	7	63	2100	5	5	5	5
20	2780	7	7	7	7	64	2075	5	5	5	5
21*	2770	7	7	7	7	65	2050	5	5	5	5
22*	2760	7	7	7	7	66	2025	5	5	5	5
23*	2750	7	7	7	7	67	2000	5	5	5	5

(continued)

Table I (continued): Number of vibrator sweeps per receiver depth for each source location in the Cedar Hills VSP. NP is near-offset P-wave; NR is near-offset radial shear; NT is near-offset transverse shear; and FP is far-offset P-wave. * indicates repeated recording levels.

TRACE	DEPTH	NP	NR	NT	FP	TRACE	DEPTH	NP	NR	NT	FP
24*	2740	7	7	7	7	68	1975	5	5	5	5
25*	2730	7	7	7	7	69*	1950	5	5	5	5
26	2720	7	7	7	7	70	1925	5	5	5	5
27	2710	7	7	7	7	71	1900	5	5	5	5
28	2700	7	7	7	7	72	1850	5	5	5	5
29	2690	7	7	7	7	73	1800	5	5	5	5
30	2680	7	7	7	7	74*	1750	5	5	5	5
31	2670	7	7	7	7	75	1700	5	5	5	5
32	2660	7	7	7	7	76	1650	5	5	5	5
33	2650	7	7	7	7	77	1600	5	5	5	5
34	2640	7	7	7	7	78	1550	5	5	5	5
35	2630	7	7	7	7	79	1000	5	5	5	-
36	2620	7	7	7	7	80	950	3	3	3	-
37	2610	7	7	7	7	81	900	3	3	3	-
38	2600	7	7	7	7	82	850	3	3	3	-
39	2590	7	7	7	7	83	800	3	3	3	-
40	2580	7	7	7	7	84	500	3	3	3	-
41	2570	7	7	7	7	85	450	3	3	3	-
42	2560	7	7	7	7	86	400	3	3	3	-
43*	2550	7	7	7	7	87	350	3	3	3	-
44	2540	7	7	7	7	88	300	3	3	3	-

Preprocessing

Before the field data could be downloaded to an IBM PC for processing on Halliburton Geophysical Services' multicomponent VSP package, the data had to be demultiplexed into separate source and receiver files. This resulted in a total of twelve separate VSPs (four sources recorded into a three component receiver). The data were then correlated with the appropriate sweep (P or S). The bad traces were deleted and the data went into a final median stack.

NEAR-OFFSET COMPRESSIONAL-WAVE VSP

The vertical component (Z) from the near-offset P-wave data set (Figure 9), was processed to obtain a zero-offset seismic trace. The Z component records a substantial portion of the compressional data in a near-offset multicomponent VSP.

The first step in processing the near-offset VSP is to compensate for spherical divergence and attenuation of the down-going wavefield. The following spherical divergence correction was applied to each trace:

$$SCALER = \frac{TX * V_{rms}^2}{V_{surf}^2}$$

where TX is time before normal move out, Vrms is root-mean square velocity calculated from first arrival times and depths, and Vsurf is the surface velocity. In order to avoid overscaling, the scalars were normalized to the values at Tmax/4.

Wavefield separation of the down-going and up-going energy was accomplished through median filtering. The separated down-going energy, Figure 10, was obtained with a 12 point median filter. The up-going energy is found simply by

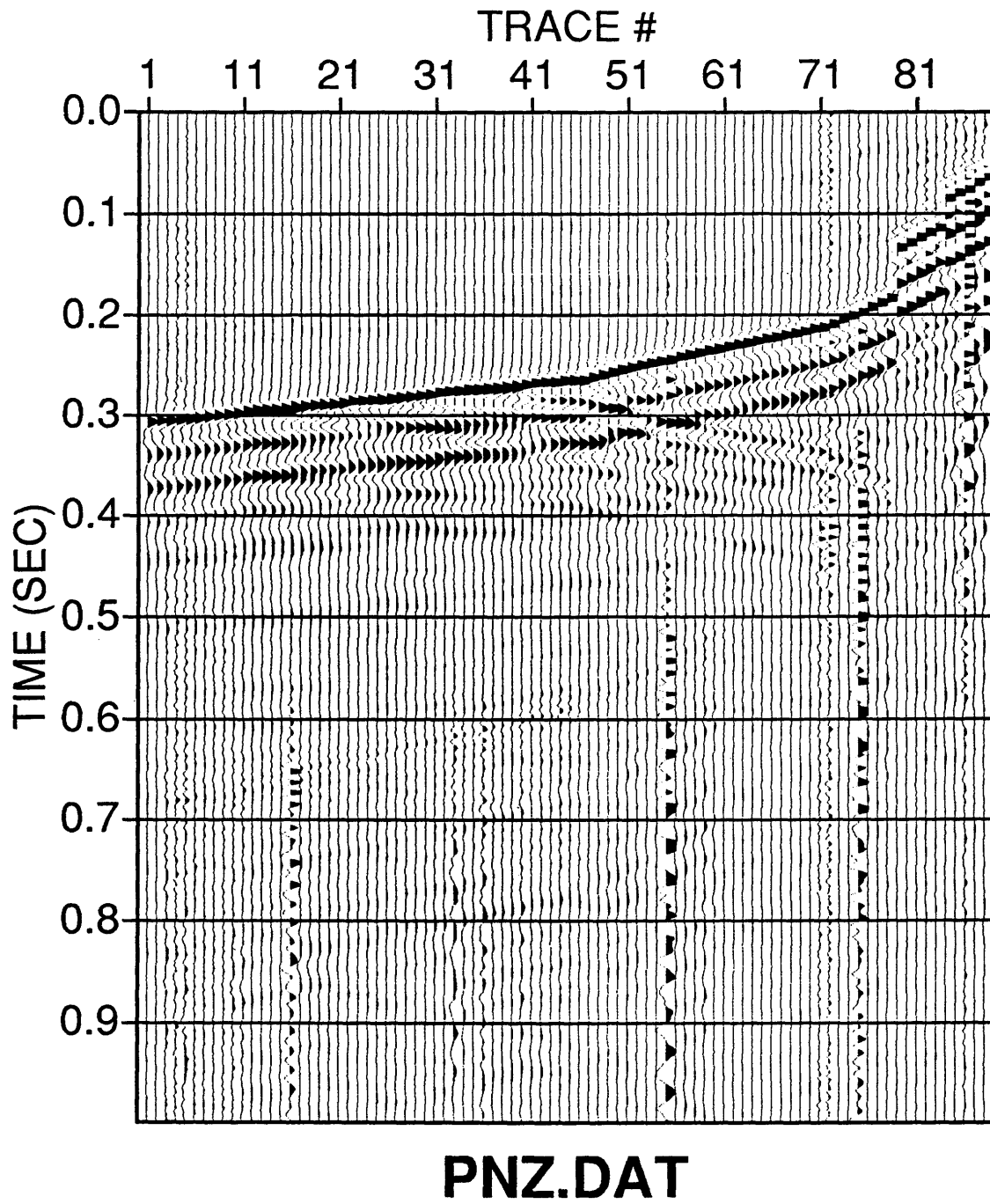


Figure 9: Vertical (Z) component from the near-offset P-wave data.

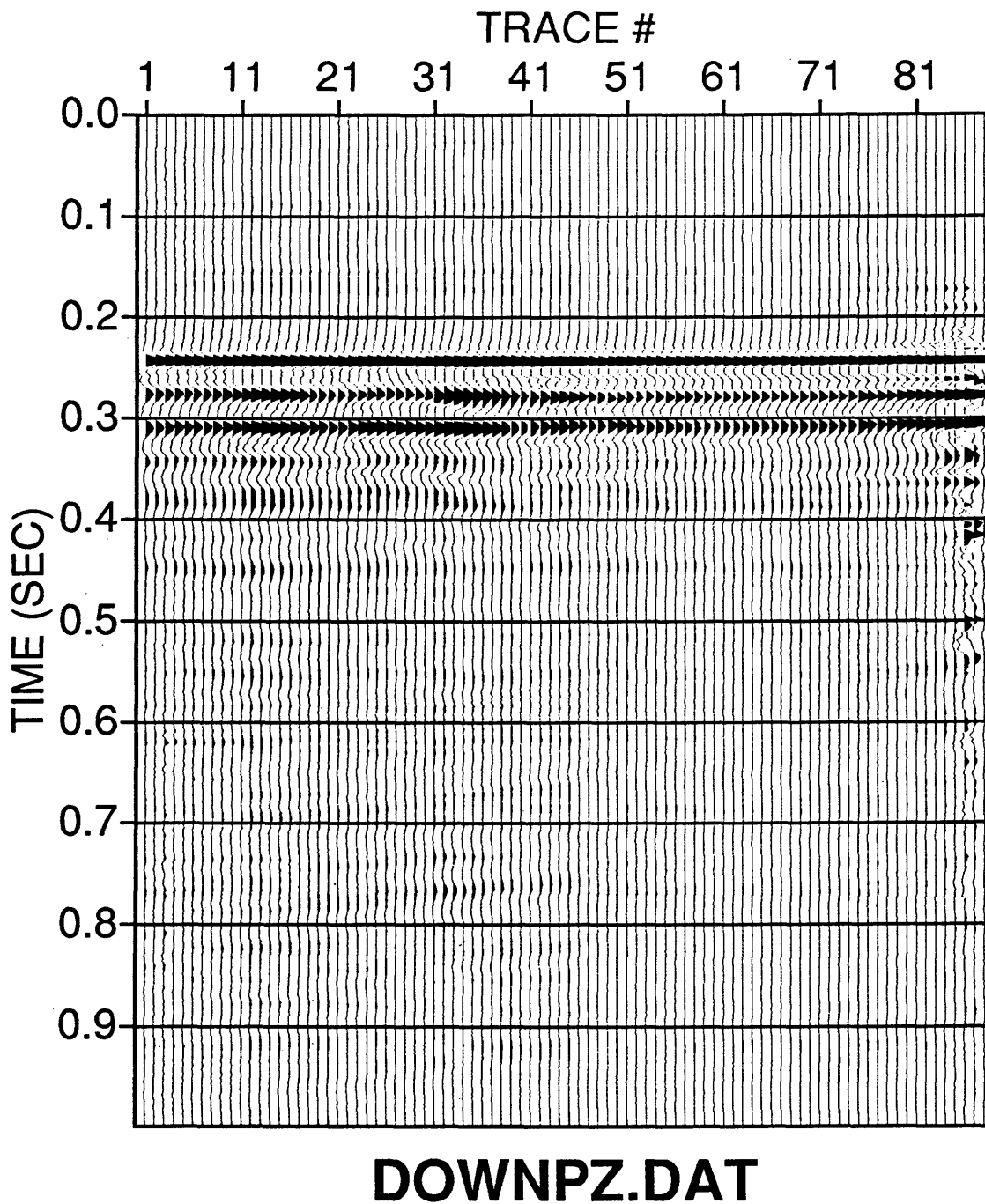


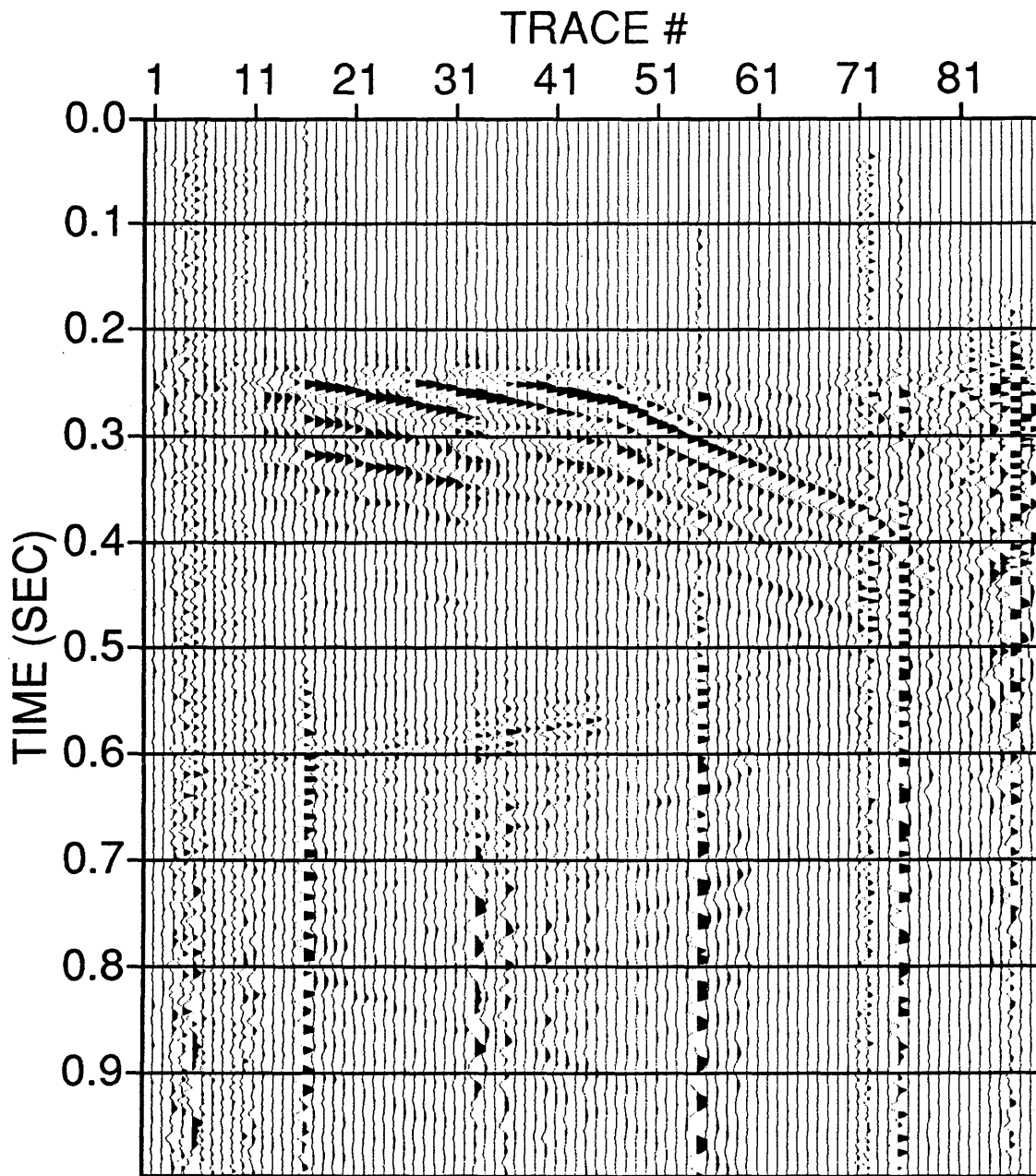
Figure 10: Down-going compressional data acquired through median filtering.

subtracting the down-going energy from the pre-median filtered data. The reflected compressional energy is displayed in Figure 11.

The next step is to eliminate the surface and interbedded multiples present in the up-going data. This was accomplished by designing an inverse filter applied to the down-going compressional data and applying it to the up-going P-wave data. Figure 12 is a plot of the inverse filter on the down-going data, where the down-going energy has been collapsed into a 10-100 Hz zero phase pulse. Before the inverse filter was applied to the upgoing energy, a nine point median filter reduced some of the noise on the data. The up-going energy after application of the inverse filter is shown in Figure 13. The deconvolved up-going data shows a better resolution in the reflecting events.

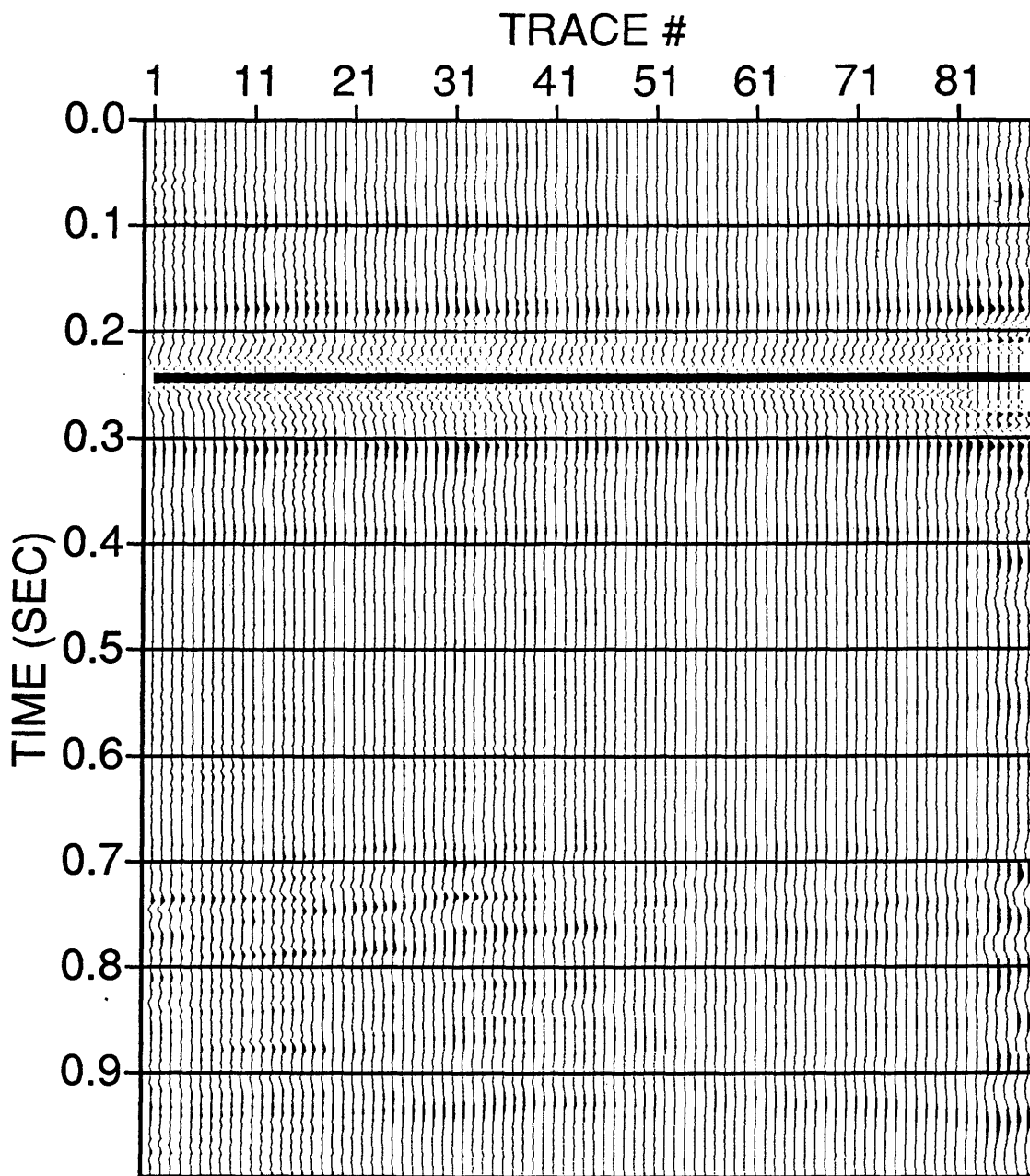
A spherical divergence correction was once again applied to the data, however this time the time variant part, appropriate for up-going wavefield. Then, the data were flattened on the up-going events, followed by another 12 point median filter to enhance the reflected events.

Finally, the up-going P-wave data were corridor stacked and fed with a 10(24) - 90(36) HZ(dB/Oct) bandpass filter. The results are shown in Figure 14. The two major peaks indicated on the plot correspond coal beds, intervals II and



UPGOPZ.DAT

Figure 11: Up-going compressional energy after subtraction of the down-going energy from the pre-median filtered data.



DOWNPZ.DCN

Figure 12: Results of the down-going energy after applying the 10(24) - 100(36) Hz (dB/Oct) wavelet shaping filter to collapse the multiples.

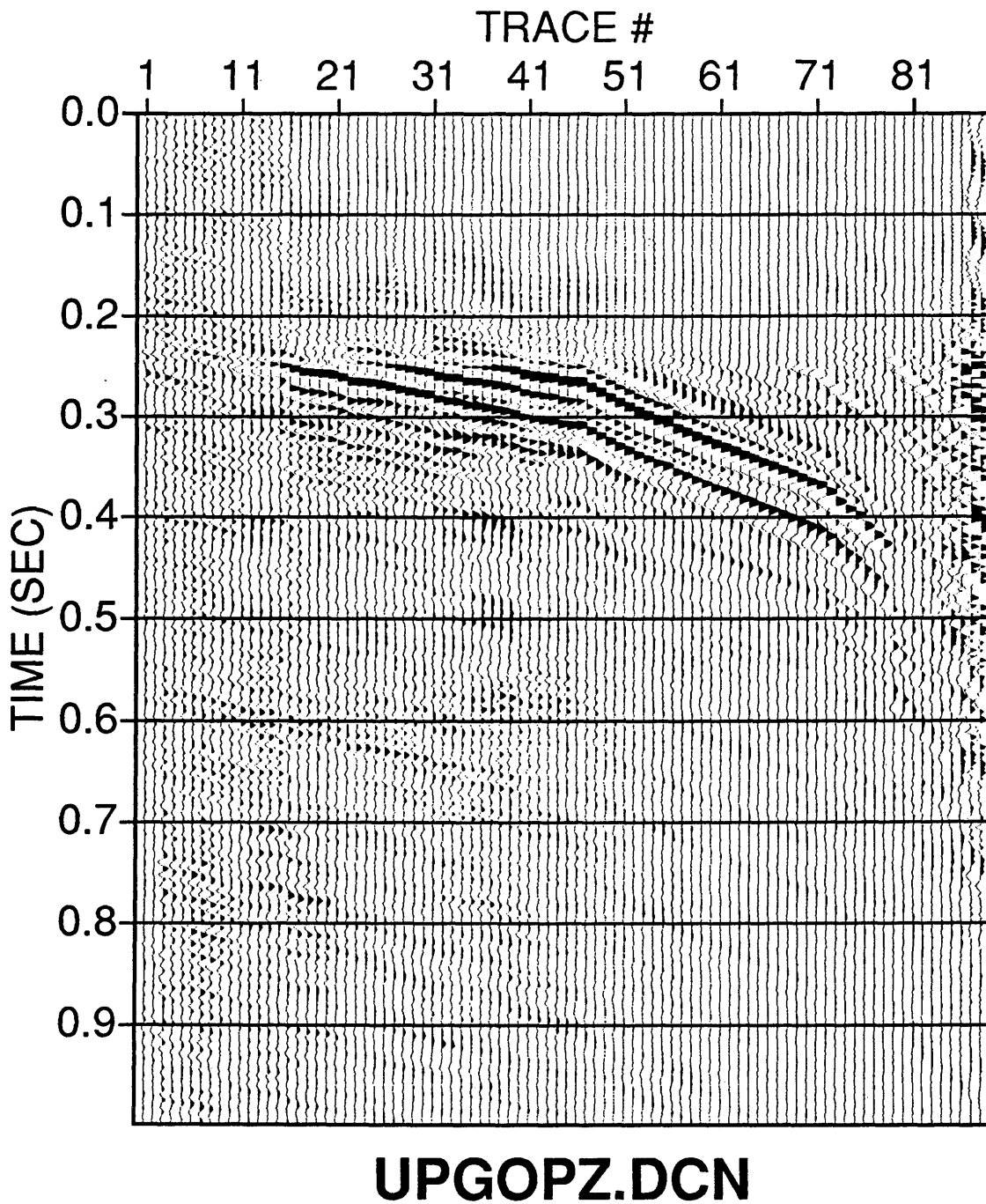


Figure 13: Results of the up-going energy after applying the 10(24) - 100(36) Hz (dB/Oct) wavelet shaping filter designed on the down-going energy.

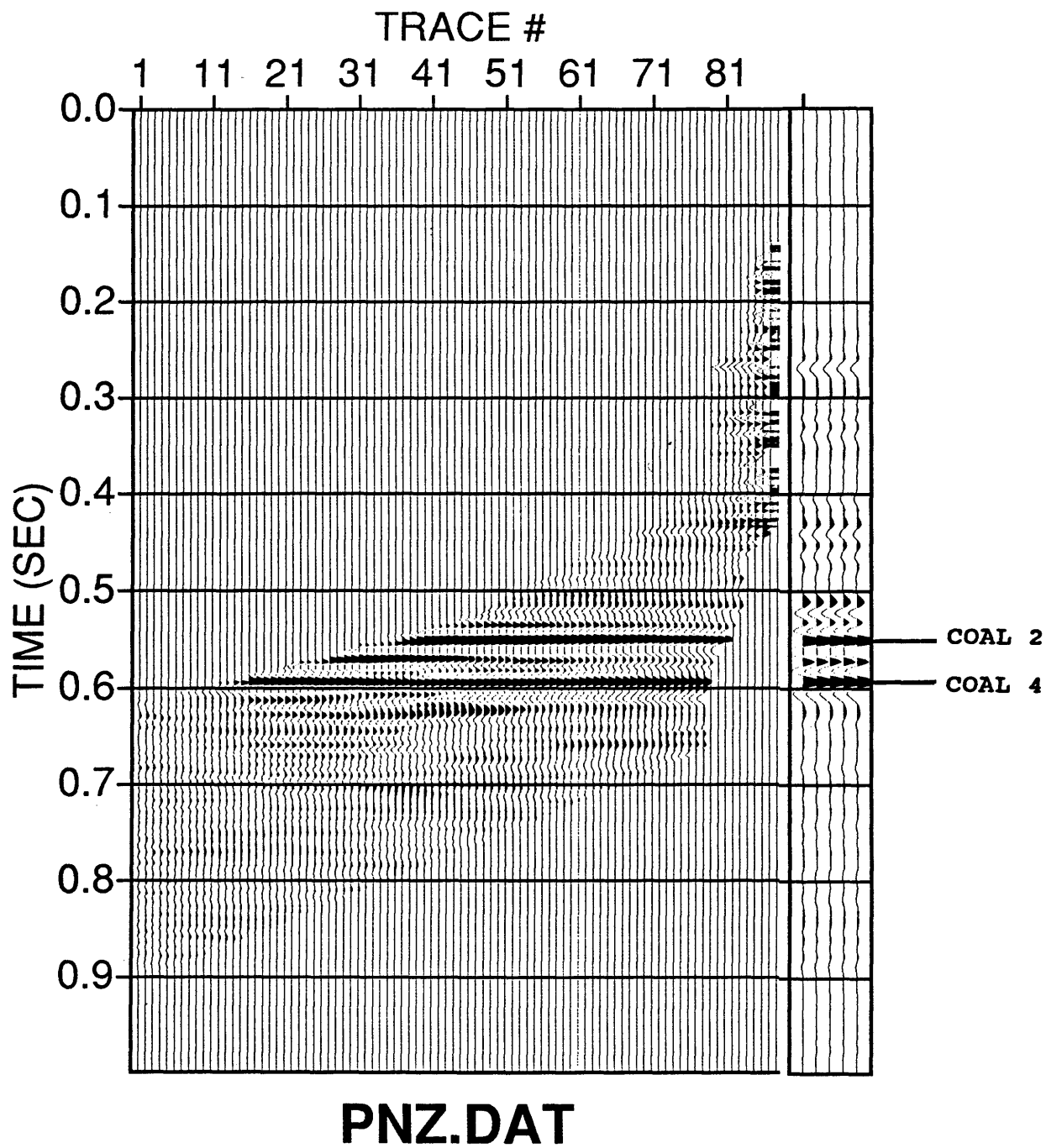


Figure 14: Unstacked and corridor stacked compressional data with a 10(24) - 90(36) Hz(dB/oct) bandpass filter.

IV, found within the Cretaceous Fruitland formation. Intervals I and III , coal thicknesses of less than 16 feet, were not resolved on the VSP data. Note that the coal intervals are made up of numerous coal stringers not just one coal bed. (Figures 2-4)

Figure 15 shows an east-west line from the 3-D multicomponent survey in the vicinity of the Hamilton #3 well. The near-offset VSP has been spliced into the appropriate location. There is a good correlation in the reflecting coal events between the two data sets. Also, Figure 16 is a north-south line through the Hamilton #3 well, again showing a good correlation in reflecting coal events.

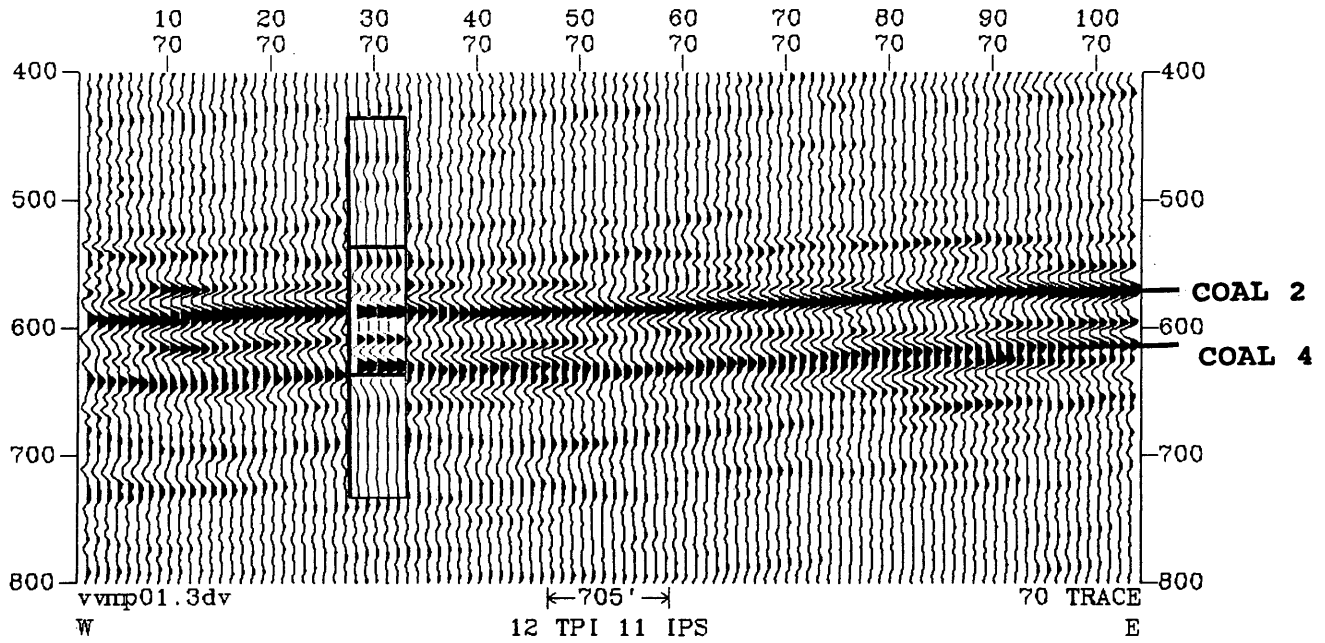


Figure 15: East-West line from the surface 3-D multicomponent seismic survey showing a tie with the near-offset compressional VSP corridor stack.

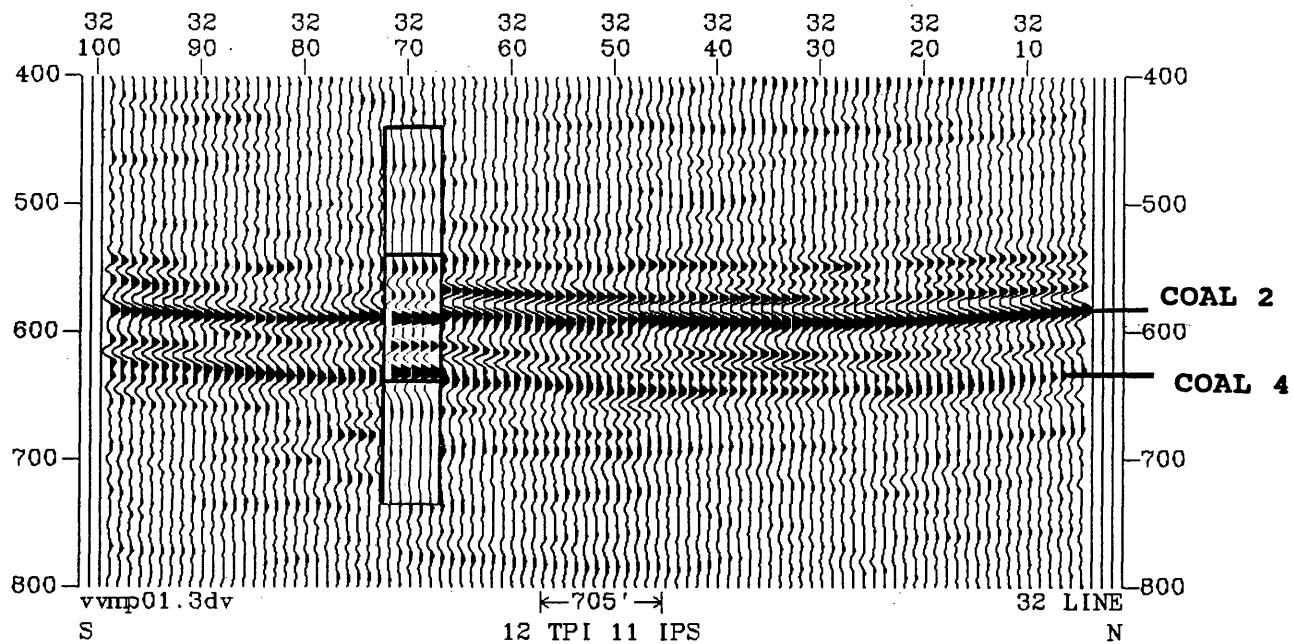


Figure 16: North-South line from the surface 3-D multicomponent seismic survey showing a tie with the near-offset compressional VSP corridor stack.

TOOL ORIENTATION

The X, Y, and Z components of the far-offset P-wave data set are displayed in Figures 17-19. A change in polarity is observed on the two horizontal components (X and Y). This is caused by the rotation of the sonde as it is brought up the hole. The rotation is removed by maximizing the energy in-line to the source-receiver plane (OHPF) and minimizing the energy cross-line to the source-receiver plane (THPF).

The first step in removing rotation is to determine the azimuthal angles of the sonde at each receiver level. Hodogram analysis of the first arrival P-wave energy on the X and Y components (far-offset P-wave energy for traces 1-78 and near-offset P-wave energy for traces 79-88) was used in finding the orientation angles. A plot of the azimuthal tool orientation angles at each receiver depth is shown in Figure 20.

By knowing the tool orientation, the components were rotated in-line and cross-line with respect to the source-receiver plane. The equations used in rotating the data are as follows:

$$OHPF = X(t, d) \cos [\theta(d)] + Y(t, d) \sin [\theta(d)]$$

$$THPF = -X(t, d) \sin[\theta(d)] + Y(t, d) \cos[\theta(d)]$$

where $X(t, d)$ and $Y(t, d)$ are the horizontal compressional components and $\theta(d)$ is tool orientation from North at each receiver depth(d). The results are shown in Figures 21 and 22. Tool orientation has apparently been removed and the events are more coherent throughout the data. The energy that is present on the transverse component (Figure 22), is mainly SH energy that has been produced by the P-wave source and possible P-SV converted energy which has split.

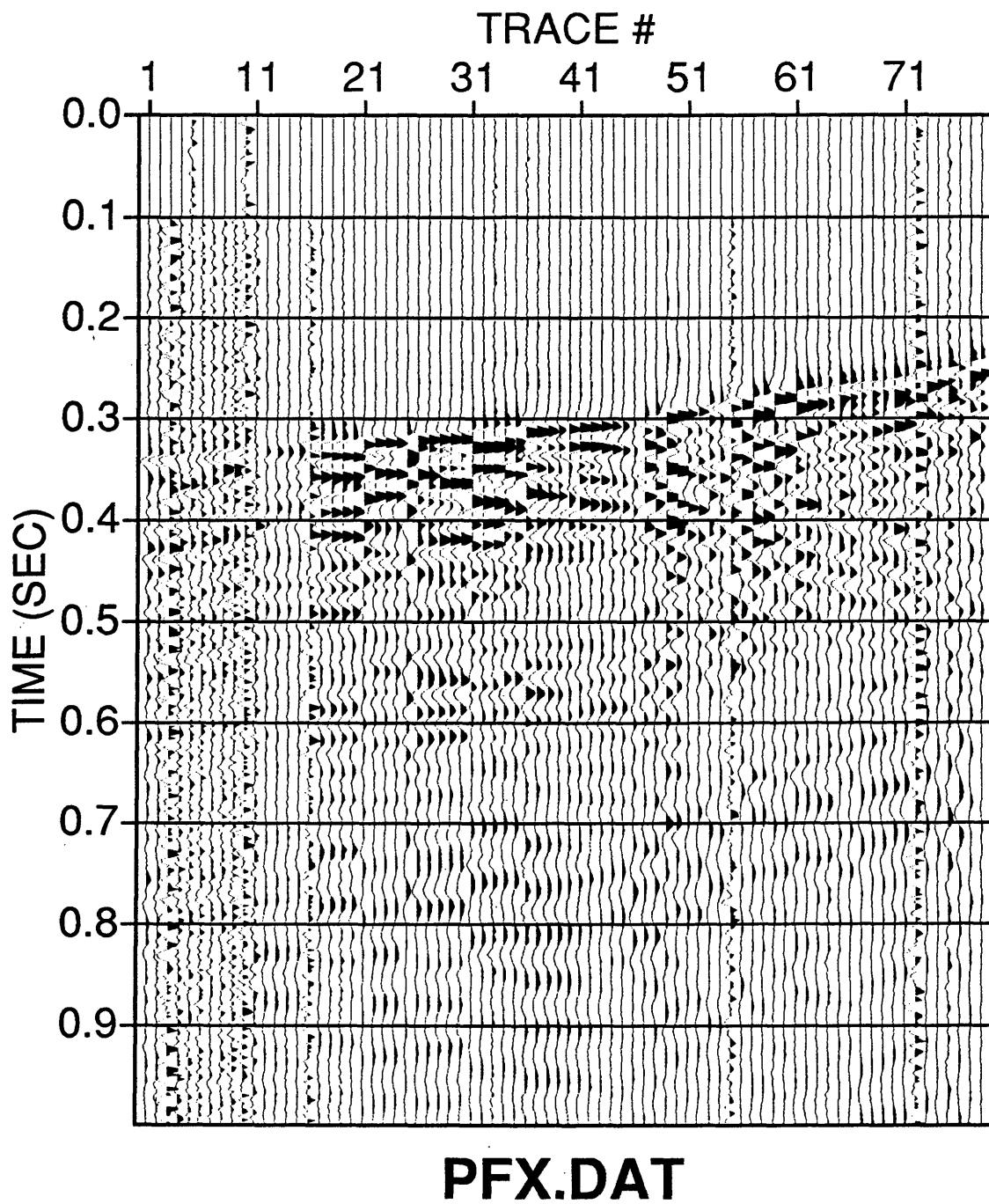
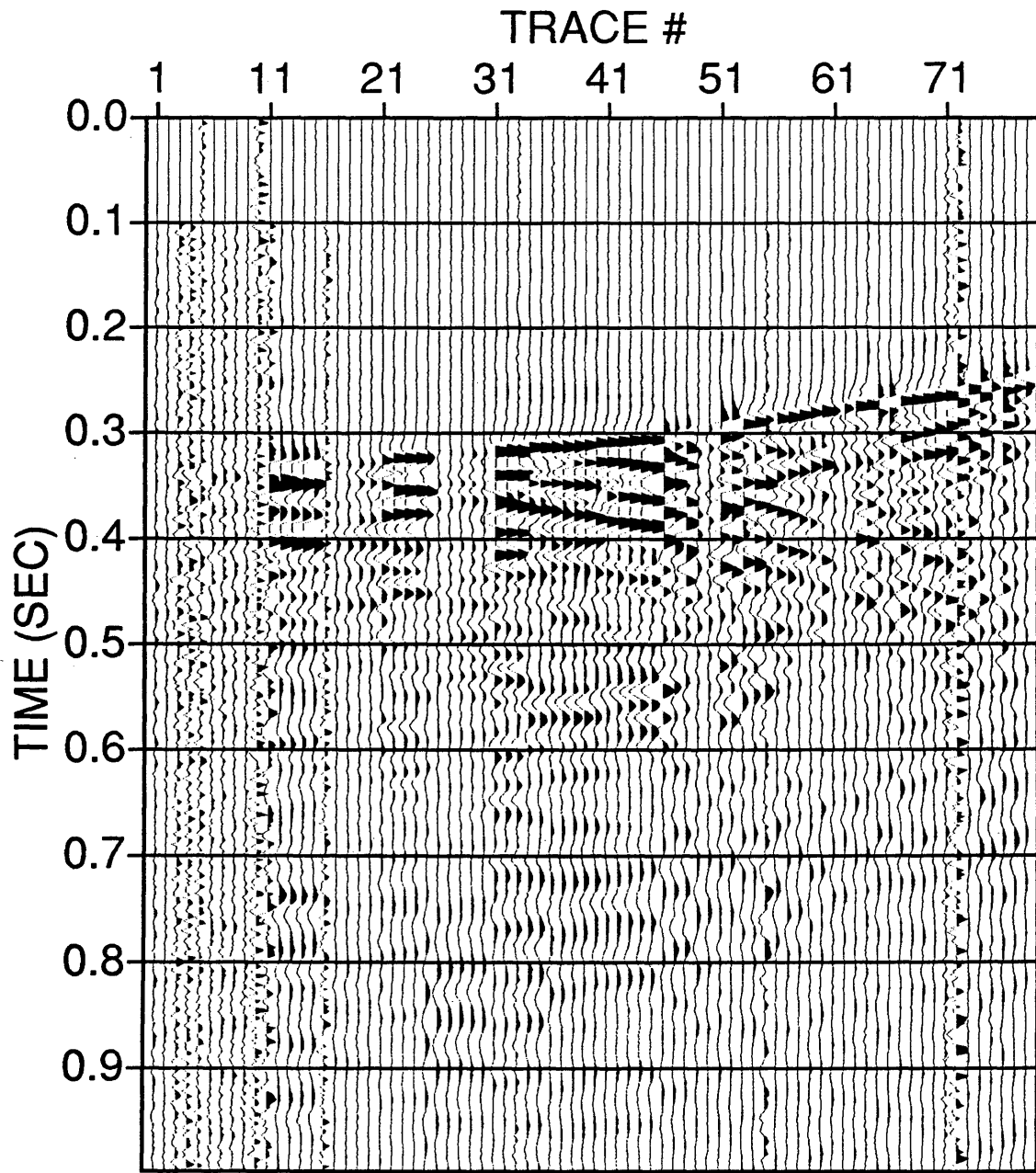
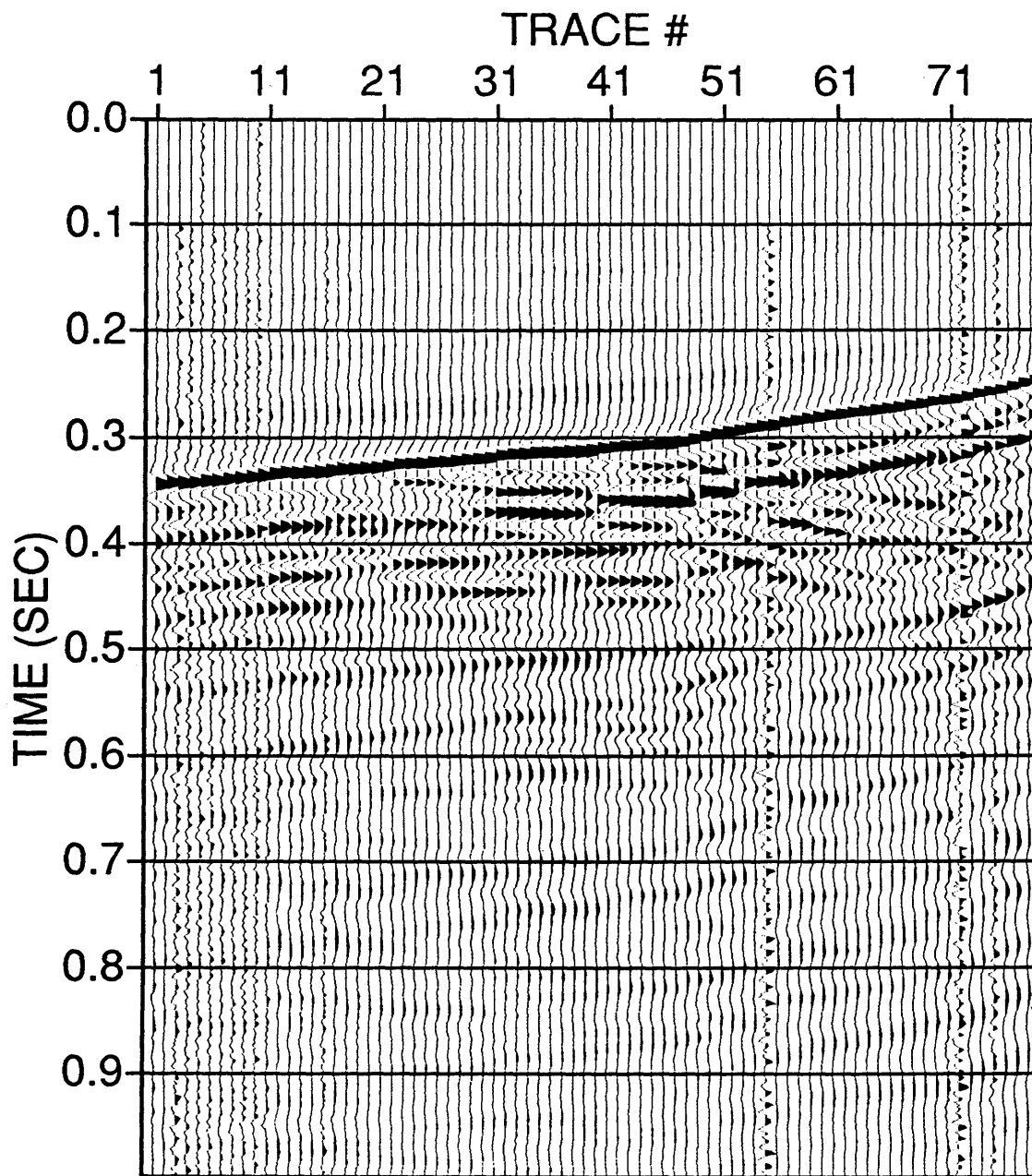


Figure 17: Horizontal (X) component from the far-offset P-wave data.



PFY.DAT

Figure 18: Horizontal (Y) component from the far-offset P-wave data.



PFZ.DAT

Figure 19: Vertical (Z) component from the far-offset P-wave data.

Azimuthal Tool Rotation Angles Far-Offset VSP

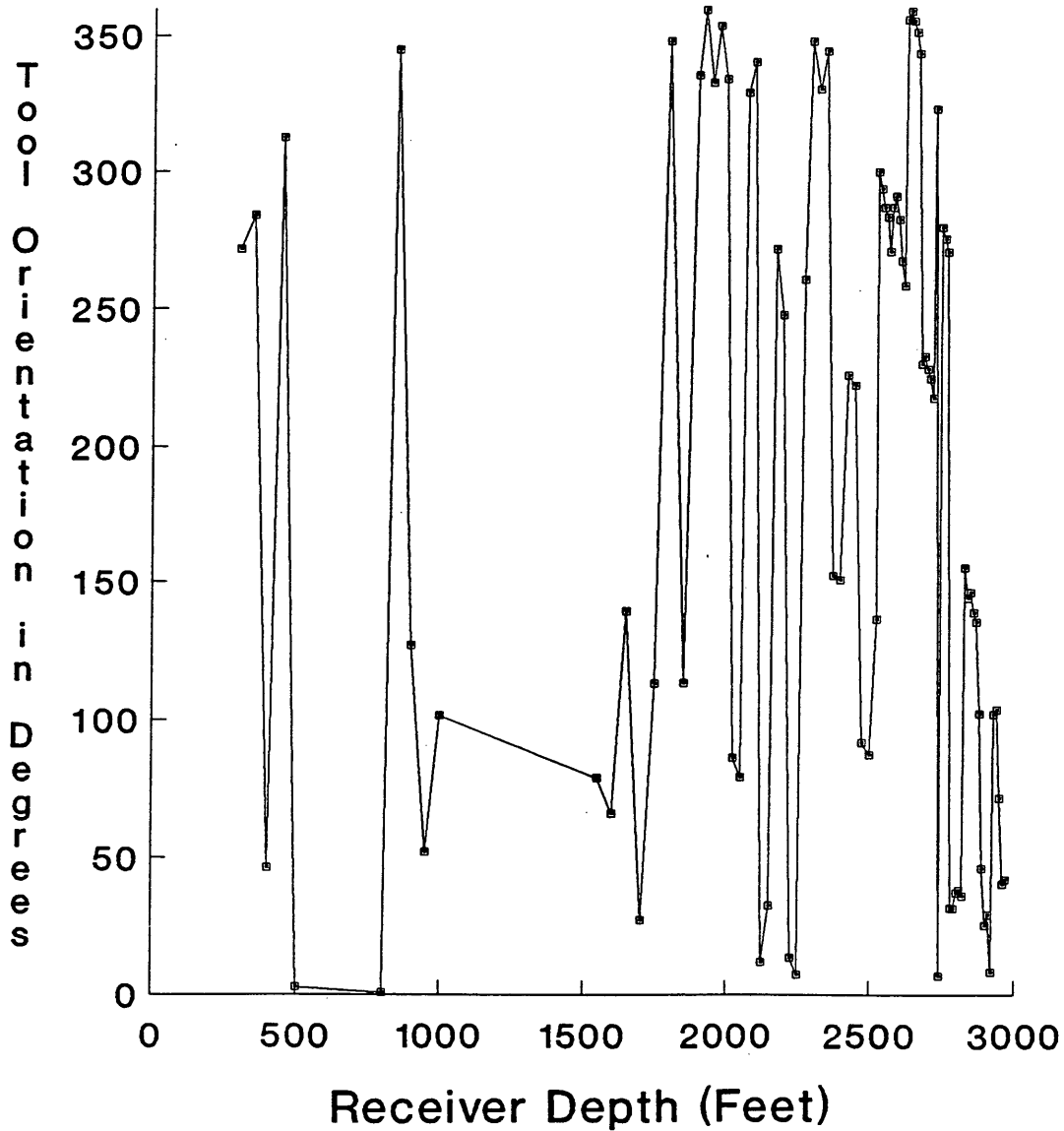


Figure 20: Azimuthal tool orientation angles (from true North) found through hodogram analysis of the far-offset P-wave X and Y data sets.

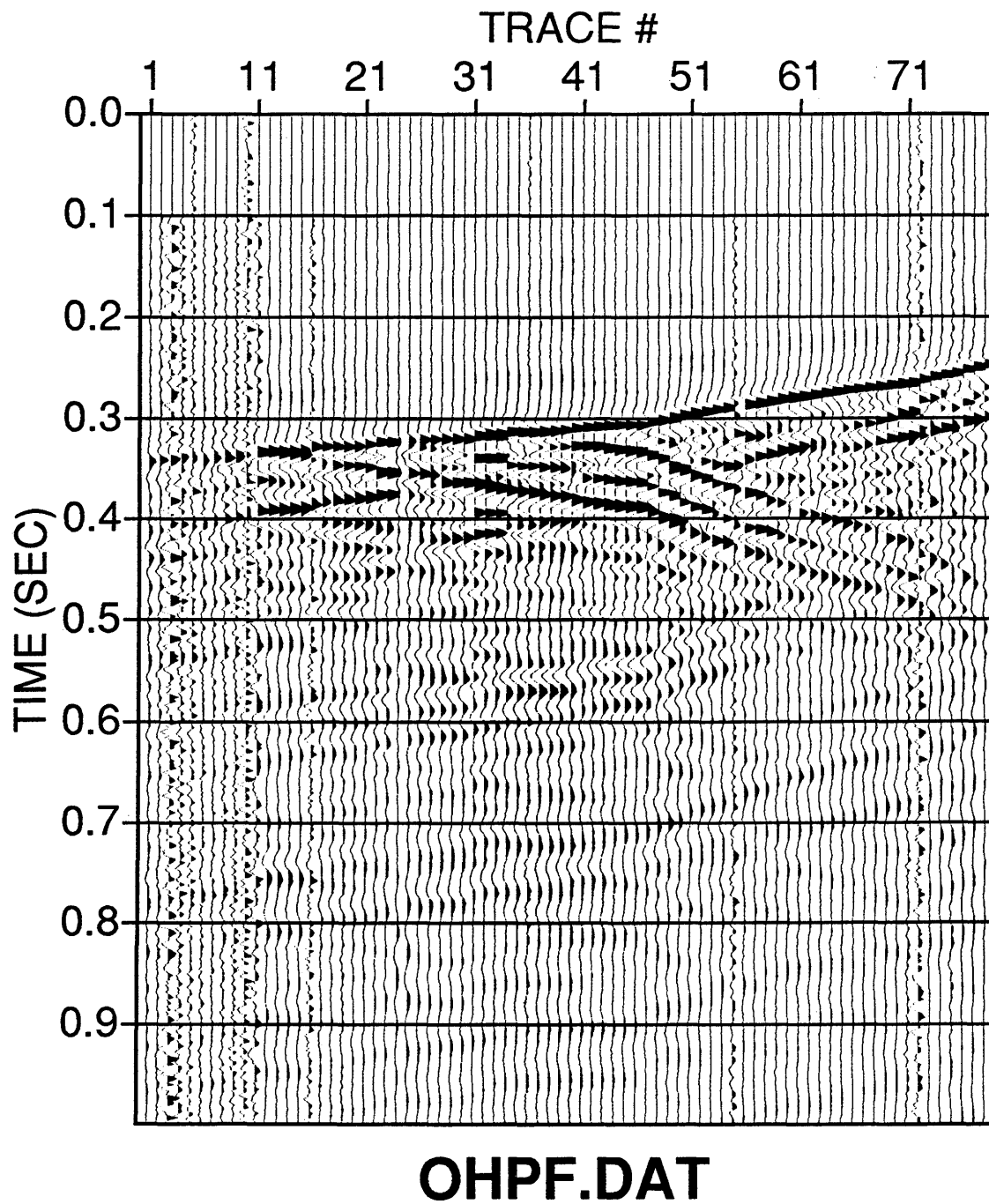


Figure 21: Horizontal far-offset P-wave component oriented inline to the source receiver plane.

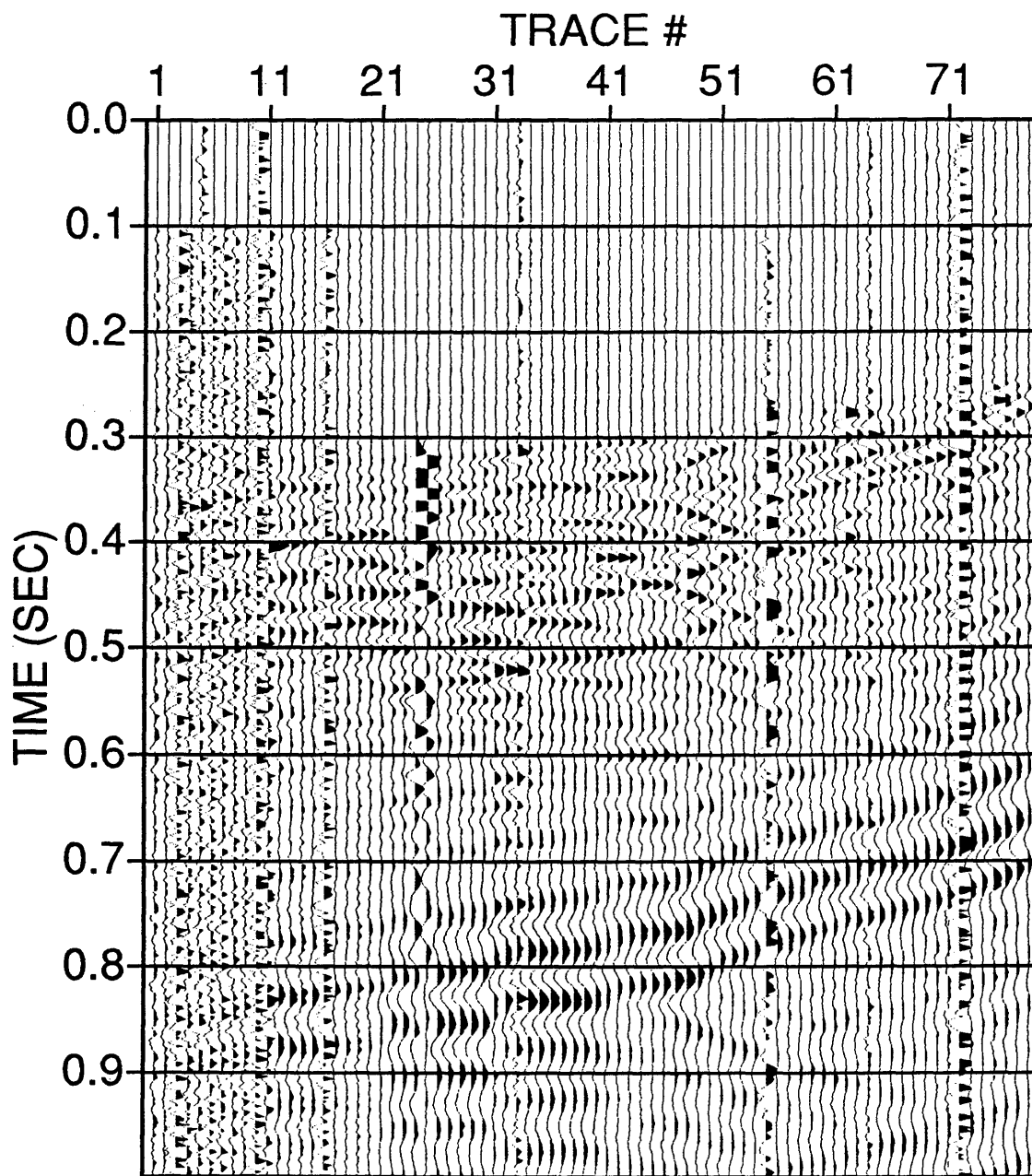


Figure 22: Horizontal far-offset P-wave component oriented transverse to the source receiver plane. (contains SH energy generated from the P-wave source)

NEAR-OFFSET SHEAR-WAVE VSPPs

The raw data from the radial shear-wave source is displayed in Figures 23-25 (X, Y, and Z components, respectively). As in the far-offset compressional data, tool rotation must be removed on the two horizontal shear components. The azimuthal tool orientation angles calculated from the first arrivals of the far-offset P-wave data (Figure 20), were used in rotating the data into in-line and cross-line components. The two radial shear components are displayed in Figures 26 and 27, respectively. No apparent energy should be recorded on the cross-line component (Figure 27), if the subsurface medium is isotropic. However, shear-wave energy is recorded on the transverse component, indicating shear-wave birefringence due to a transversely anisotropic medium. Also, the vertical component (Z) shows recorded compressional data, output from the shear-wave source. This is shown by the similar arrival times between the vertical component of the near-offset P-wave data (Figure 9), and the vertical component of the near-offset radial shear-wave data, (Figure 25).

The two horizontal components of the transverse shear-wave data (Figures 28-30), were also rotated into in-line and

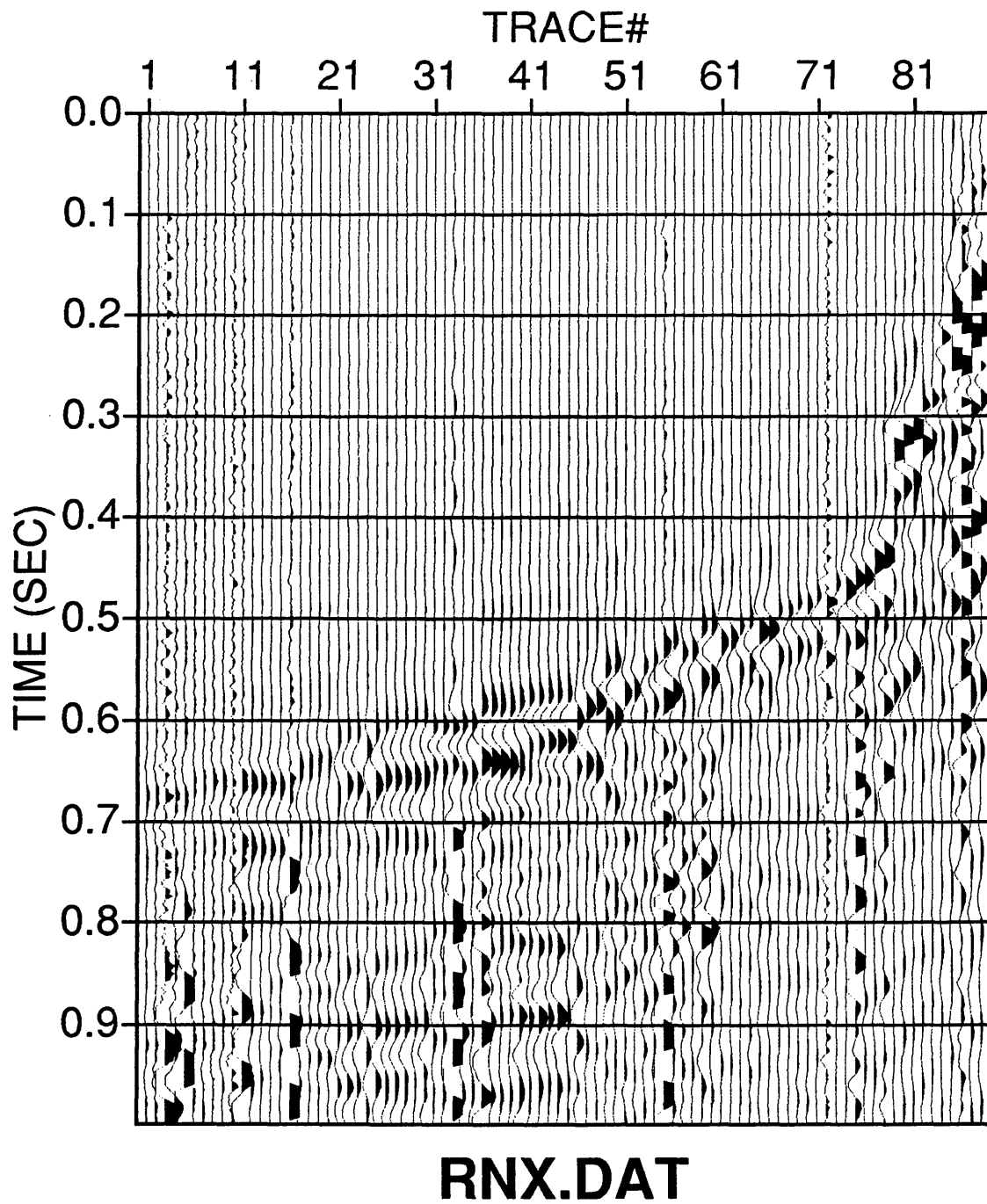


Figure 23: Horizontal (X) component from the near-offset radial shear-wave data.

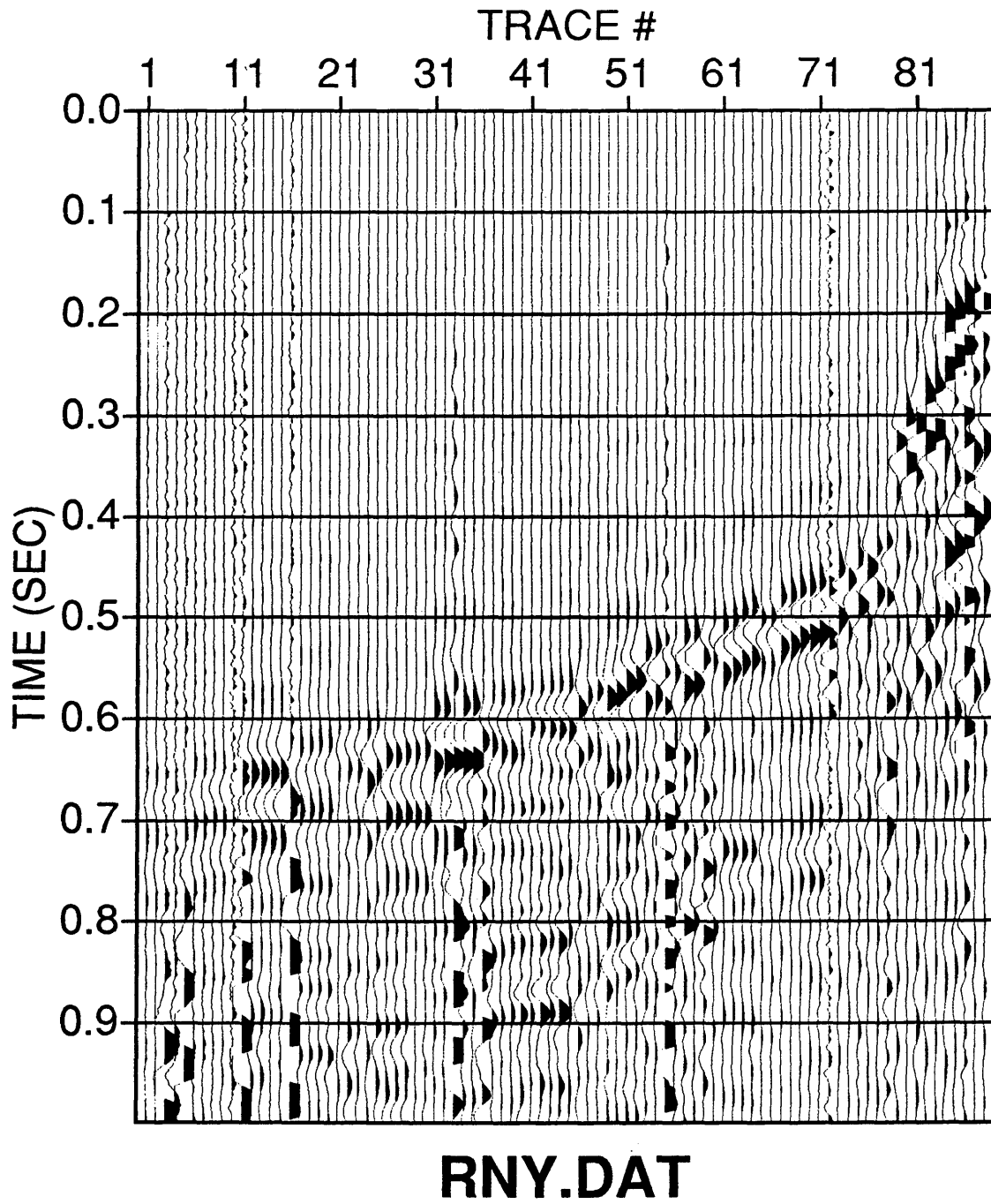


Figure 24: Horizontal (Y) component from the near-offset radial shear-wave data.

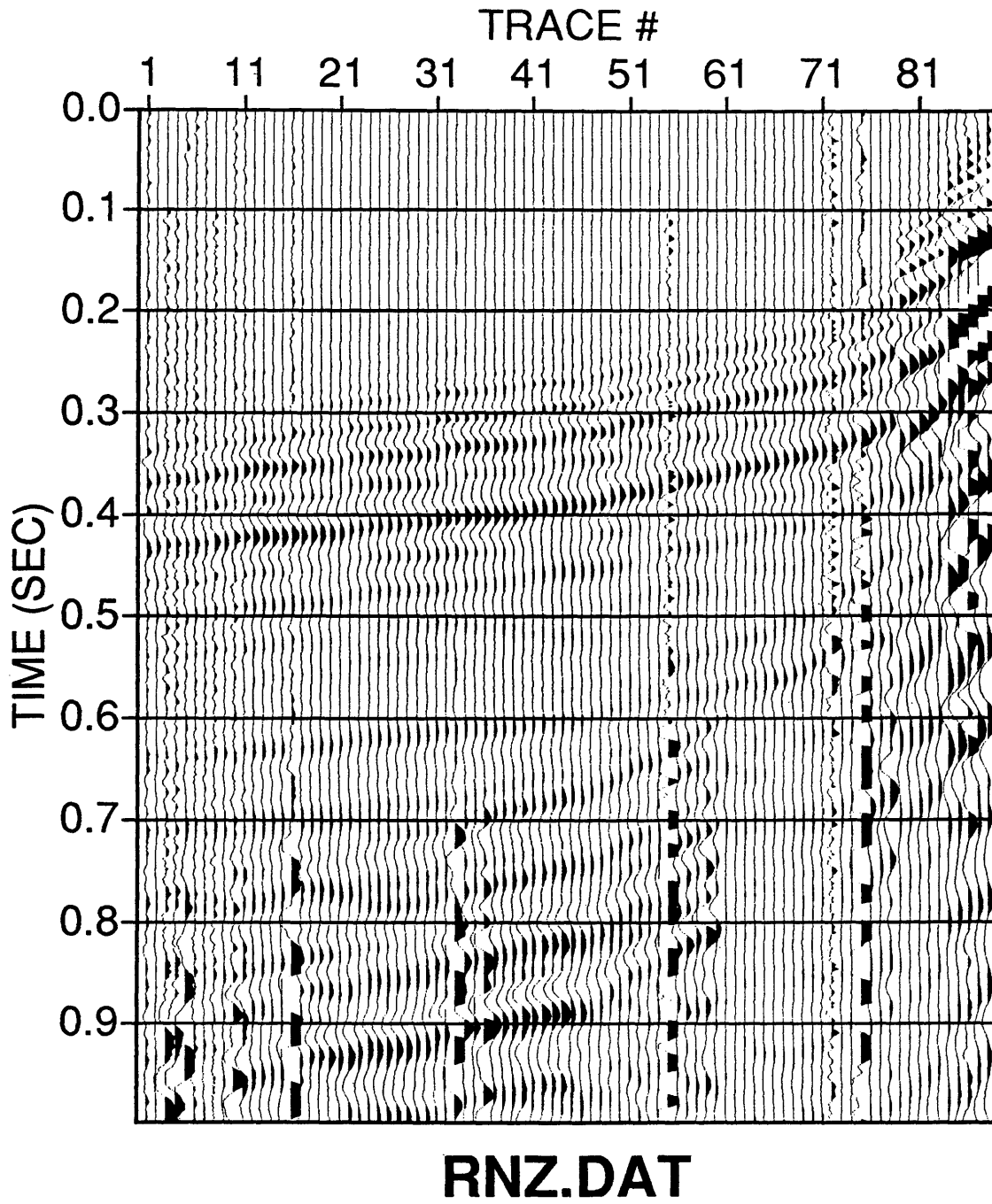


Figure 25: Vertical (Z) component from the near-offset radial shear-wave data.

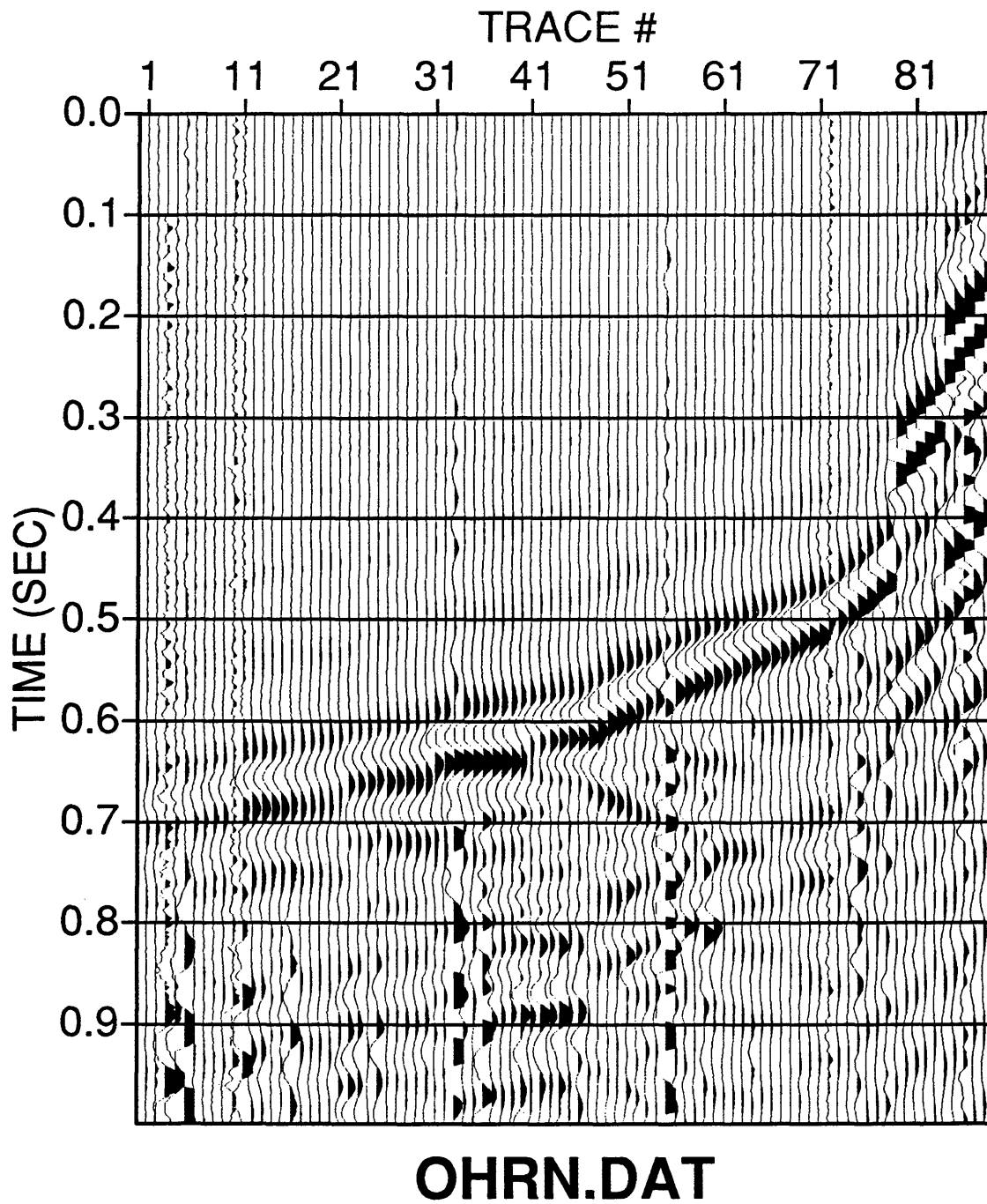


Figure 26: Horizontal near-offset radial shear-wave component oriented inline to the source receiver plane.

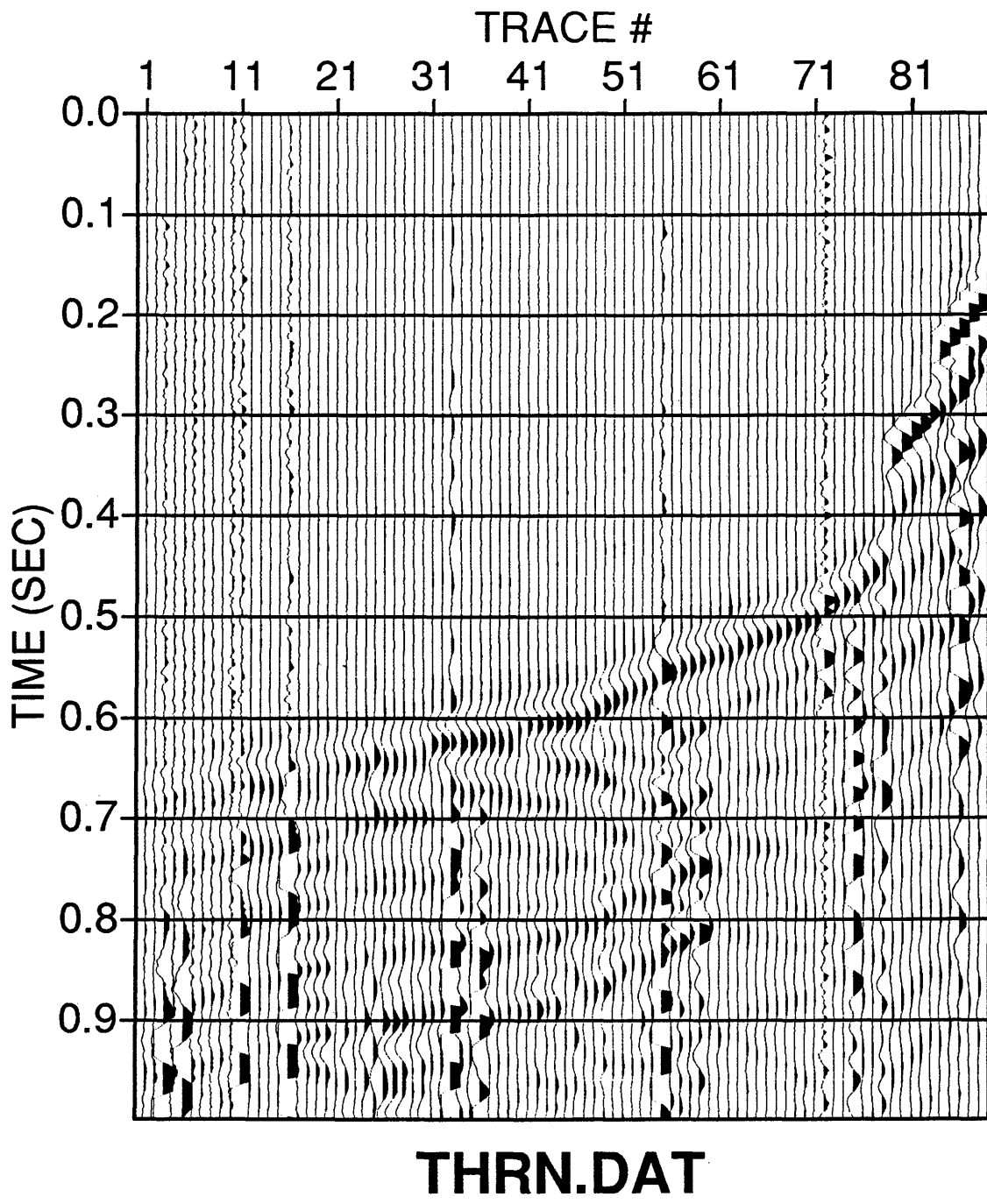


Figure 27: Horizontal near-offset radial shear-wave component oriented transverse to the source receiver plane.

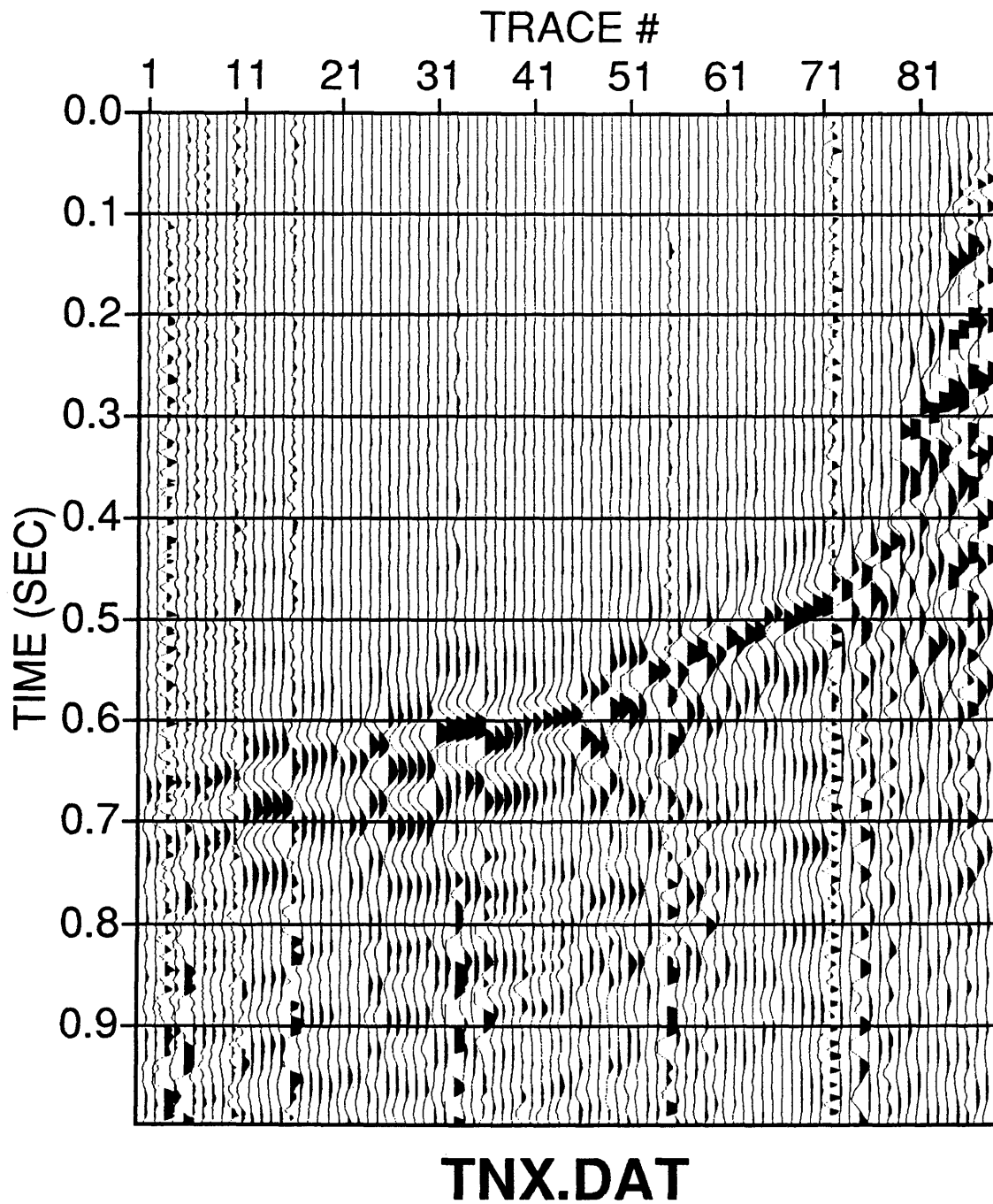


Figure 28: Horizontal (X) component from the near-offset transverse shear-wave data.

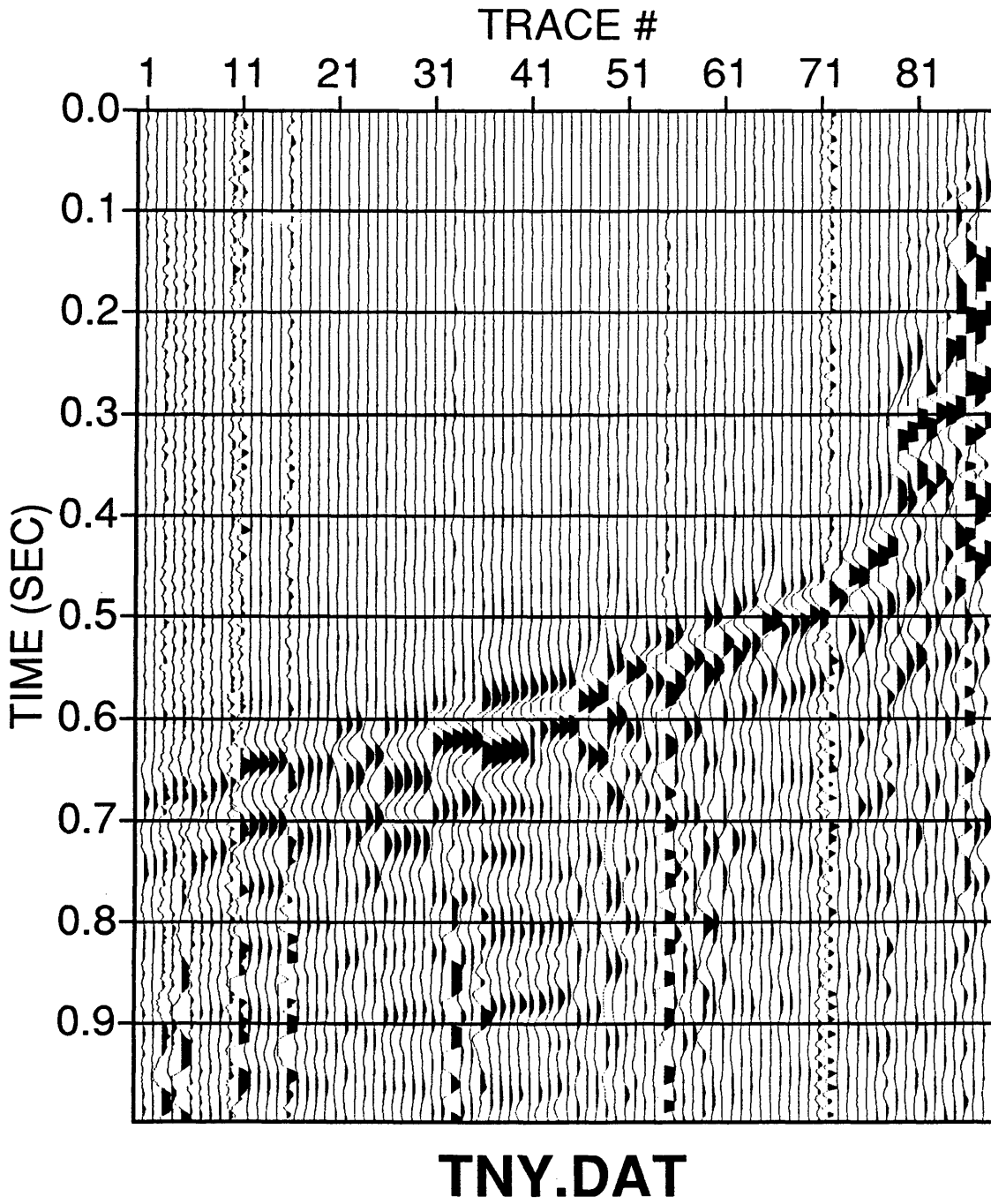


Figure 29: Horizontal (Y) component from the near-offset transverse shear-wave data.

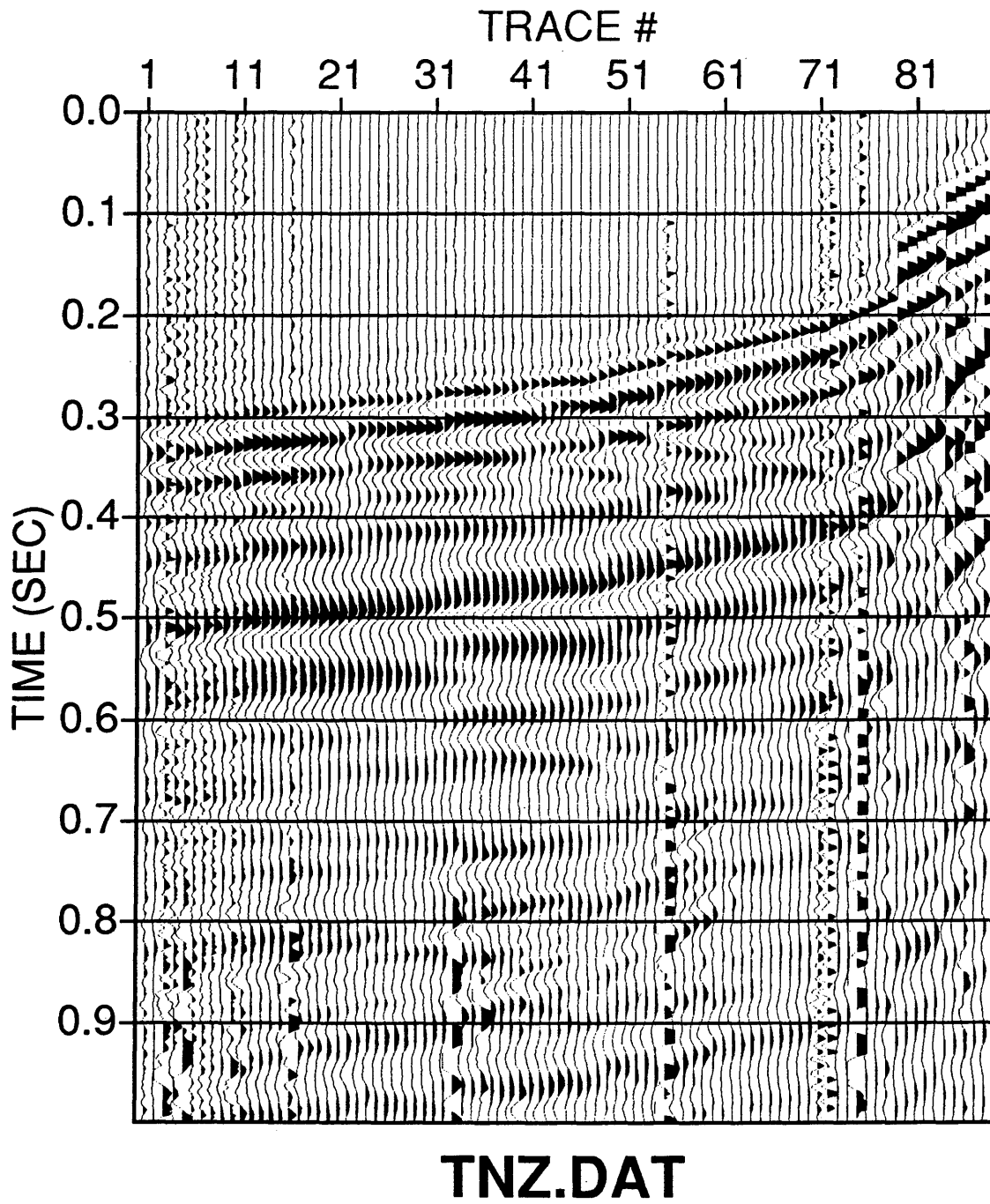
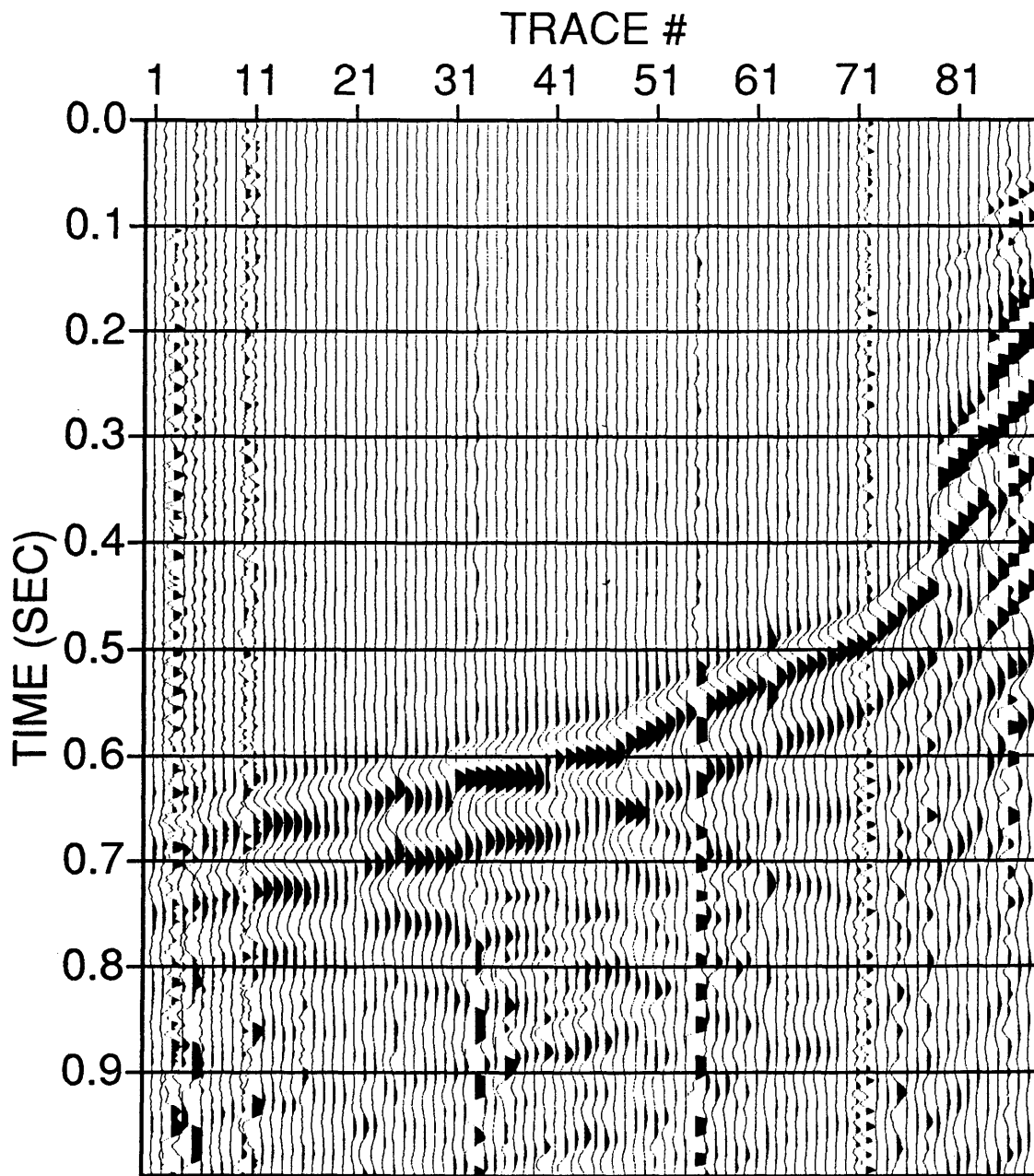


Figure 30: Vertical (Z) component from the near-offset transverse shear-wave data.



OHTN.DAT

Figure 31: Horizontal near-offset transverse shear-wave component oriented inline to the source receiver plane.

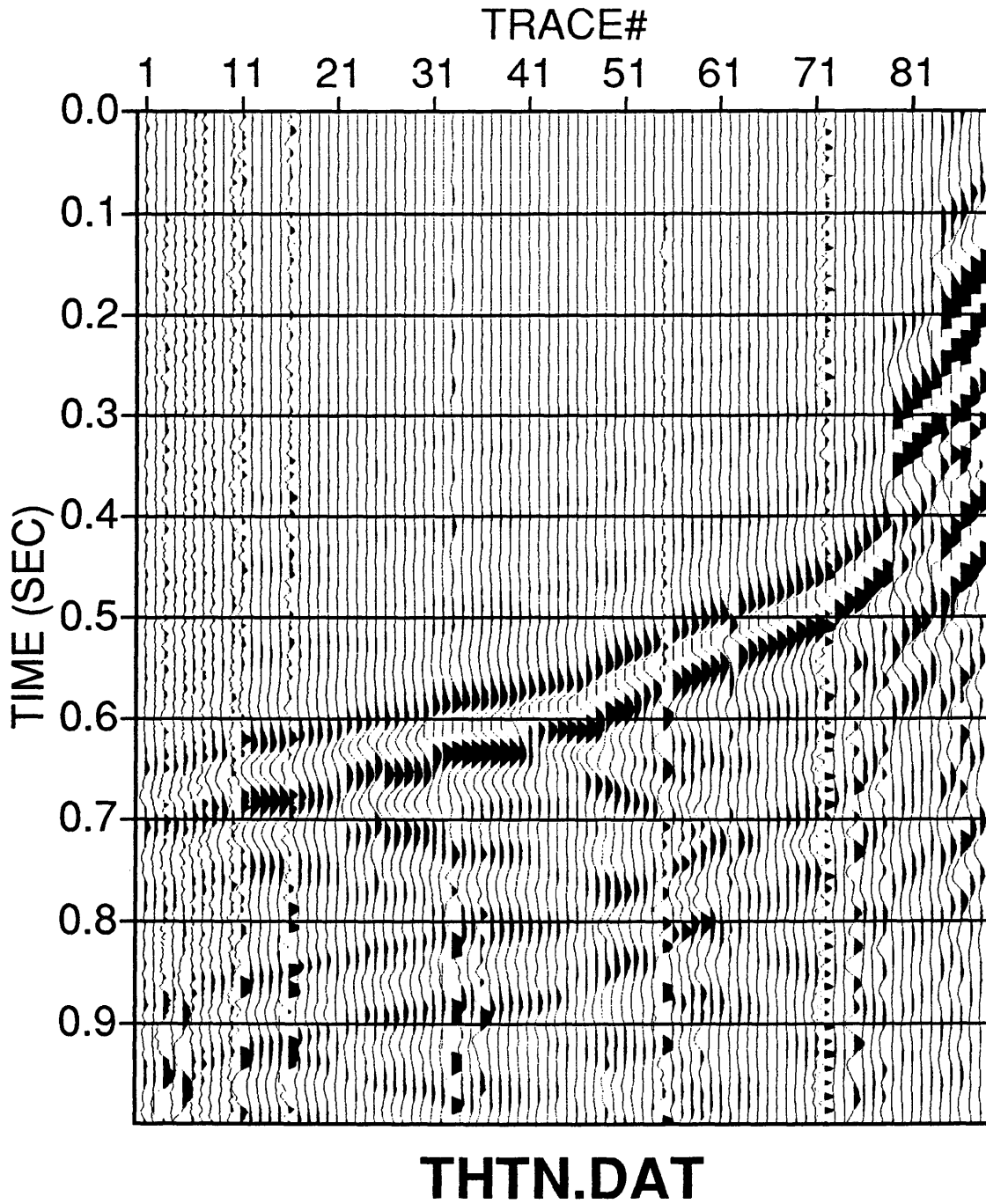


Figure 32: Horizontal near-offset transverse shear-wave component oriented transverse to the source receiver plane.

cross-line components in order to remove tool rotation. The results are shown in Figures 31 and 32. Shear-wave energy is recorded on the in-line component (Figure 31), once again indicating the presence of shear-wave splitting due to an azimuthally anisotropic medium. In addition, compressional energy can be readily observed on the vertical (Z) component (Figure 30), which has been output from the transverse shear-source.

Birefringence

Knowing that shear-wave birefringence has taken place within the subsurface, a second rotation of the data is necessary to determine the natural polarization of the fast shear-wave data. An accurate polarization angle using two horizontal polarized shear sources can be determined only if there is equal displacement of the sources, the output of the sources are similar, and coupling components of the horizontal receivers are equal, (Kramer, 1991).

The polarization angle is found by rotating the in-line and cross-line components of the radial and transverse shear-wave data until energy is maximized on the main diagonal components and minimized on the off-diagonal components. The above procedure is accomplished through the following four component rotation:

$$\begin{pmatrix} S1 & D1 \\ D2 & S2 \end{pmatrix} = R^T(\alpha) \begin{pmatrix} OHRN & THRN \\ OHTN & THTN \end{pmatrix} R(\alpha)$$

$$R(\alpha) = \begin{pmatrix} \cos[\alpha(d)] & -\sin[\alpha(d)] \\ \sin[\alpha(d)] & \cos[\alpha(d)] \end{pmatrix}$$

where

S1 = fast shear-wave data

S2 = slow shear-wave data

D1 = off-diagonal

D2 = off-diagonal

OHRN = in-line component of the radial source data

THRN = cross-line component of the radial source data

OHTN = in-line component of the transverse source data

THTN = cross-line component of the transverse source data

$\alpha(d)$ = polarization angle from source-receiver plane

T = matrix transpose

The results of the shear-wave data after transformation into its natural coordinate system are shown in Figure 33. The data were displayed at the same relative amplitude. Note that the data show minimal energy on the off-diagonals (D1 and D2), except in areas containing a lot of noise. Also, a time separation was calculated by cross-correlating the fast- and

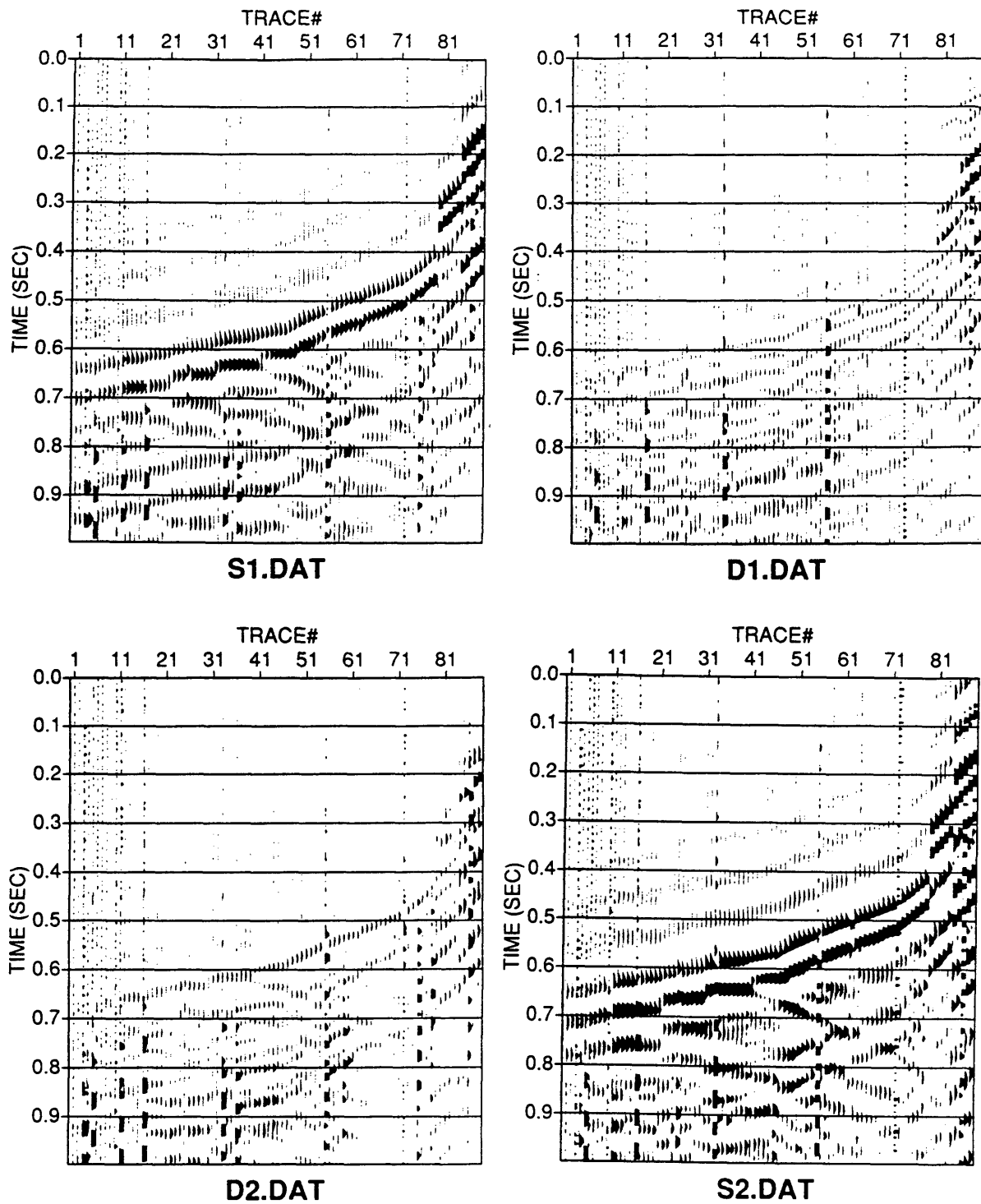


Figure 33: Results after four component rotation of the near-offset shear-wave data.

slow- shear-wave data in order to evaluate the subsurface anisotropy.

Figure 34 shows a plot of the polarization angles, cross-correlation time delays, and incidence angles at each receiver depth. The incidence angles were calculated through hodogram analysis of the vertical (Z) and oriented in-line near-offset P-wave components. The spikes in the three curves are inaccurate readings due to noisy traces at those receiver level positions. The average polarization angle between depths 2970 feet and 1000 feet (traces 1-79) is 56 degrees from the source-receiver plane. The source-receiver plane is at 263 degrees from North, therefore the fracture orientation is approximately at 319 degrees from North or North 41 degrees West (error of ± 5 degrees). At depths less than 1000 feet, the incidence angle increases to over 10 degrees and affects the Polarization angle and time separation as seen in Figure 34. This is due to the fast- and slow- shear-waves approaching shear-wave singularity which was discussed in the Theory section and is shown in Figure 7. In looking at the time separation curve, there is a constant 10 ms time delay between S1 and S2 throughout the data. Because a 10 ms time delay is observed at the first few receiver levels, shear-wave splitting is occurring at or near the surface of the earth. This is probably caused by anisotropy at the near surface.

Layer Stripping

The near-surface layers are characterized as being anisotropic, shown through evidence of a recorded 10 ms time delay between S1 and S2 at the first few receiver levels, (Figure 34). There is a possibility that the fracture orientation within the coal beds could be different from the orientation in the upper anisotropic layers. In order to find the correct orientation at depth, a method adopted by Winterstein and Meadows (1990) called layer stripping was applied to the data. This process includes polarizing the shear-wave data into the natural coordinate system of the upper anisotropic layer, then static shifting the slow shear-wave data (S2) until S1 and S2 are positioned at the top of the lower anisotropic layer. The procedure essentially places the sources at the top of the next anisotropic layer, so that a polarization angle can be found within the lower layers. An illustration of this process, taken from Winterstein and Meadows, is shown in Figure 35.

The shear-wave data, in-line and cross-line components of the radial and transverse shear-source data, were placed in the natural coordinate system of the upper anisotropic layer. In this case, the upper anisotropic layer is the interval between the surface and 2630 feet, depth to the top of the first coal. The data were rotated by 56 degrees, calculated

Layer Stripping Rationale

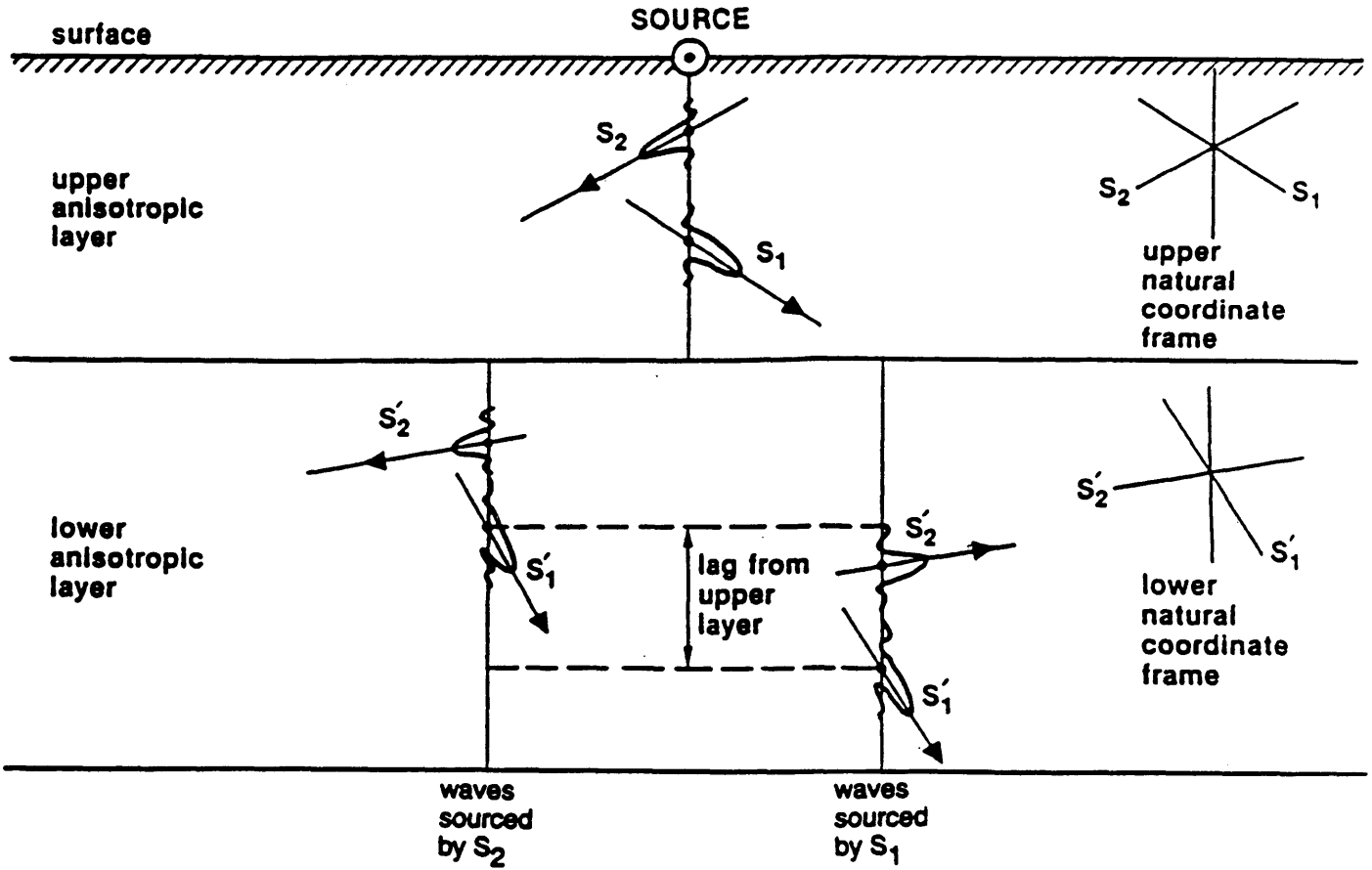
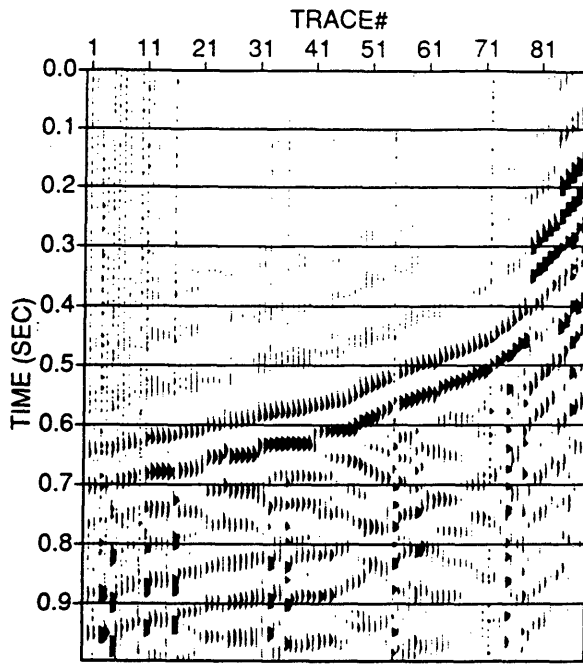


Figure 35: The layer stripping rationale used to determine a change in natural polarization direction with depth. (after Winterstein and Meadows, 1990)

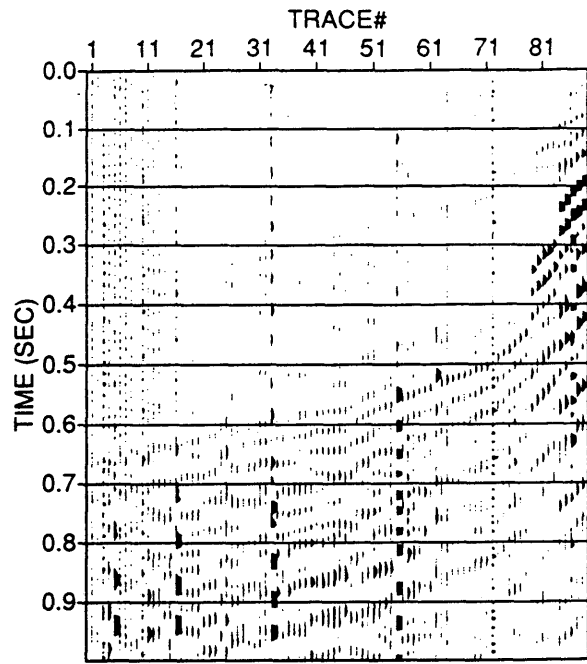
by four component rotation, to achieve natural polarization of the shear-wave data, (Figure 36). Then, the S2 and D2 components were static shifted by 10 ms to correct for the cumulative time delay down to the top of the coals. An additional four component rotation was then performed on the data below 2630 feet in order to find the natural coordinate system within the coals. A plot of the resulting polarization angles and time delay at each receiver level is displayed in Figure 37. No consistent polarization angle is observed, indicating the data are already in its natural coordinate system. Therefore, the polarized shear-waves at the near-surface are at the same orientation within the coals.

Processing of fast- and slow- shear-wave data

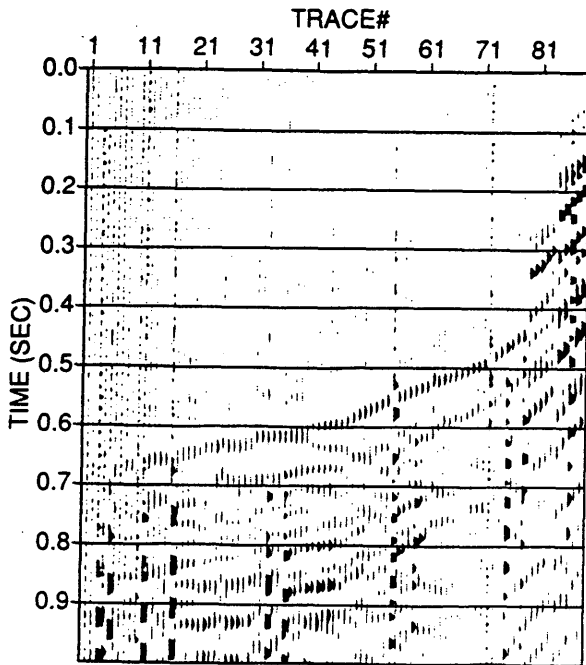
The processing of the fast- and slow- shear-wave data is very similar to the steps used for the near-offset compressional data. Figure 38 shows the processing flow diagram for the shear-wave data. The final corridor stacks are plotted in Figures 39 and 40, (S1 and S2, respectively). Figure 41 is a comparative plot of the two stacks in the area of the coal, intervals II and IV. There seems to be a good correlation between the coals of S1 and S2 with a two-way time delay of approximately 20 ms. The only noticeable difference is that S2 has a slightly higher amplitude than S1. A plot



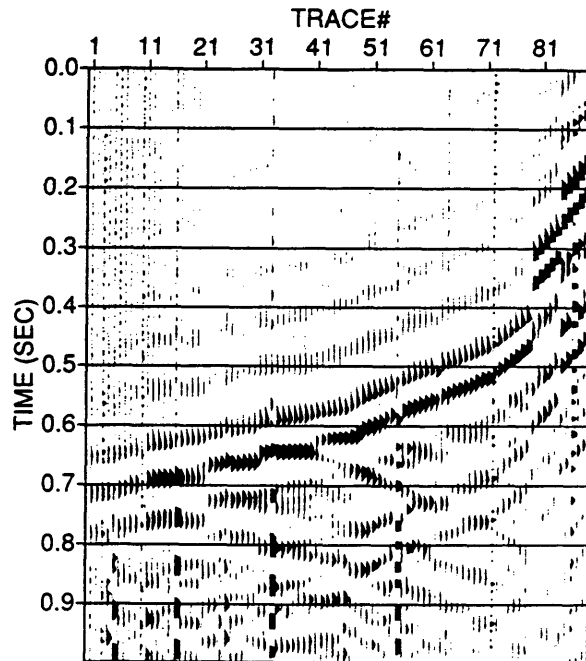
S156.DAT



D156.DAT



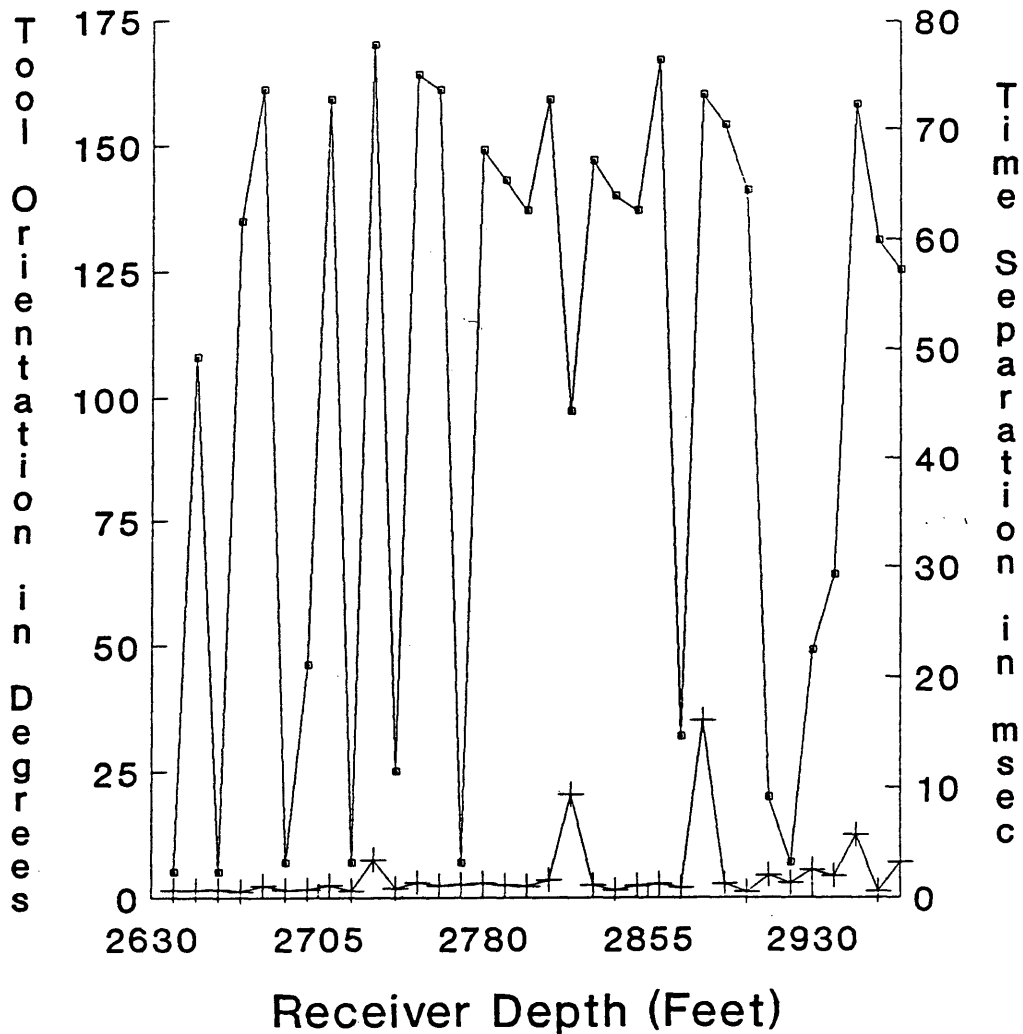
D256.DAT



S256.DAT

Figure 36: Results of the near-offset shear-wave components after four component rotation using a polarization angle of 56 degrees.

Polarization Angle after layer stripping



—□— Angle from S-R —+— Time Separation

Figure 37: Azimuthal polarization angle (relative to the source-receiver plane) of the fast shear-wave (upper curve) and time delay between the fast and slow shear-waves (lower curve) after layer stripping the first 2630 feet and removing 10 ms time delay.

showing the results of subtracting S2 from S1 is shown in Figure 42. The amplitude difference is due to the different travel paths of the fast- and slow- shear wave data causing reflection coefficient differences for S1 and S2. The S1 wave travels through the unfractured medium, whose velocities are the result of the fluids within the fractures, mineralogy, and the confining forces within the coal beds. Whereas the S2 wave travel through the fractured medium, whose velocities are governed by the intensity of fracturing, (Mueller, 1992).

In looking at the shear-wave corridor stacks, there are no high amplitude events above the coals, which is significantly due to a weakly anisotropic medium between the surface and the coals. This makes it easy to preserve the amplitude of the coals and possibly determine fracture intensity in the Cedar Hills Field through the 3-C 3-D survey.

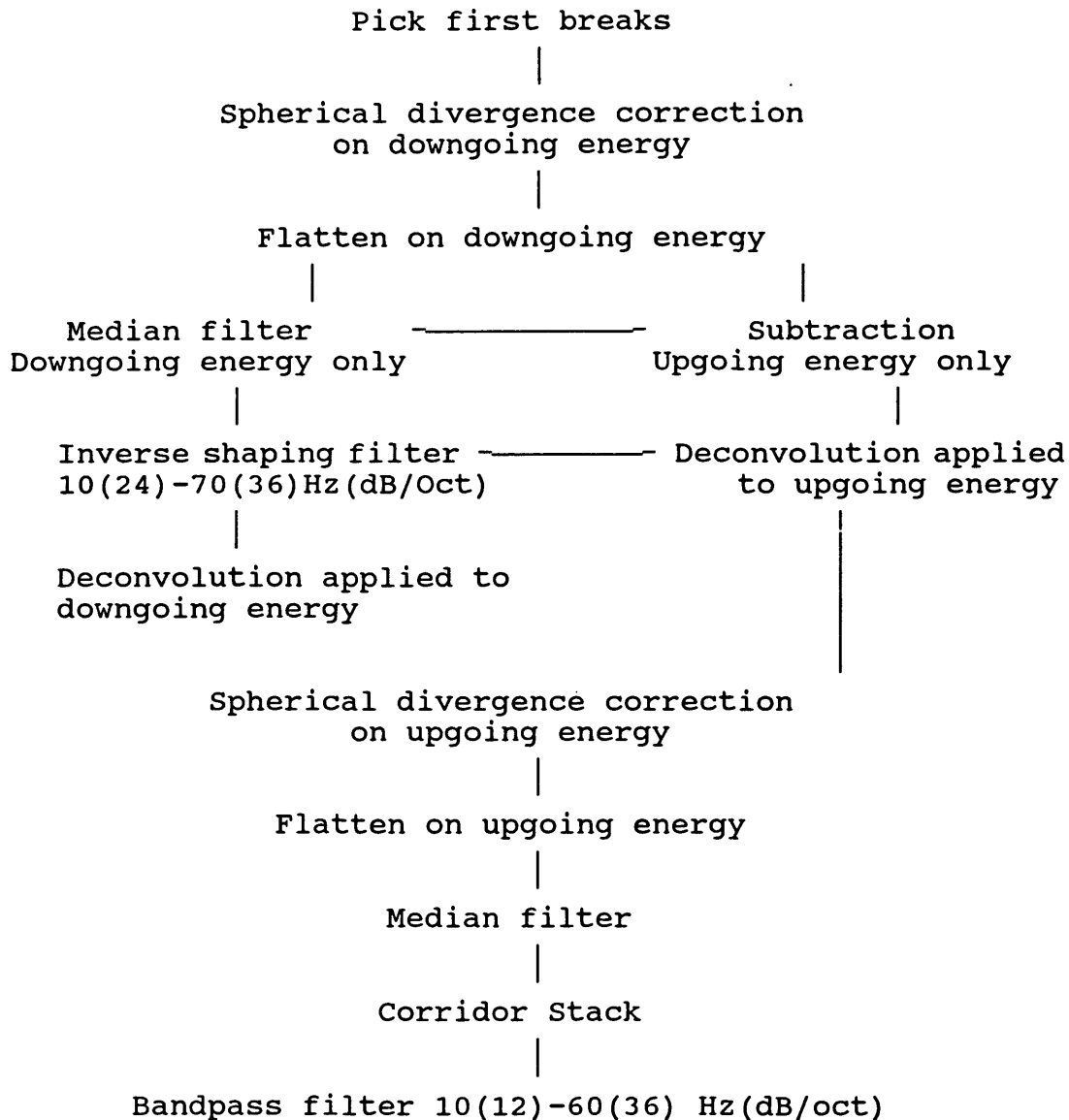


Figure 38: Processing flow for near-offset fast and slow shear-wave data.

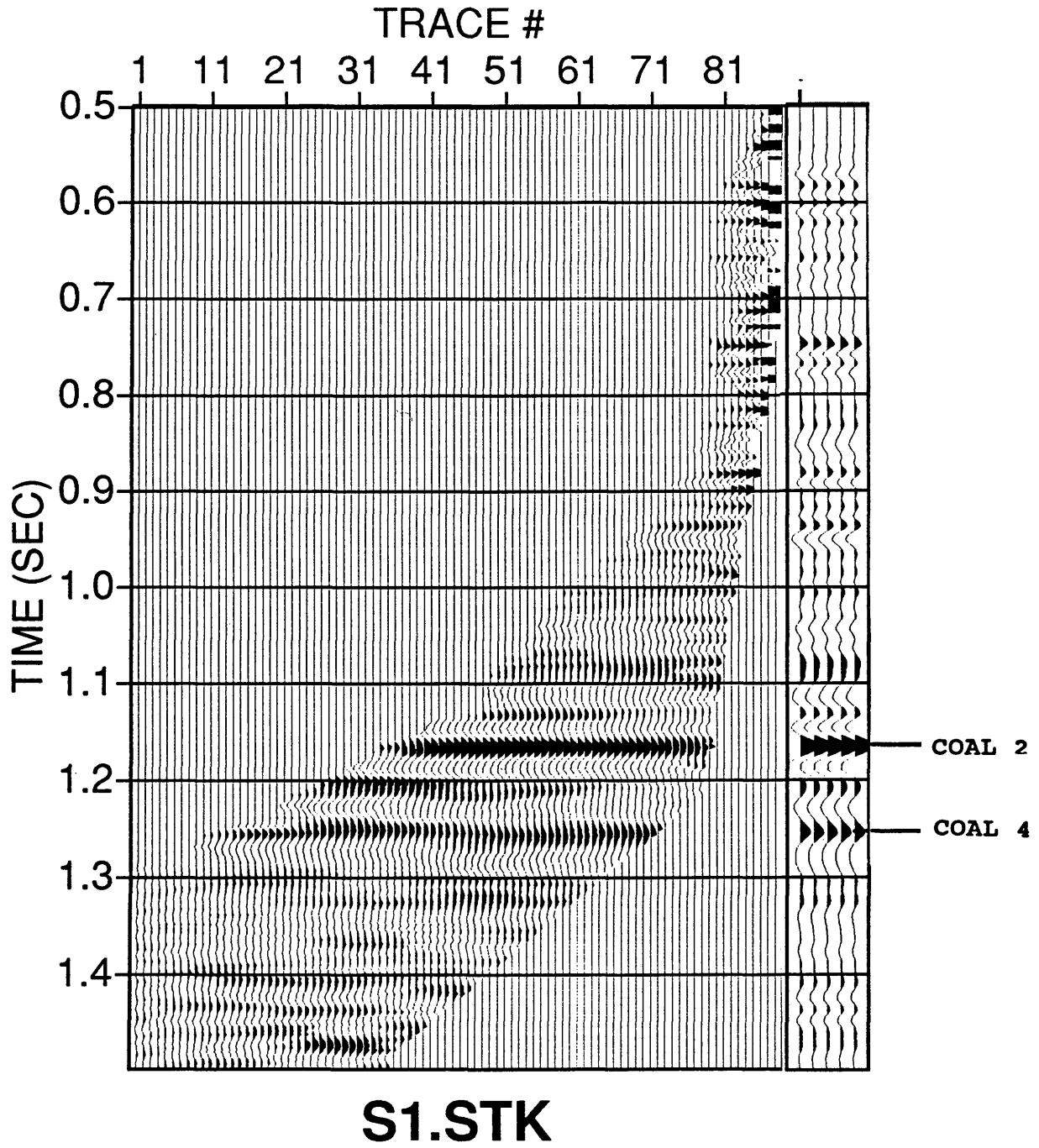


Figure 39: Unstacked and corridor stacked fast shear-wave data with a 10(124) - 50(36) Hz(dB/oct) bandpass filter.

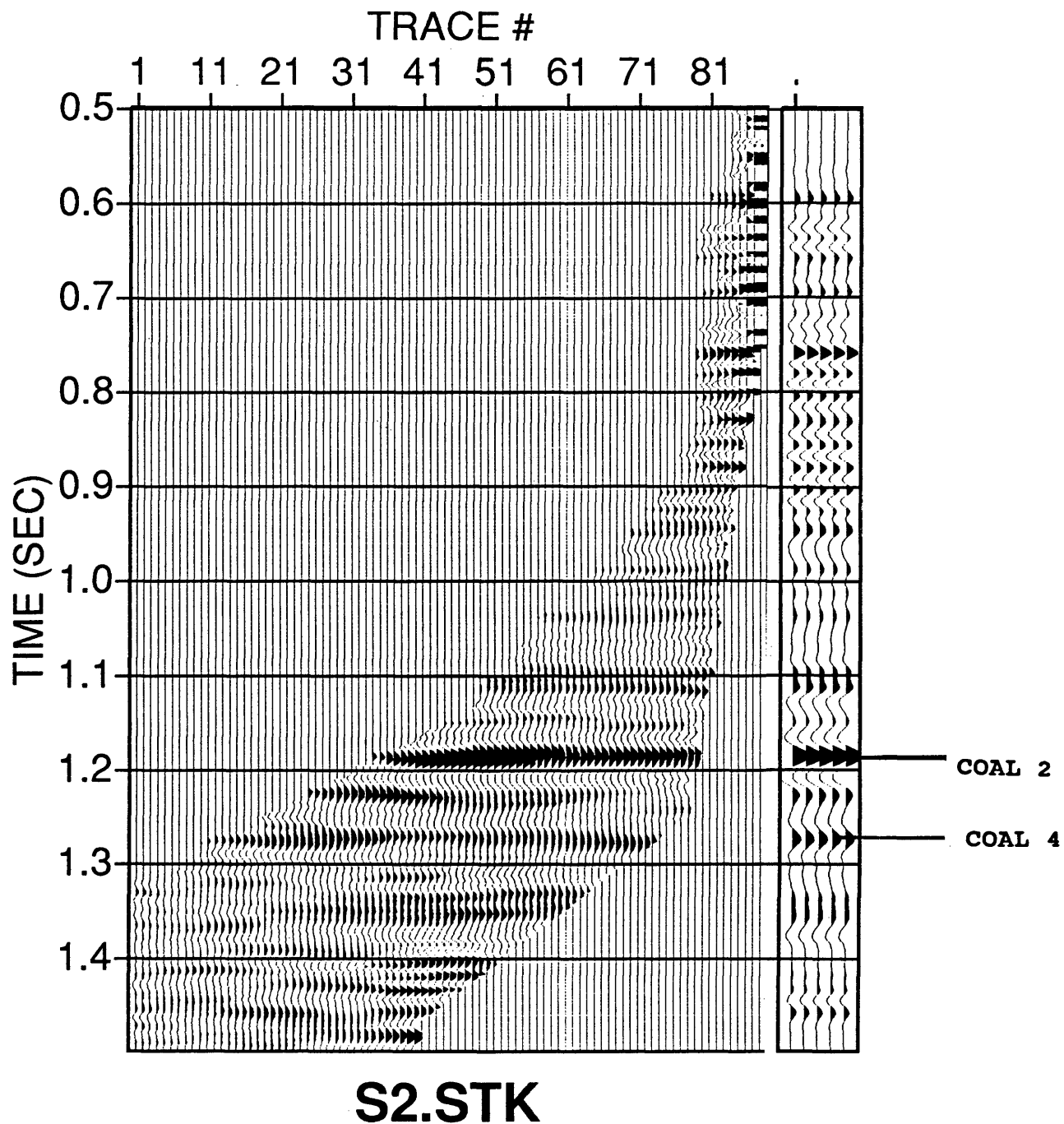


Figure 40: Unstacked and corridor stacked slow shear-wave data with a 10(124) - 50(36) Hz(dB/oct) bandpass filter.

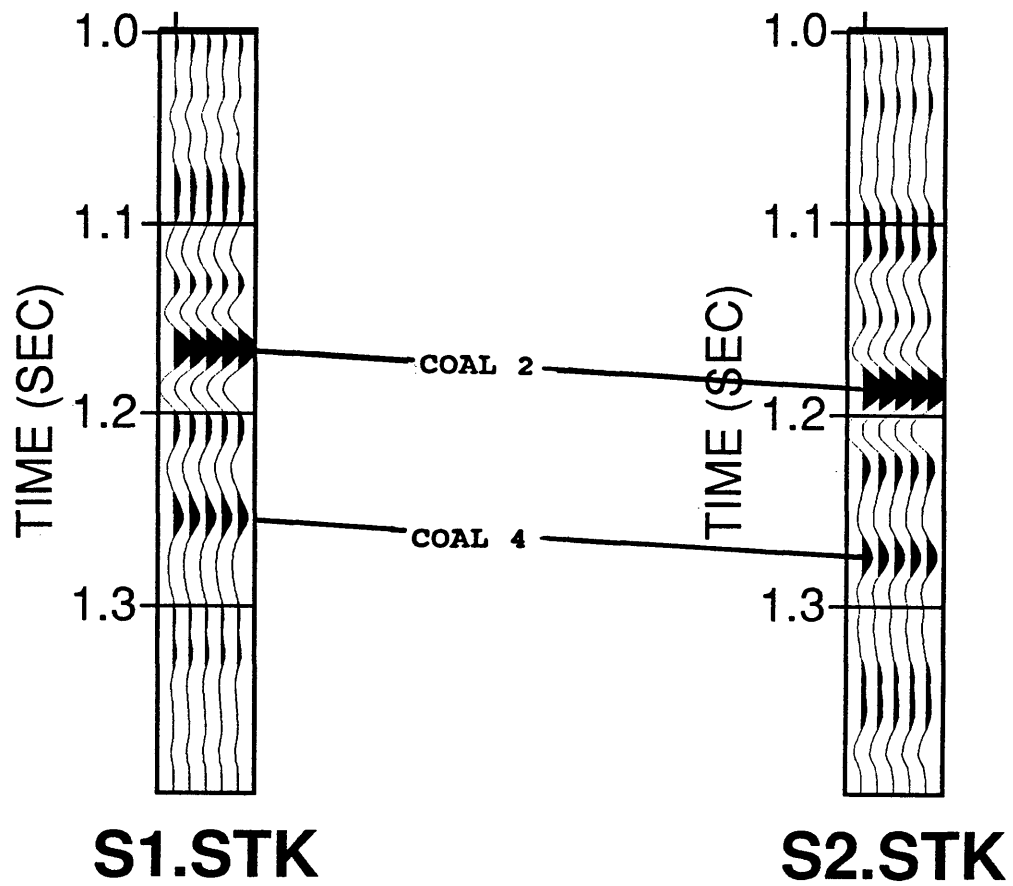


Figure 41: Comparison of the fast and slow shear-wave data in the coal interval.

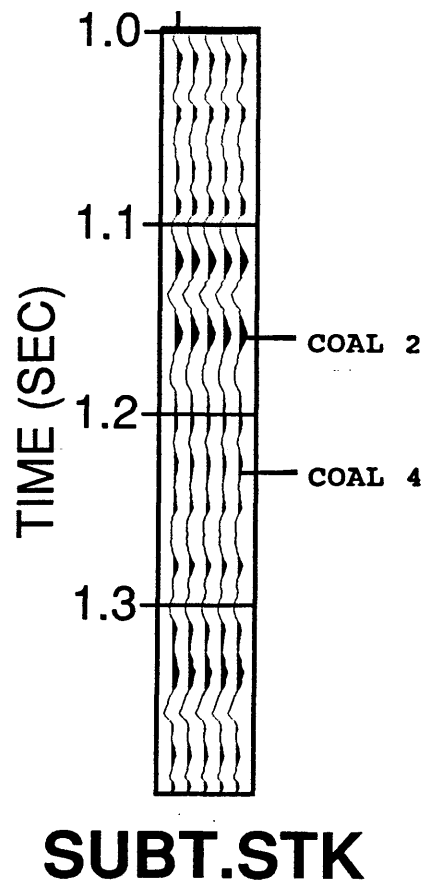


Figure 42: Results of subtracting the fast shear-wave data from the slow shear-wave data to show the amplitude difference.

BIREFRINGENCE AND GEOLOGY

A fracture analysis using core data between 2652 feet and 2887 feet from the Hamilton #3 well was conducted by TerraTek Core Services (1988). A summary of the report is as follows:

The face cleats strike predominantly from N20E to N50E (20 to 50 degrees from north) and dip to the northwest or southeast at angles greater than 70 degrees. Butt cleats strike N40W to N60W (120 to 140 degrees from North), dipping northeast or southwest at angles greater than 70 degrees. Of the three diagonal cleat sets, two strike at due north to N10E (0 to 10 degrees) and dip from due west to S80W (260 to 270 degrees from north) at angles greater than 80 degrees. The strike orientation for open (non-mineralized) fractures are variable, with most ranging from N30E to N80E (30 to 80 degrees). They dip generally to the northwest or southeast at widely varying angles. Filled fractures are highly variable in their strike orientation. The two calcite filled fracture sets have a strike trend between N20E and N30E (20 to 30 degrees), dipping from N60W to N70W (110 to 120 degrees) at angles greater than 80 degrees. The gouge filled fractures exhibit a variety of strike orientations and dip predominantly to the south at angles less than 65 degrees.

The natural polarization angle of N41W is oriented parallel to the reported butt cleat fractures. This indicates that the butt cleats are the open fractures caused by present day stresses. A rose diagram showing the fracture orientations and the natural polarization angle is displayed in Figure 43.

CLEAT ORIENTATION ROSE DIAGRAM
MESA OPERATING LIMITED PARTNERSHIP HAMILTON NO. 3

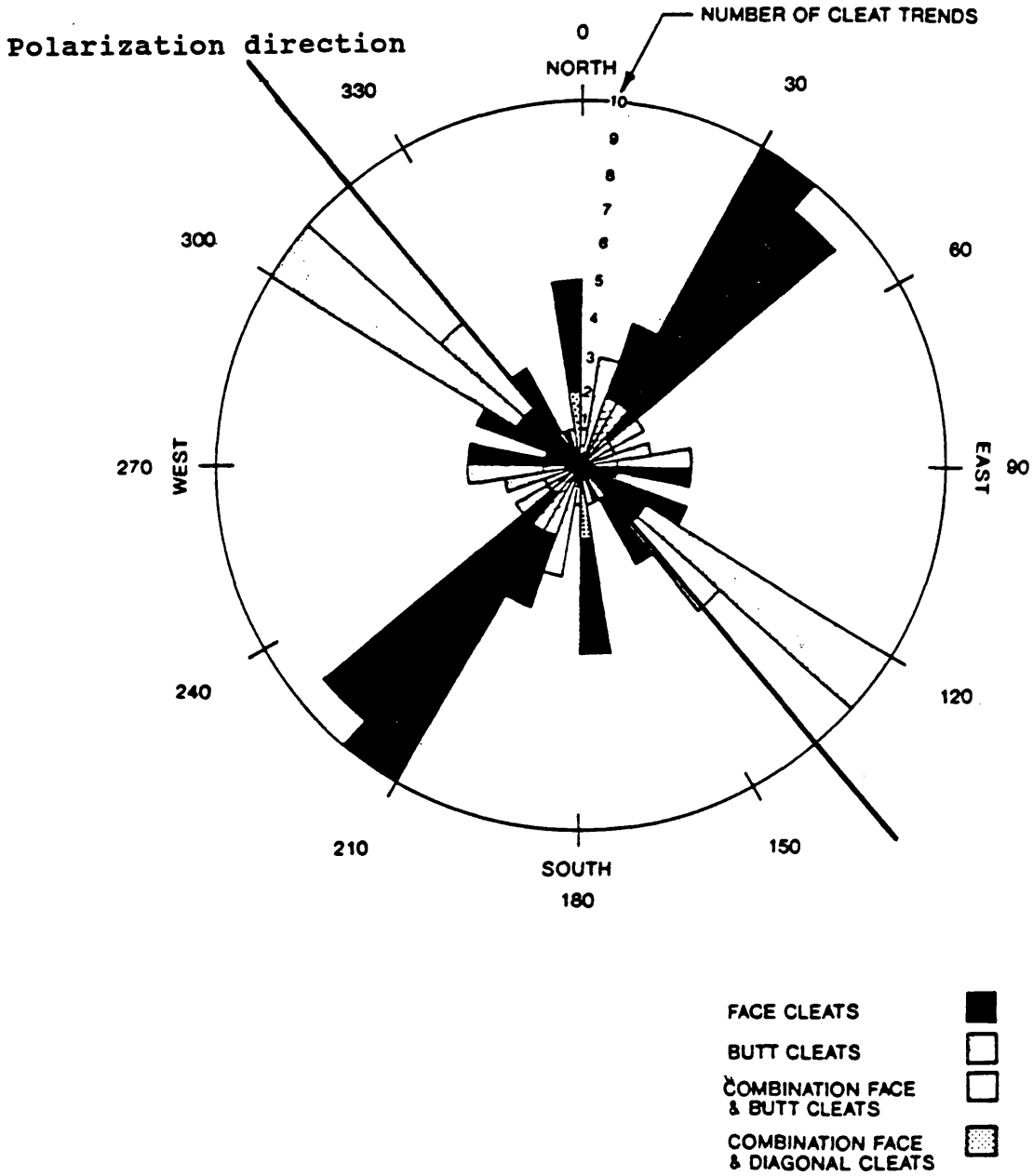
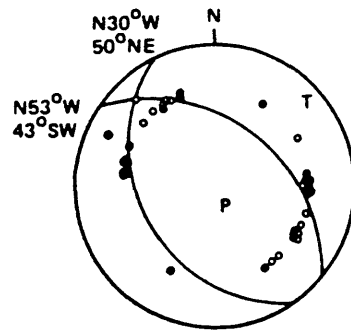


Figure 43: Rose diagram showing cleat orientation from core analysis and polarization angle from the VSP. (modified from the GRI Report, 1989)

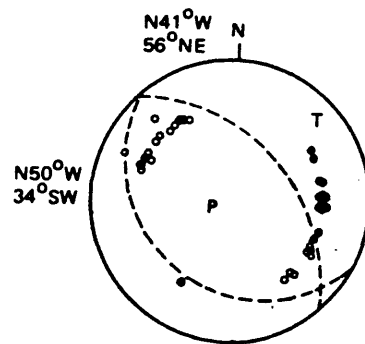
The most probable orientation for greater permeability is parallel to face cleats. But this is not always the case, maximum permeability may not be associated with the face cleat system at all. Subsequent tectonic events may develop new fracture systems with a higher permeability than the pre-existing cleat system. For instance, the present day horizontal stress field may have partially or totally constricted the face cleat system, where now the butt cleat system may control the direction of maximum permeability (Way, 1987).

A change in stress field has been documented by Humphrey and Wong 1989. They suggest that since the time of the Laramide Orogeny (northeast compressional forces), the San Juan Basin has been uplifted, causing a reversal of the stress field. Their results come from seismic monitoring of small to moderate earthquakes throughout the basin. Focal mechanisms showed normal faulting along northwest-striking planes and northeast minimum principal stress direction (Figure 44). Therefore, Humphrey and Wong characterize the present state of stress as a northeast-trending extension. This orientation in stress could cause the butt cleats to be the dominant open fractures.

A gas production rate map of the Cedar Hills Field is shown in Figure 45. There are two major trends within the



Crownpoint, NM
5 January 1976
M_L 4.6



Crownpoint, NM
5 March 1977
M_L 4.2

Figure 44: Focal mechanisms of earthquakes in the Colorado Plateau, New Mexico. Solid circles are compressional; open circles are dilatational first motions. (after Humphrey and Wong, 1989)

CEDAR HILL FIELD

Maximum Month-by-Month
Gas Production Rate 1982-1988

LEGEND

Normalized Gas Production Contours in MMCF per Month
Contour Interval 5 MMCF

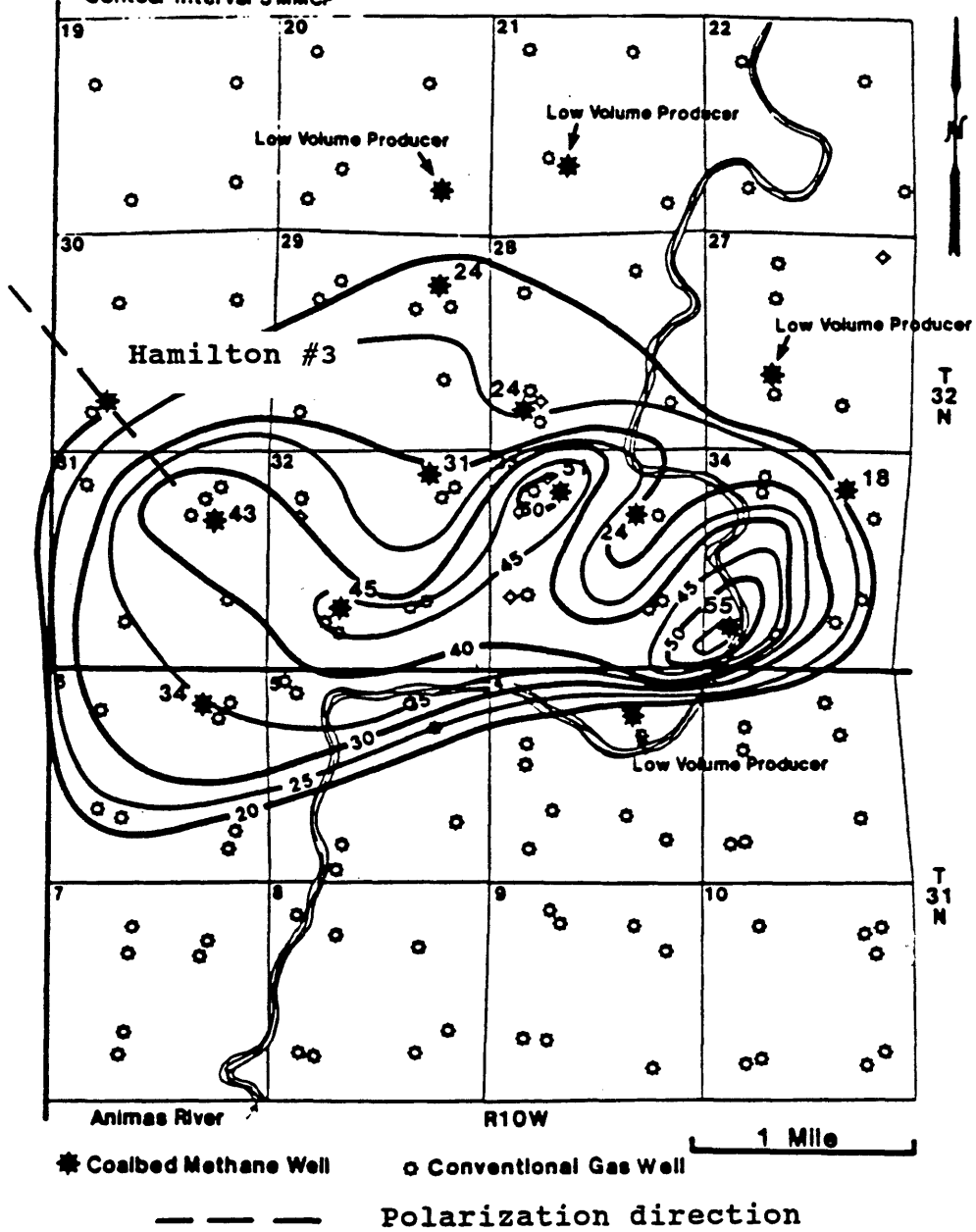


Figure 45: Gas production map in Cedar Hills area indicating the natural polarization within the coals. (modified from Mavor et.al., 1989)

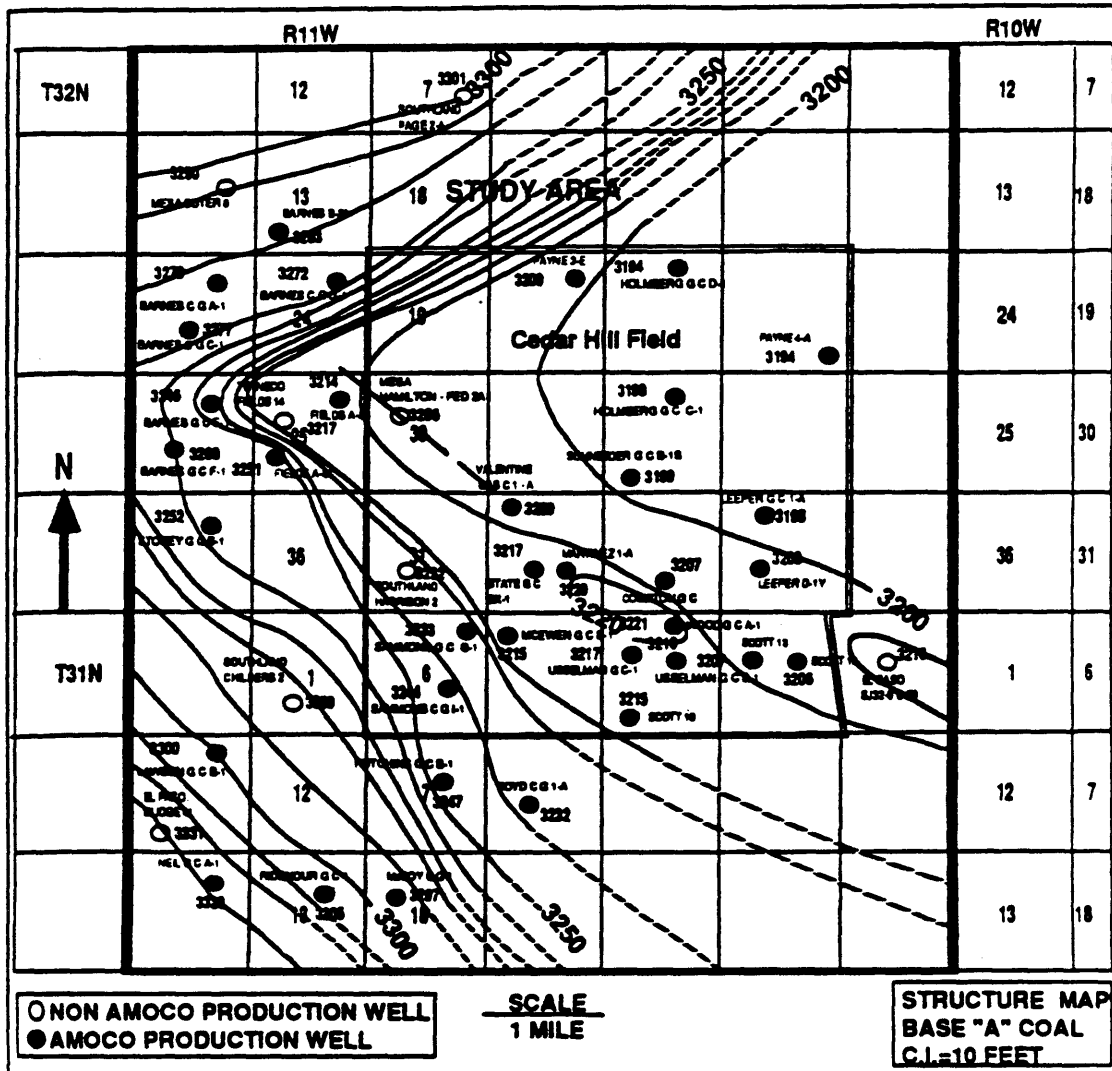
field; a primary northeast-southwest trend and a secondary northwest-southeast trend. In the vicinity of the Hamilton #3 well, the north-west production trend parallels the natural polarization angle within the coals.

Figure 46 shows a structure contour map at the base of the Basal Fruitland Coal (coal interval 4). The map shows a syncline trending northwest through the Cedar Hill Field. The southern limb of this syncline parallels the polarization angle indicated on the structure map.

As far as the credibility of the fracture analysis, the orientation survey of the core is possibly inaccurate. The report by TerraTek Core Services states:

Because of the condition of some of the core, and because portions of the core were cut into one foot lengths at rig-site, it is difficult to determine how continuous the orientation survey data is, and how rotations and breaks in the data relate to the core. Orientation survey azimuth plots were constructed from the survey data to help determine which portions of the core could be oriented. There are probably breaks and spins in the core that could not be seen and thus some of the fracture orientation data may be inaccurate.

In light of this problem, observations in stress direction, production rates, and structure show strong evidence of a north-west open fracture orientation.



--- Polarization direction

Figure 46: Structure map of the base of coal interval 4 in the Cedar Hills area indicating the natural polarization angle within the coals. (modified from Johnson, 1991)

FAR-OFFSET COMPRESSIONAL-WAVE VSP

By processing the far-offset P-wave VSP, two objectives were accomplished; observation of reflection characteristics within the coals and the amount of converted SV energy output from the compressional source. The processing steps performed on the far-offset data are slightly different than on the near-offset.

The in-line and cross-line components of our far-offset data are displayed in Figures 21 and 22, (see Tool Orientation section). Because the source is offset, hodogram analysis was performed using the in-line (OHPF) and vertical (Z) component in calculating the incident angles of the direct P-wave arrivals. The vertical incidence angles at each receiver depth are plotted in Figure 47. The angles are then used to rotate the data into a in-line vertical component (OVPF) which maximizes the down-going P-wave energy and a transverse vertical component (TVPF) which minimizes down-going P-wave energy, (Figure 48). The formulas used in rotation are as follows:

$$OVPF = Z(t, d) \cos[\phi(d)] + OHPF \sin[\phi(d)]$$

Vertical Incidence Angles Far-Offset VSP

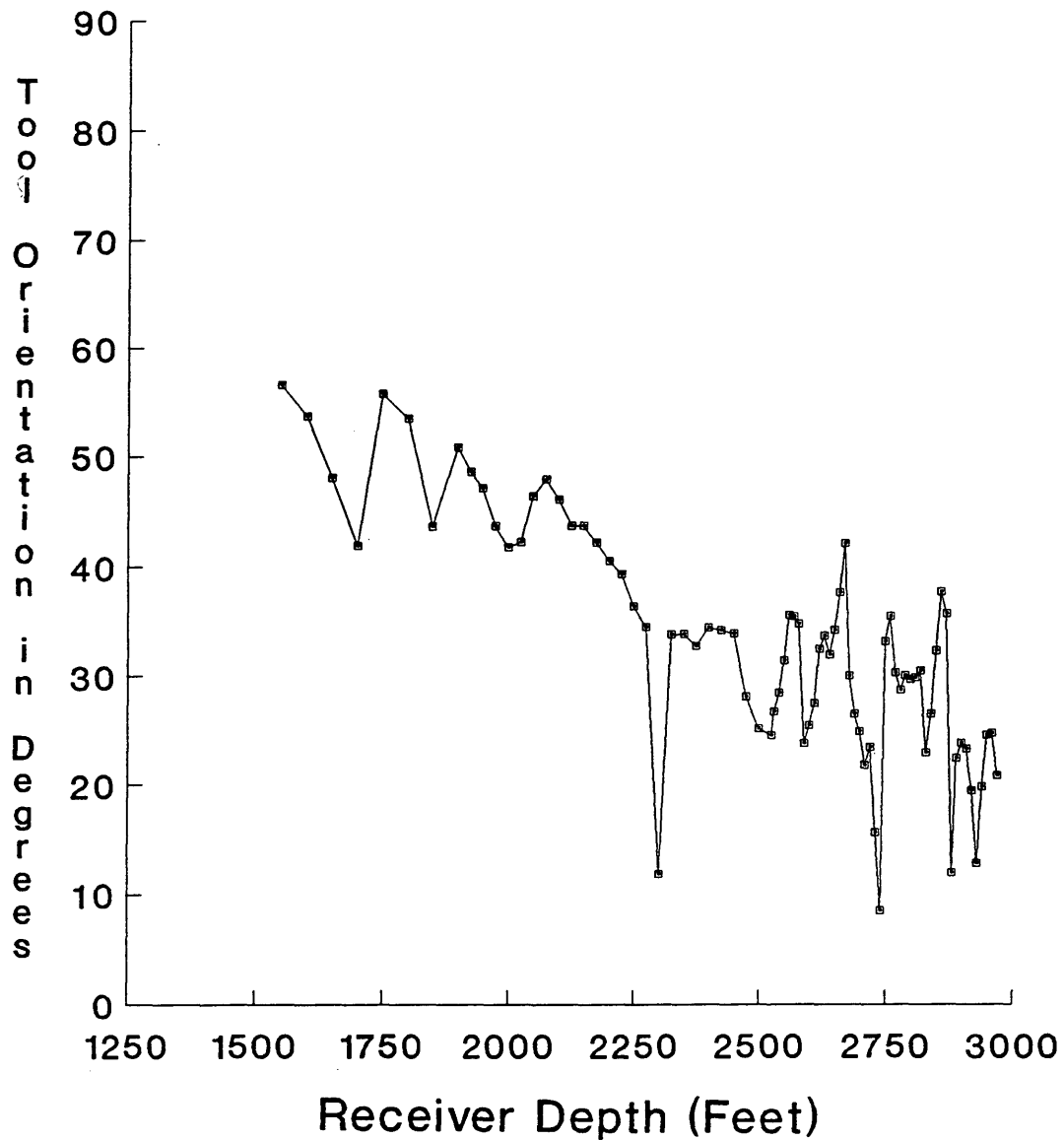


Figure 47: Vertical incidence angles found through hodogram analysis of the near-offset P-wave inline (OHPF) and vertical (Z) component.

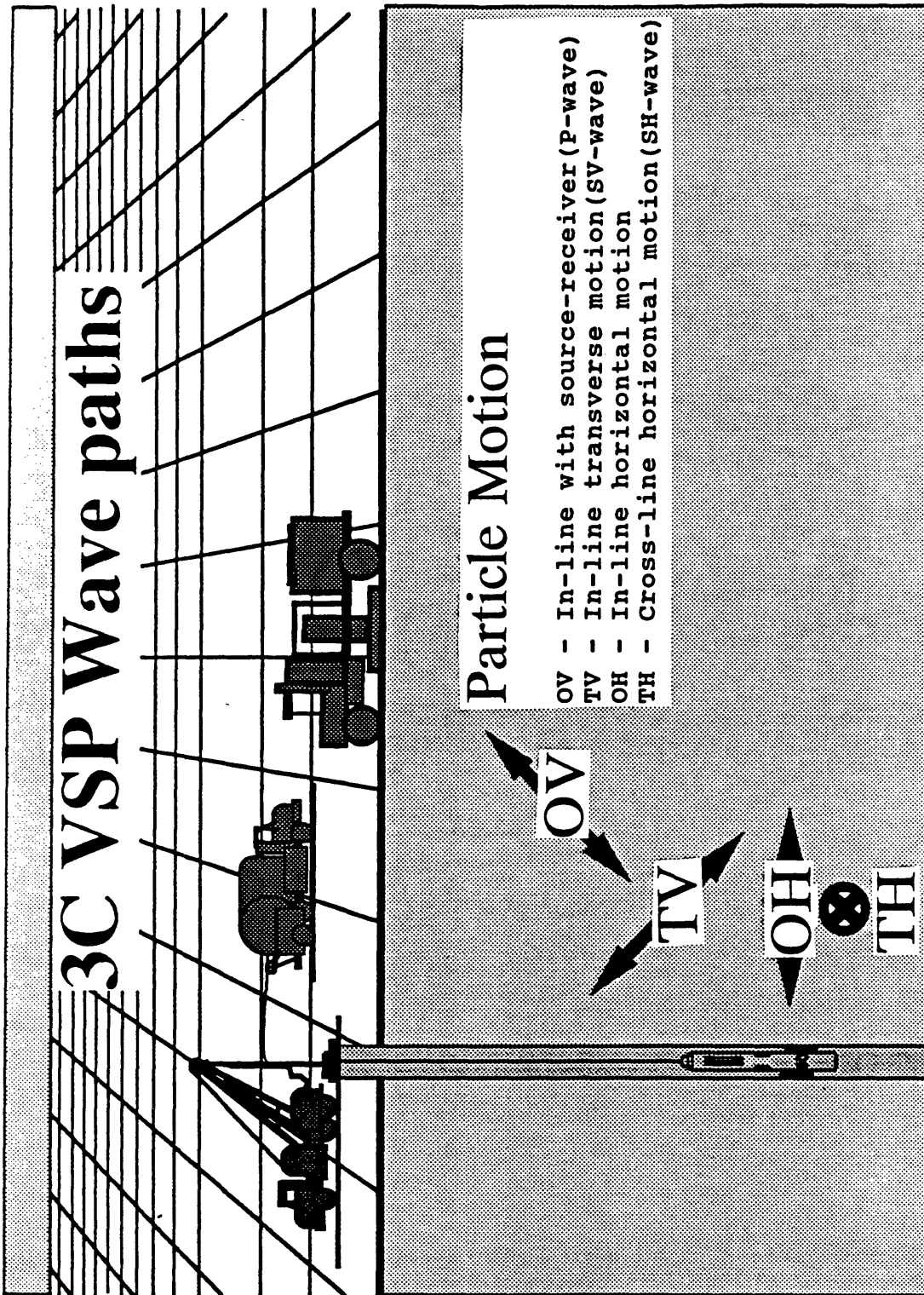


Figure 48: Particle motions for downgoing waves after corrected tool orientations. (after Kramer, 1991)

$$TVPF = -Z(t, d) \sin[\phi(d)] + THPF \cos[\phi(d)]$$

where $\phi(d)$ is the vertical incidence angle. The inline and transverse vertical components are displayed in Figures 49 and 50.

The next step is to separate the down-going energy from the up-going energy. This was accomplished by flattening on the first breaks and applying a 12 point median filter to both the OVPF and TVPF components. The down-going energy from OVPF component (Figure 51), contains predominantly compressional energy, whereas the down-going energy from TVPF component (Figure 52), contains predominantly SV-wave energy. The up-going energy was found simply by subtracting the down-going energy from the pre-median filtered data. The up-going energy on the two data sets are shown in Figures 53 and 54.

The up-going data sets contain both P-wave and SV-wave energy. The separation of these two energies required a time variant orientation. The time varying angles used for the rotation were calculated through a raytracing program within the HGS VSP software package. The program requires a velocity model of the subsurface, which was estimated by examining the well logs, a full-waveform inversion on the near-offset P-wave corridor stack, and the first arrivals of the compressional wave data. Table II summarizes the velocity model by giving

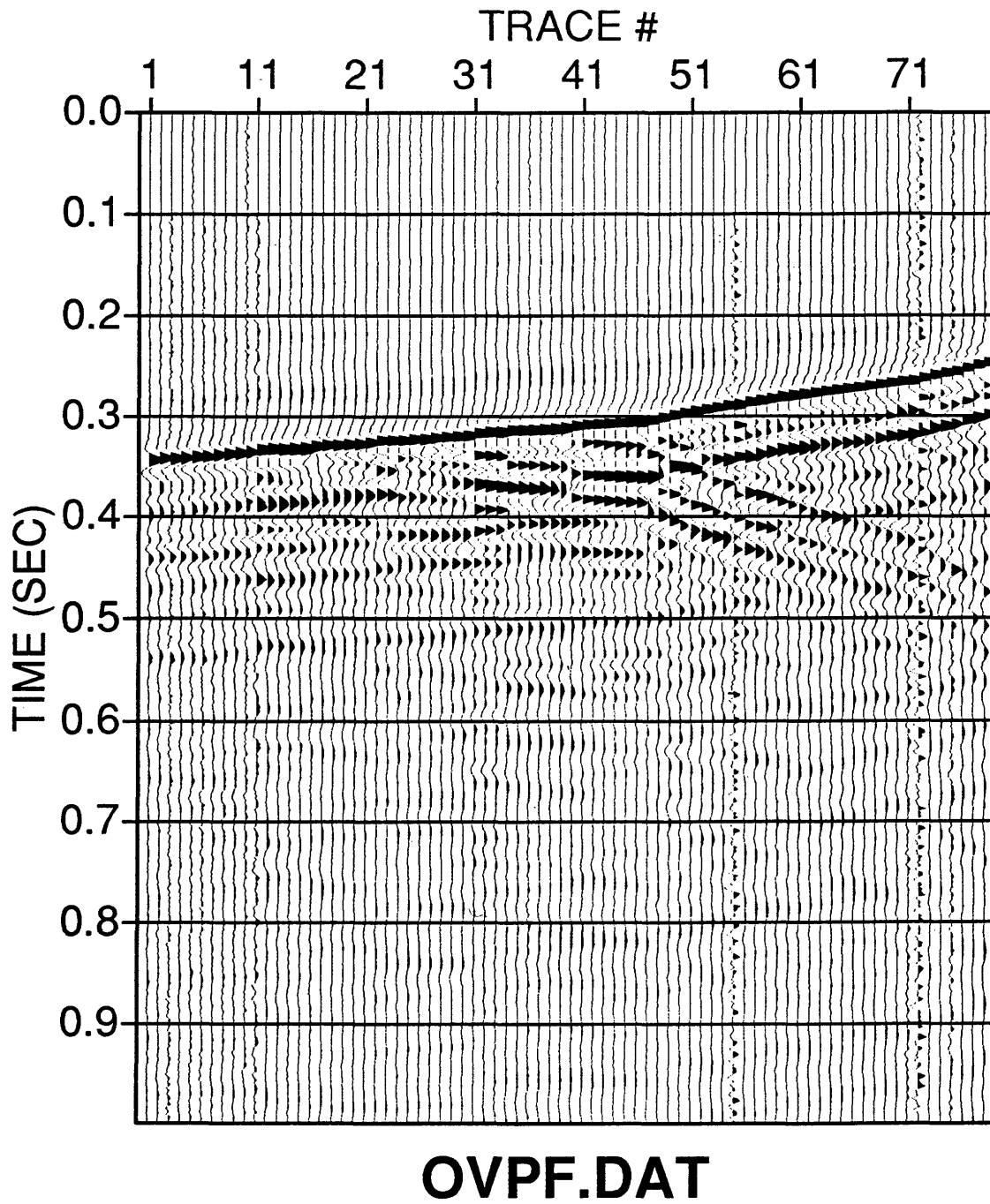


Figure 49: Vertical far-offset P-wave component oriented inline to the source receiver plane. Maximizing down-going compressional energy.

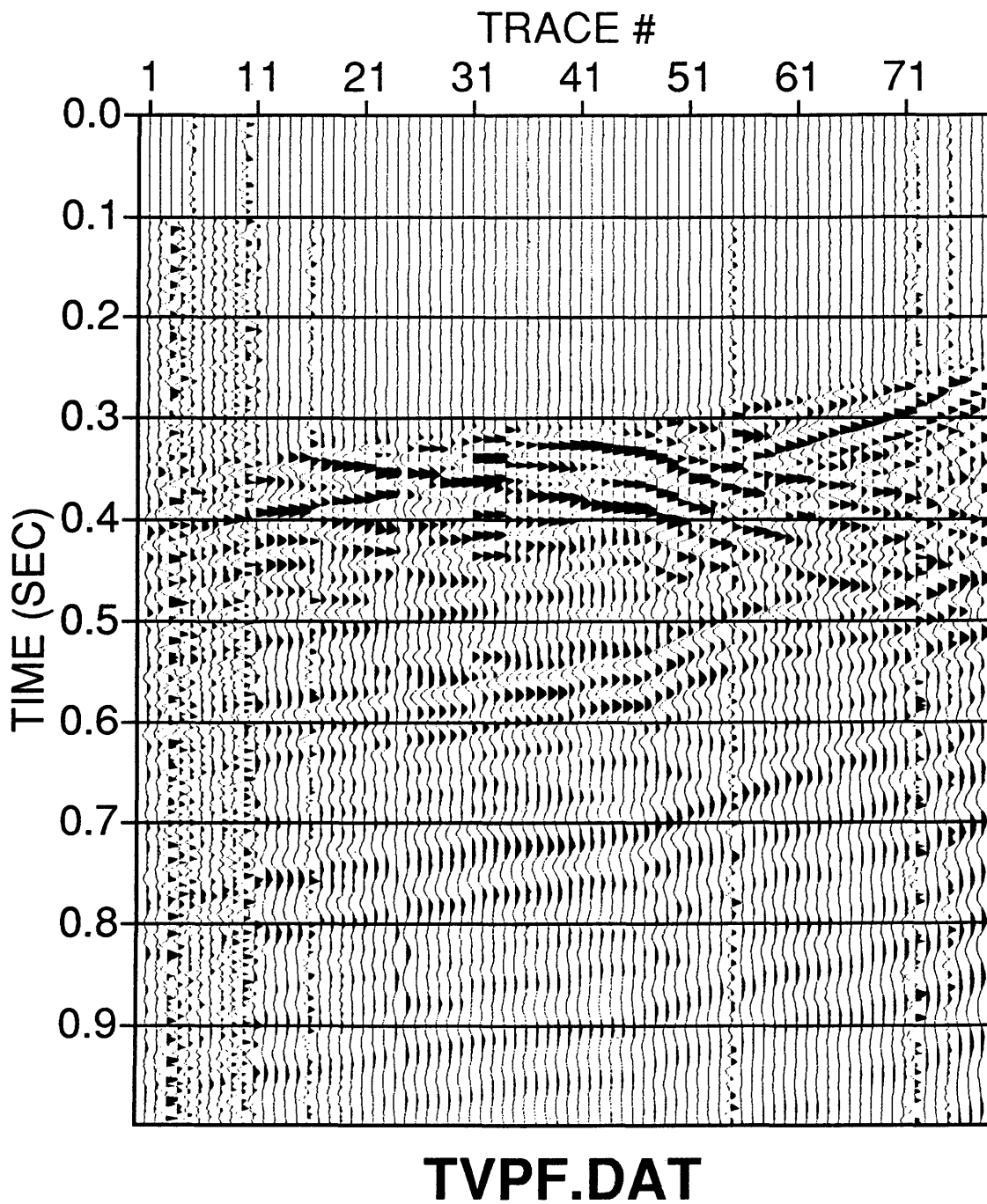


Figure 50: Vertical far-offset P-wave component oriented transverse to the source receiver plane. Maximizing down-going SV energy.

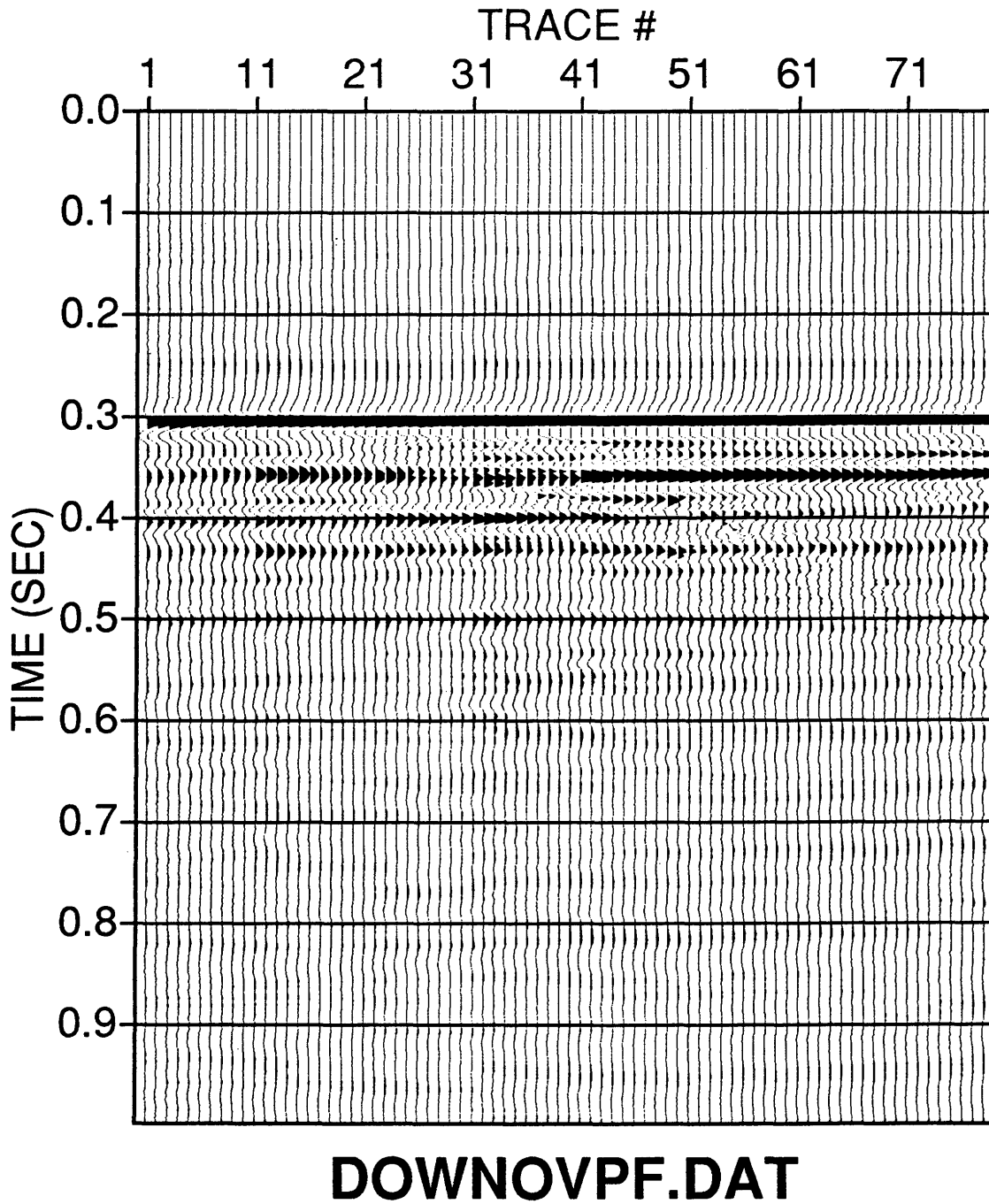


Figure 51: Down-going compressional data computed by median filtering of the inline component (OVPF).

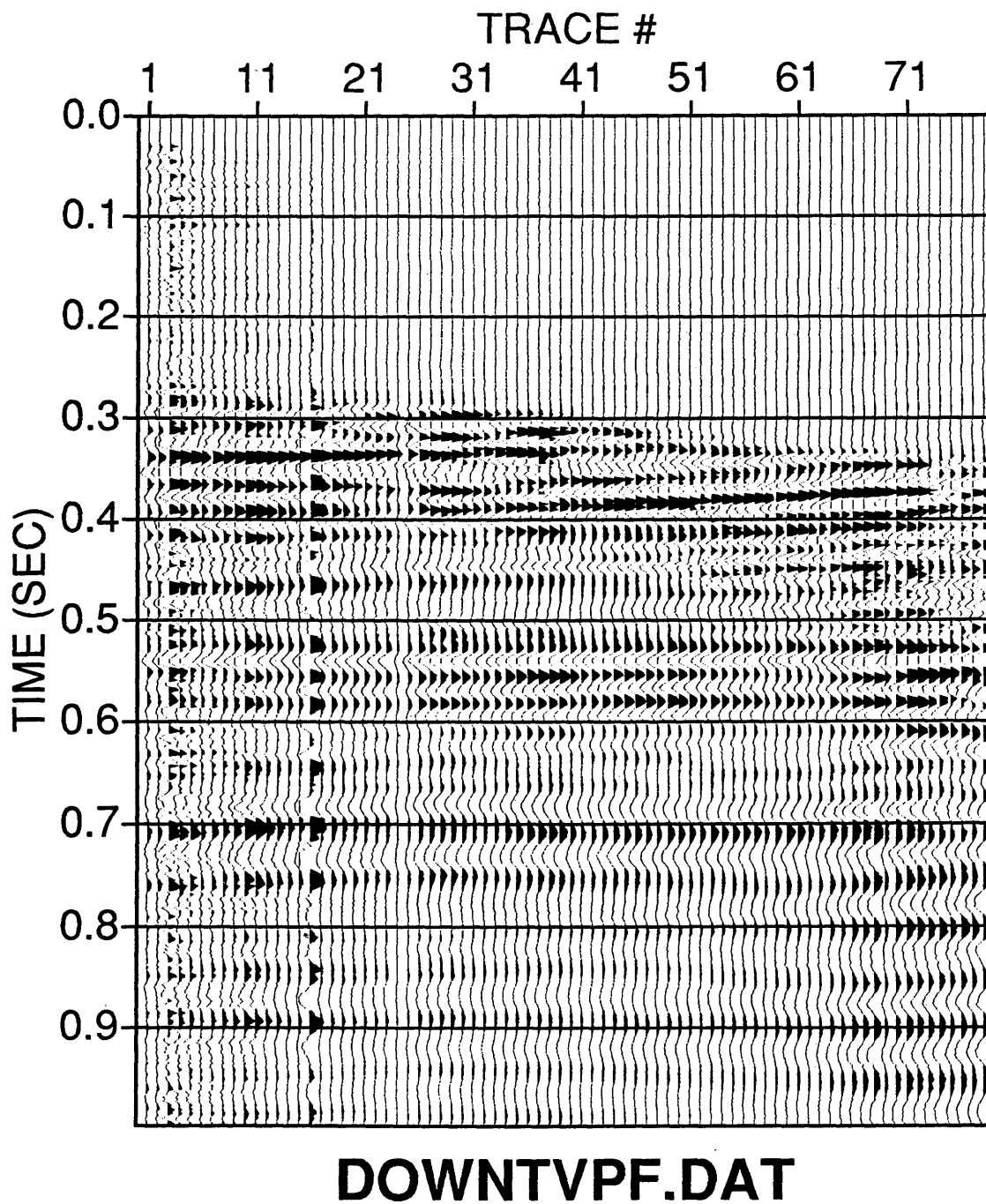
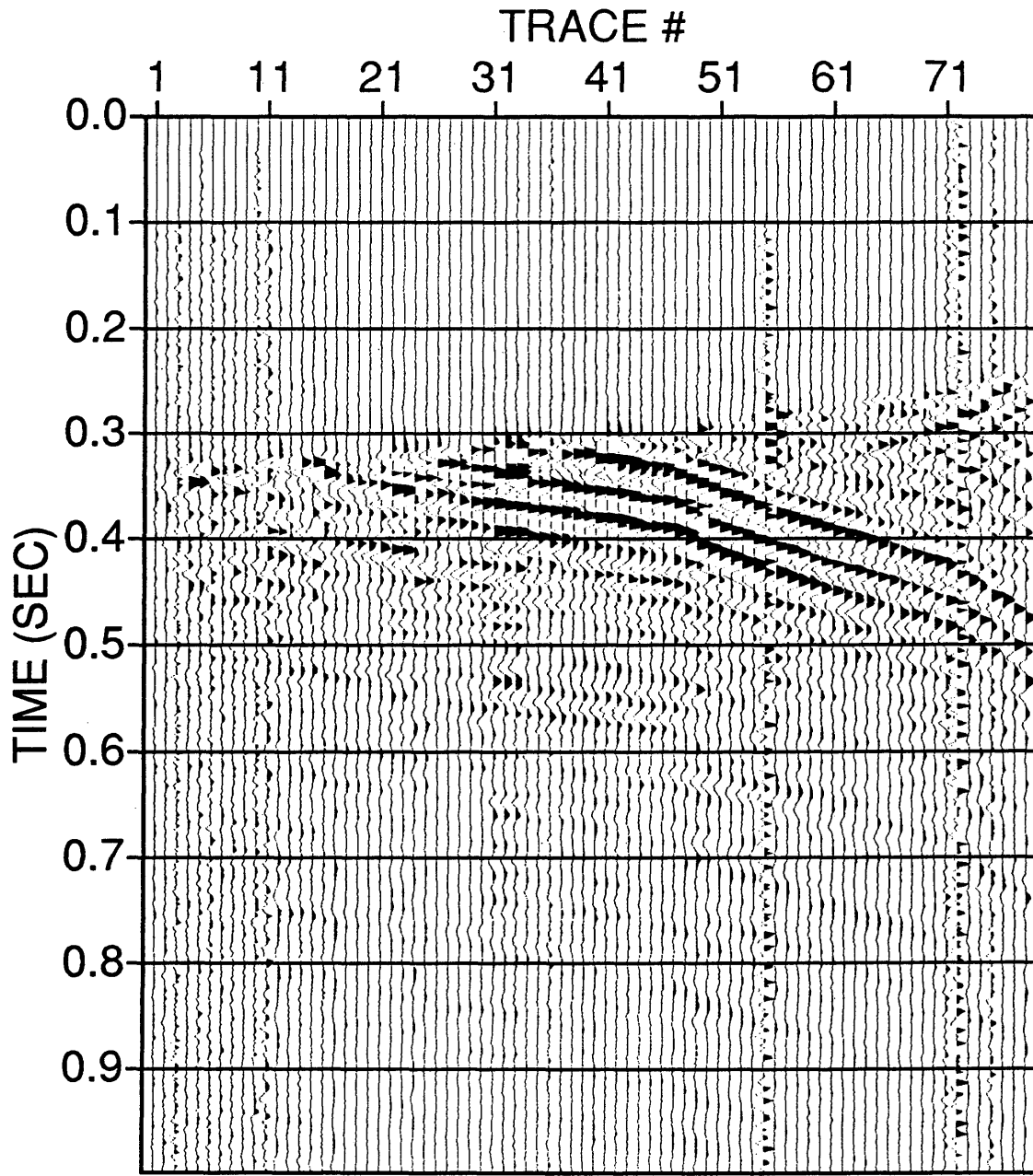


Figure 52: Down-going SV data computed by median filtering of the crossline component (TVPF).



UPOVPF.DAT

Figure 53: Results after subtraction of the down-going P-wave energy from the pre-median filtered OVPF data, (contains up-going P and SV energy).

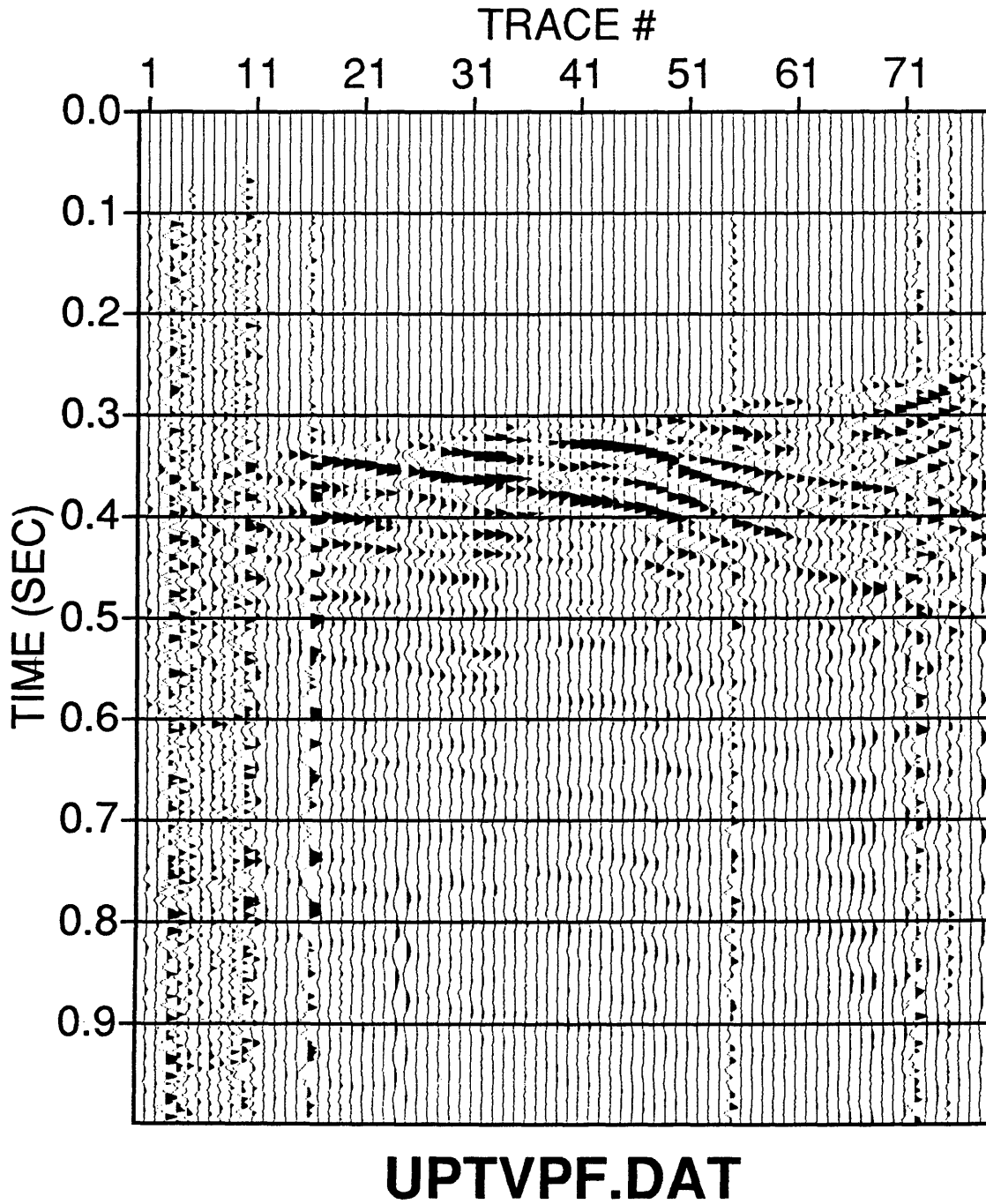


Figure 54: Results after subtraction of the down-going SV energy from the pre-median filtered TVPF data, (contains up-going P and SV energy).

the depths, velocities, densities, and VP\VS ratio for each layer.

Table II: Velocity model used for the raytracing program in order to calculate the time variant angles. Depth is in feet and velocity is in feet/sec. * indicates coal stringers.

Layer	Top Depth	Bottom Depth	Top Velocity	Bottom Velocity	Density	VP\VS
1	0	450	3000	9000	2.50	2.00
2	450	1600	11000	11000	2.25	2.06
3	1600	2113	12000	12000	2.45	1.53
4	2113	2450	13500	13500	2.52	1.56
5	2450	2650	10000	10000	2.33	1.85
6*	2650	2680	7700	7700	1.96	2.13
7	2680	2750	10000	10000	2.51	1.89
8*	2750	2770	7800	7800	2.32	1.90
9	2770	2815	11000	11000	2.48	1.72
10*	2815	2825	8000	8000	2.08	1.54
11	2825	2865	11000	11000	2.53	1.69
12*	2865	2885	8000	8000	1.60	1.89
13	2885	2965	11000	11000	2.62	1.61
14	2965	3500	12000	12000	2.50	1.60

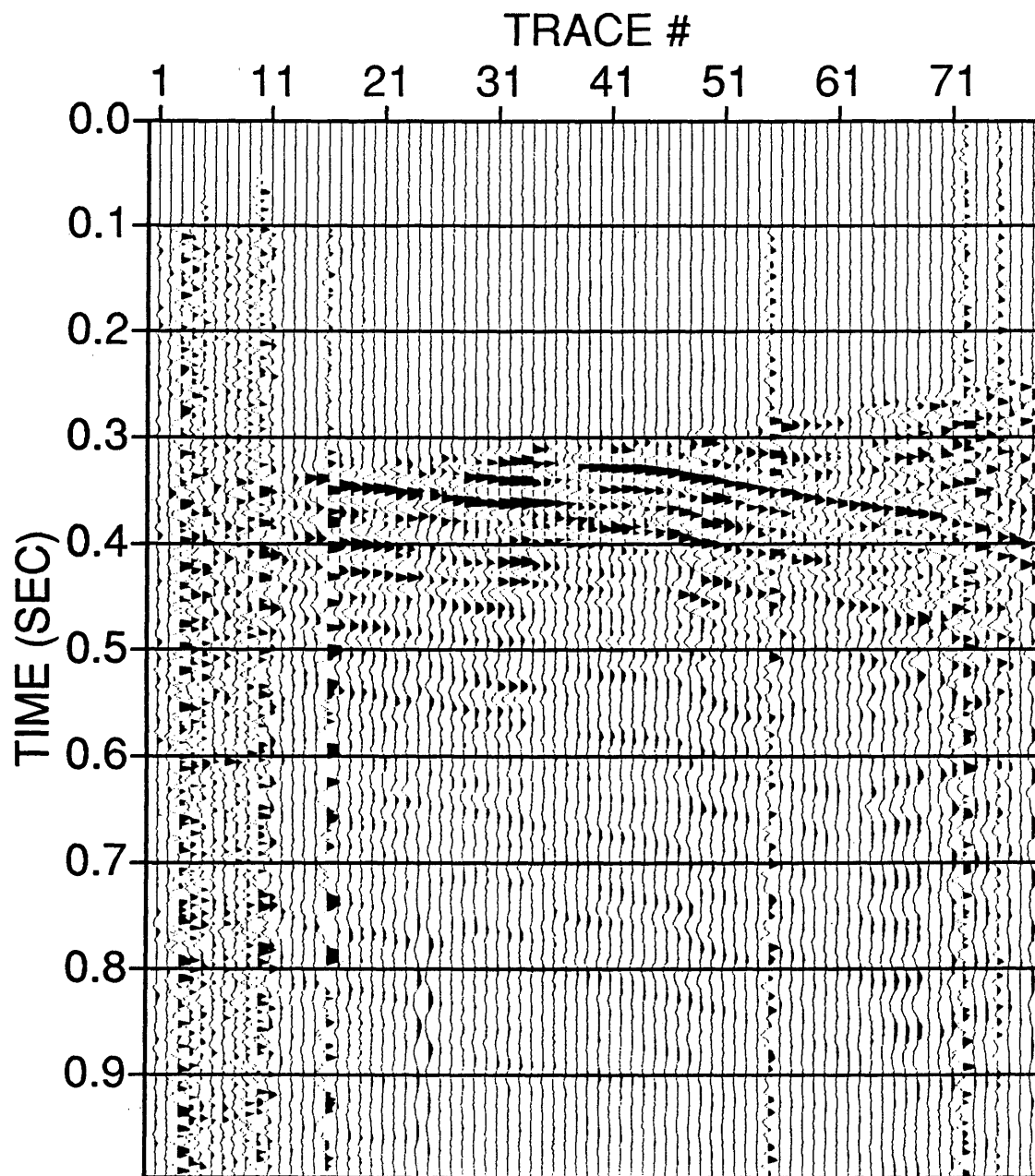
After finding the time varying angles, they were applied to the two upgoing data sets (OVPF.UPG and TVPF.UPG) using the following formulas:

$$P.UPG = OVPF.UPG(t, d) \cos[\phi(t, d)] - TVPF.UPG(t, d) \sin[\phi(t, d)]$$

$$SV.UPG = OVPF.UPG(t, d) \sin[\phi(t, d)] + TVPF.UPG(t, d) \cos[\phi(t, d)]$$

where $\phi(t, d)$ are the time varying angles. The results of the upgoing P and SV energy are displayed in Figures 55 and 56. (P.UPG and SV.UPG, respectively)

Due to the multiples seen in the down-going P-wave energy



P-WAVE.DAT

Figure 55: Up-going compressional energy after time-variant orientation.

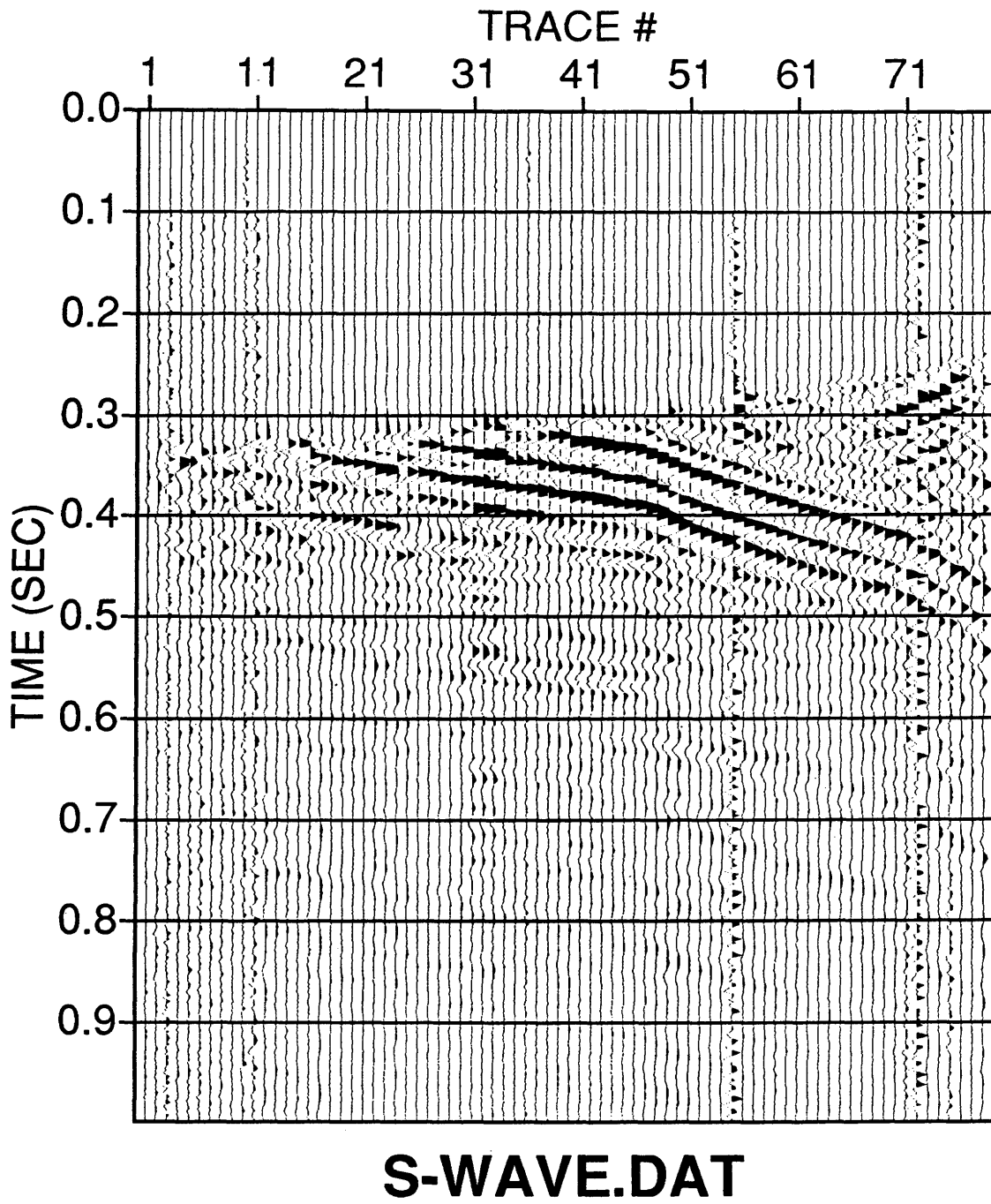


Figure 56: Up-going SV energy after time-variant orientation.

(Figure 51), an inverse shaping filter was designed to collapse the data into a 10(12) - 100(36) Hz(dB/Oct) zero phase wavelet. The result is displayed in Figure 57. The inverse shaping filter designed on the down-going energy was then applied to the up-going P and SV data to suppress the multiples. The deconvolved data sets are shown in Figures 58 and 59. This was then followed by a spherical divergence correction to the up-going wavefield.

In dealing with far-offset data, a normal moveout correction is essential. The NMO correction uses Rms velocities calculated from the first arrival times and depths in the traces headers and shot receiver offsets calculated from coordinates in the headers. Following NMO, the P and SV data were flattened on the upgoing energy and a 12 point median filter was applied in order to enhance the reflecting events. Figures 60 and 61 show the results after NMO and median filtering.

Finally, a horizontal moveout correction was applied to both data sets. This included computing offset positions for each time sample of each trace and moving them to their offset reflection points. The final results are displayed in Figures 62 and 63.

The far-offset P-wave data (Figure 62) show good resolution of the coals in interval II, but poor resolution in

the coals contained within interval IV. Also, the data show a slight west dip in the coals, possibly due to draping of the coals caused by underlying channel sands (Johnson, 1991). The data has not been migrated, therefore the dip might be steeper than it actually appears on Figure 62. The far-offset converted shear-wave data (Figure 63) show good resolution of the coals in interval II and IV with a slight dip towards the west. In comparing the P-wave and converted S-wave data, the S-wave data tends to show a higher resolution of the coals within interval IV. This is easily explained by the fact that wavelength determines the resolution. The S-wave data travels at a slower velocity than the P-wave data, thus the shear-wave data has a shorter wavelength than the P-wave data.

The far-offset data profile was located at an azimuth 263 degrees from North, therefore almost parallel to the P-wave seismic section shown in Figure 16. In looking at the data west of the well, there is a slight west dip in the interval II coals which was also seen in the far-offset P-wave data. (Figure 62)

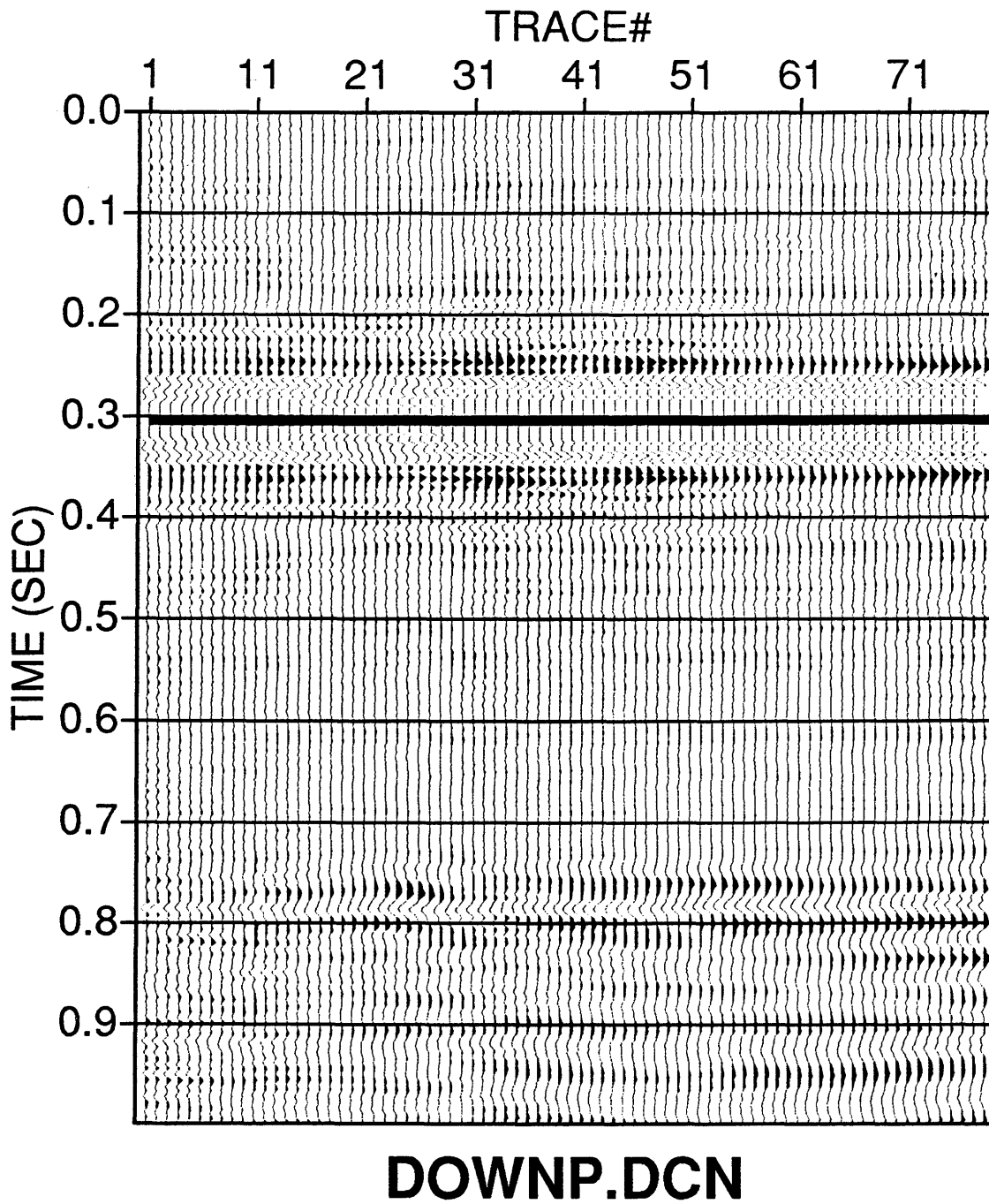


Figure 57: Results of the down-going energy after applying the 10(24) - 100(36) Hz (dB/Oct) wavelet shaping filter to collapse the multiples.

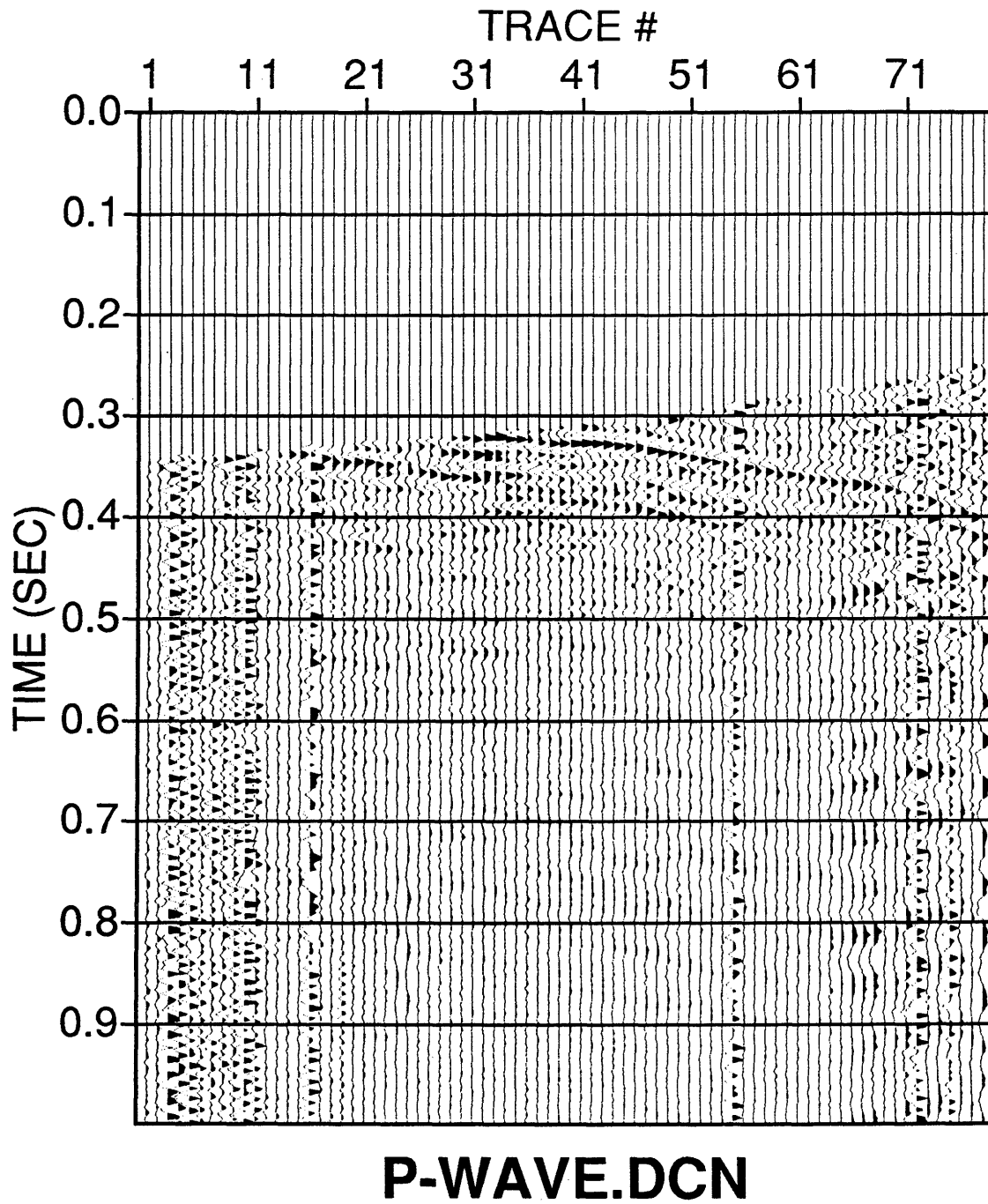
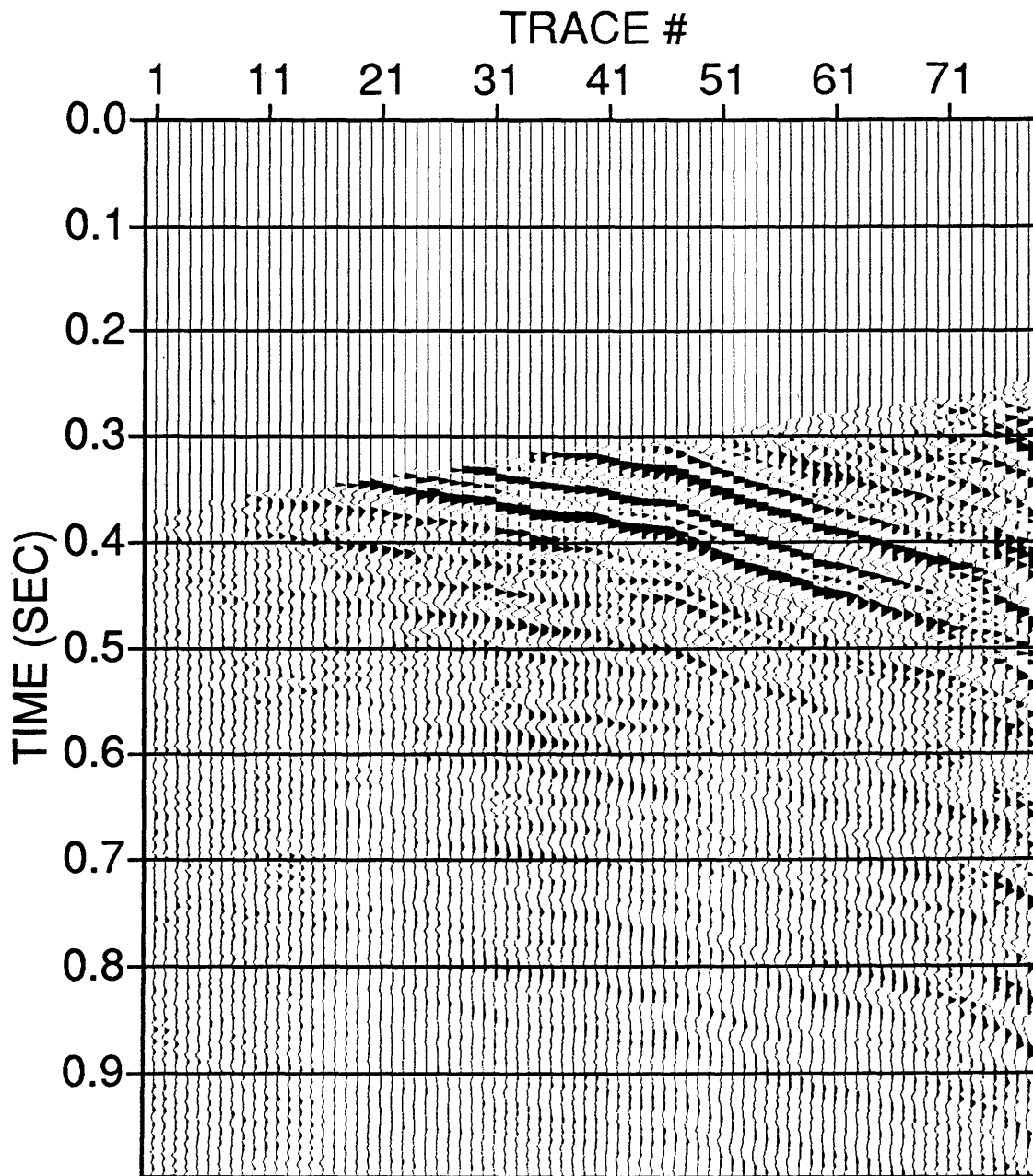


Figure 58: Results of the up-going P-wave energy after applying the 10(24) - 100(36) Hz (dB/Oct) wavelet shaping filter designed on the down-going energy.



S-WAVE.DCN

Figure 59: Results of the up-going SV-wave energy after applying the 10(24) - 100(36) Hz (dB/Oct) wavelet shaping filter designed on the down-going energy.

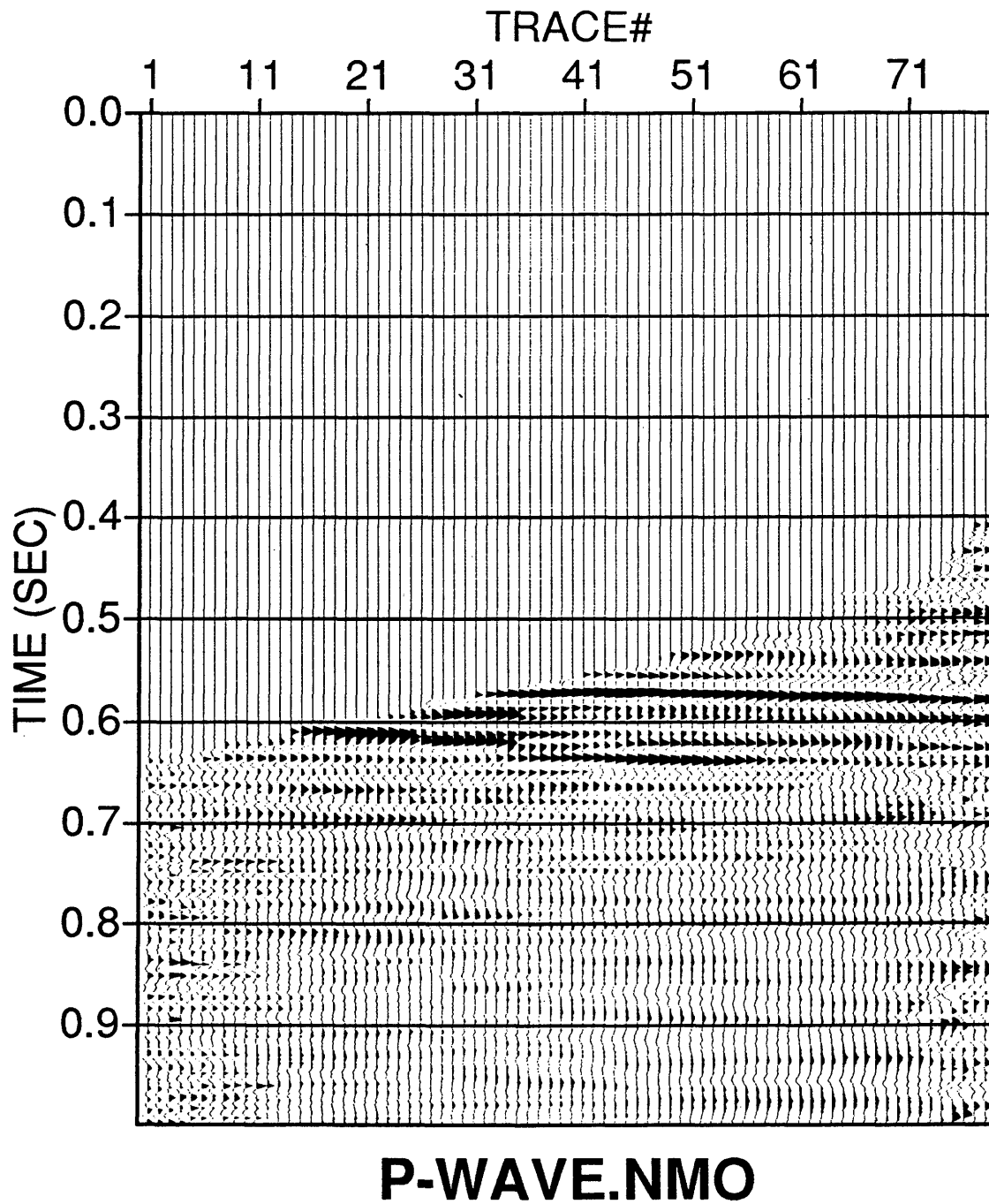


Figure 60: Results of the P-wave data after NMO correction and median filtering.

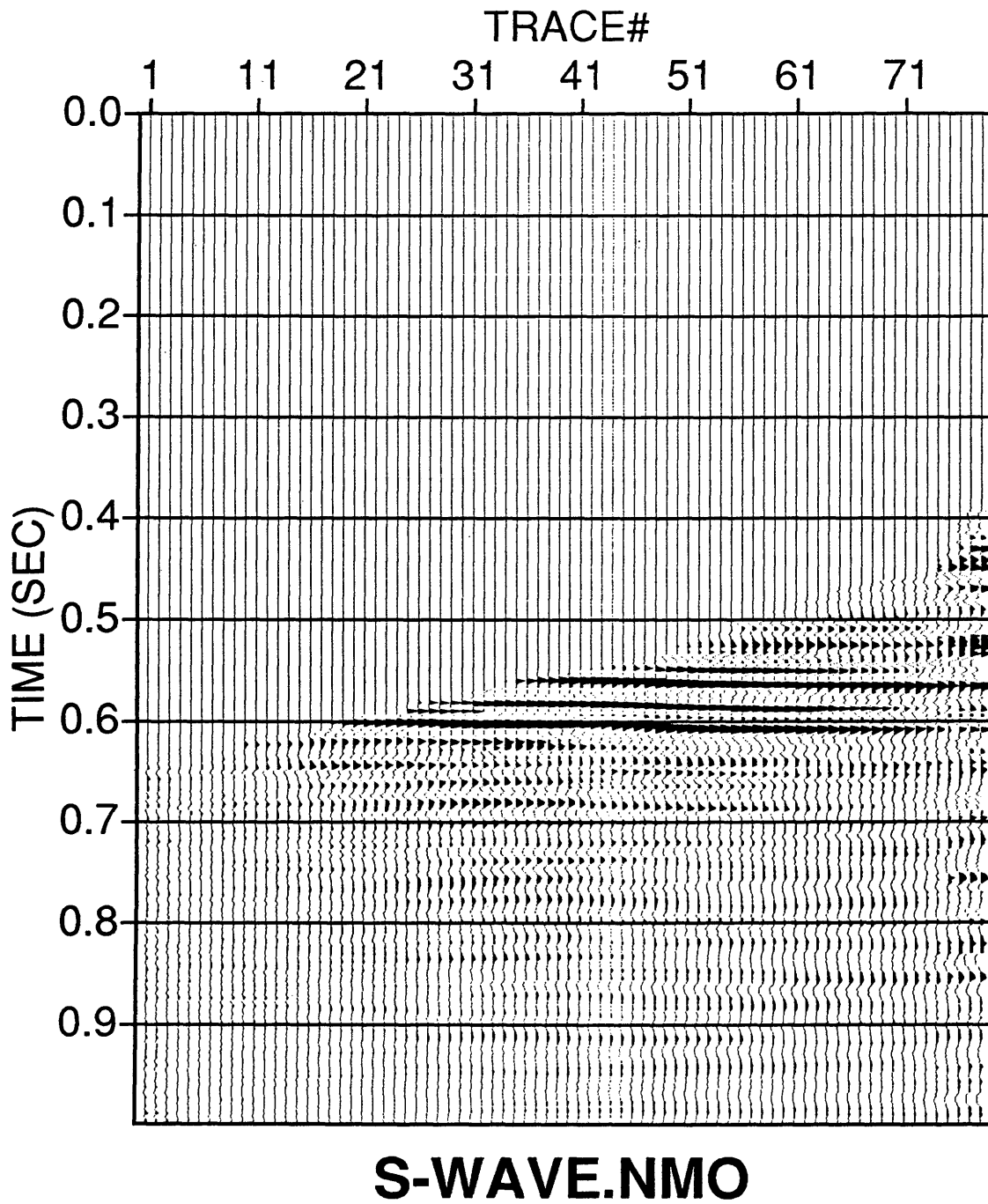


Figure 61: Results of the SV data after NMO correction and median filtering.

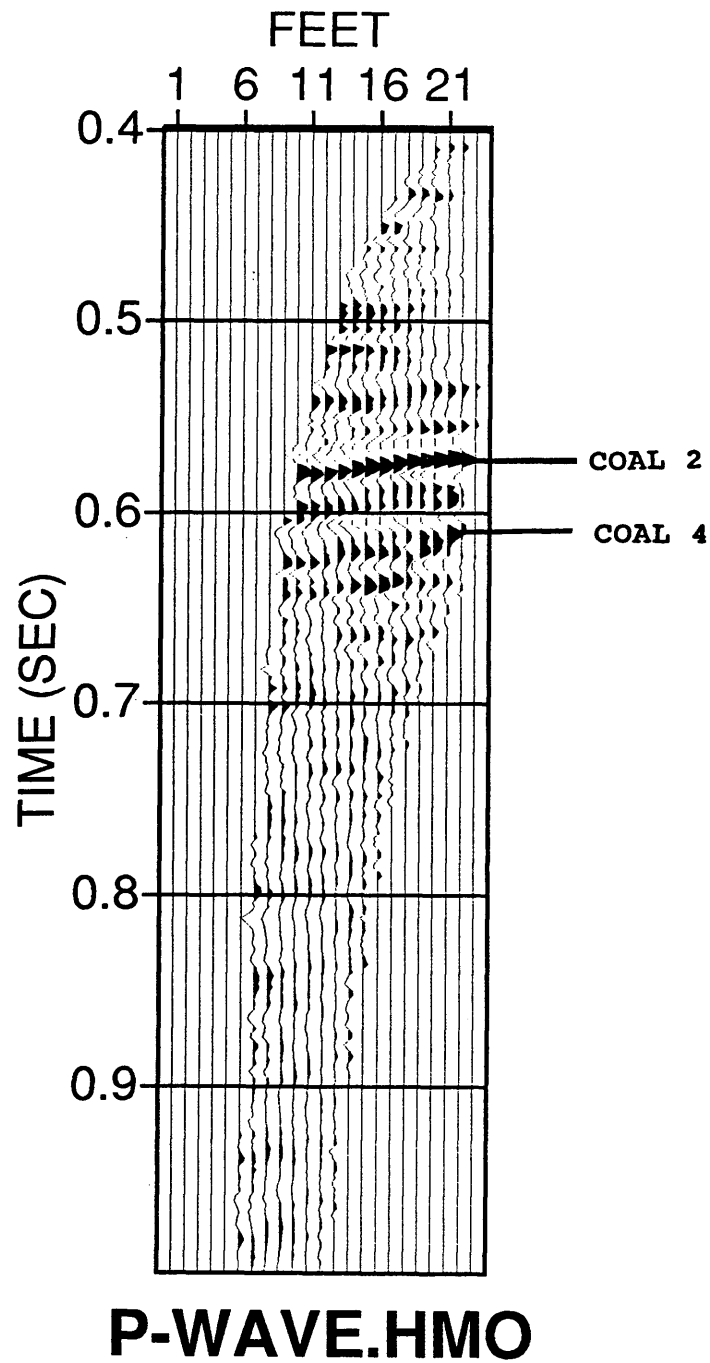


Figure 62: Final results of the P-wave data after horizontal moveout correction.

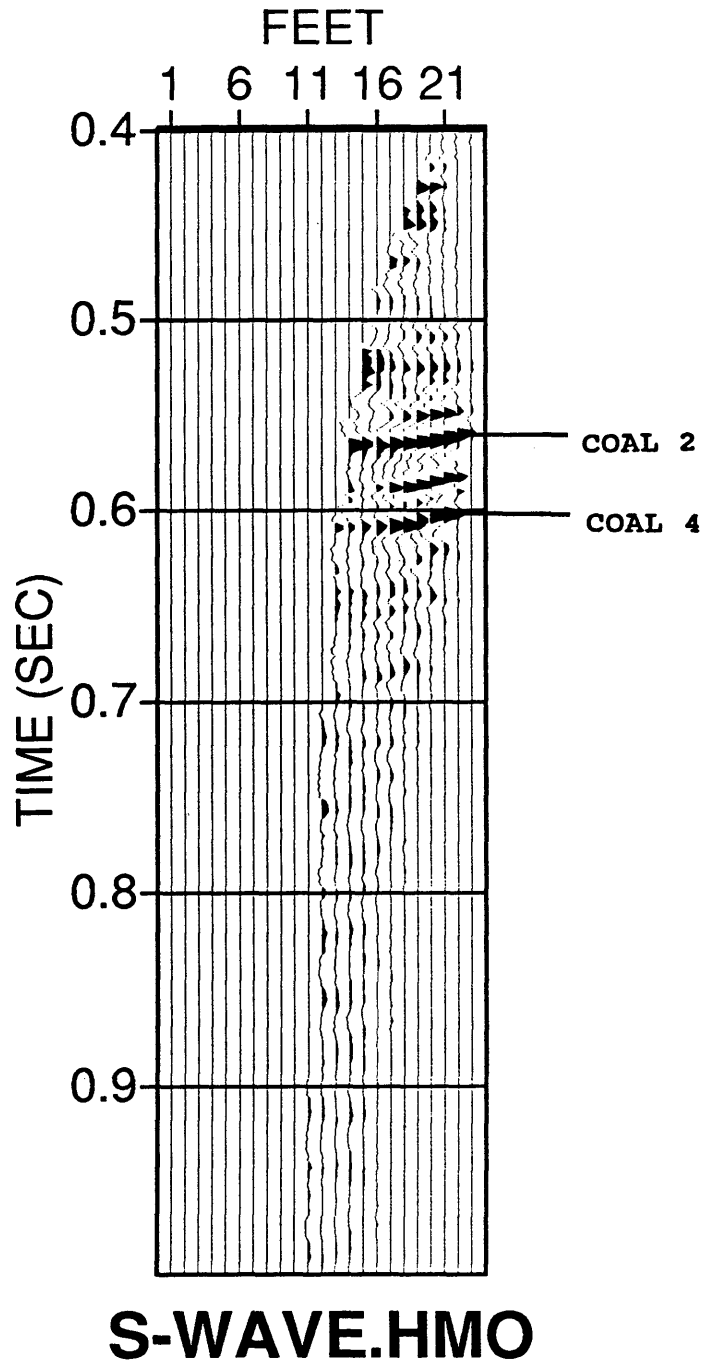


Figure 63: Final results of the converted S-wave data after horizontal moveout correction.

FUTURE STUDIES

The fast shear-wave data indicated a natural polarization direction parallel to the butt cleats. However, this polarization angle can be a result of either the fracturing in the rock or an indication of the local stress. Measurements would need to be made to determine local stress and see if it differs from the principal regional stress that caused the fractures.

The amplitudes within the coals can easily be preserved due to a weak anisotropic medium above the coal. This facilitates the interpretation of amplitude variation in the S2 component due to fracture intensity. Also, due to thin bed anisotropy in the coal beds, measuring attenuation could provide insight into the fracture intensity. Both of these tools, amplitude and attenuation, could be helpful in the interpretation of the multicomponent 3-D survey in the Cedar Hills Field.

The area examined for study was limited to coal bed methane formations in the Cedar Hills Field. Other coal bed methane fields worldwide containing complex fracturing should be tested in determining the validity of this method. Also, this technique could be applied to environmental problems, such as injecting toxic waste material into fractured salts.

CONCLUSIONS

Multicomponent VSPs assisted in the characterization of methane producing coal beds in the Fruitland Formation, Cedar Hill Field. Analysis of the VSPs gave the following results:

1. The near-offset P-wave corridor stack resolved two major coal beds, intervals 2 and 4 observed on the high resolution density log. These coals are greater than 16 feet in thickness. The thinner coal beds are incoherent due to interference in wave form.
2. The P-wave stack and the surface seismic data show a good correlation in the coal intervals, 2 and 4, within the Cretaceous Fruitland Formation.
3. Shear-wave birefringence was observed on the near-offset shear-wave data. Through rotation of these data, a natural polarization angle was estimated at 319 degrees from North or N41W. This angle parallels the butt cleat direction found within the Hamilton #3 well. Also, production trends, structure at the base of the Basal Fruitland Formation, and present day tectonic information

supports a northwest open fracture orientation.

4. Through the process of layer stripping, it was determined that the fractures within the coals is at the same orientation as the fracturing detected at the near-surface.
5. The corridor stacks of the fast (S1) and slow (S2) shear wave data correlate very well in the coal intervals, 2 and 4, with an approximate two-way time delay of 20 msec.
6. The S2 corridor stack has a slightly higher amplitude than S1. Amplitude anomalies in the S2 component could facilitate finding lateral variation in fracture intensity in the coal beds when interpreting the 3-C 3-D seismic survey.
7. The processing of the far-offset data gave a good comparison between the up-going P-wave and converted S-wave data. The converted S-wave data showed a higher resolution in coal interval IV than the P-wave data and offers hope for the utilization of converted shear wave data in this project.

8. A slight west dip is seen on the far-offset VSP and on the surface P-wave data. The dip is possibly a result of draping of the coals caused by underlying channel bodies.

In conclusion, multicomponent VSPs were useful in measuring shear-wave birefringence in the Cedar Hill Field, which in turn helps to determine a fracture orientation in the subsurface. By knowing this information, better enhanced recovery programs can be developed in the future.

REFERENCES

- Ambrose, W.A., and Ayers, W.B., 1991, Geologic controls on coalbed methane occurrence and producibility in the Fruitland Formation, Cedar Hill Field and Coal site, San Juan Basin, Colorado and New Mexico: Rocky Mountain Association of Geologists, 227-240.
- Balch, A.H., Lee, M.W., Miller, J.J. and Taylor, R.T., 1982, The use of vertical seismic profiles in seismic investigation of the earth: Geophysics, 47, 906-918.
- Balch, A.H. and Lee, M.W., 1984, Vertical Seismic Profiling: Techniques, Applications, and Case Histories, published by the International Human Resources Development Corporation, Boston.
- Carswell, Allan and Moon, Woil M., 1989, Application of multioffset vertical seismic profiling in fracture mapping: Geophysical Journal, 96, 65-83.
- Crampin, Stuart, Chesnokov, Eugenie M., and Hipkin, Rodger G., 1984, Seismic anisotropy - the state of the art: II.: Geophysical journal of the Royal Astronomical Society, 76, 1-15.
- Crampin, Stuart, 1984, An introduction to wave propagation in anisotropic media: Geophysical Journal of the Royal Astronomical Society, 76, 17-28.
- Crampin, Stuart, 1985, Evaluation of anisotropy by shear-wave splitting: Geophysics, 50, 142-152.
- Davis, Thomas L., and Lewis, Catherine, 1990, Reservoir characterization by 3-D, 3-C seismic imaging, Silo field, Wyoming: Geophysics: The Leading Edge of Exploration, 9, 22-25.
- Decker, A.D., Jeu, S.J., Cooper, J.D., and Wicks, D.E., 1988, Geology, geochemistry, reservoir engineering, and completion methods at the Cedar Hill Field, San Juan County, New Mexico-A field study of classic coal degasification behavior, in Fassett, J.E., ed., Geology and coal-bed methane resources of the northern San Juan basin, Colorado and New Mexico: Rocky Mountain Association of Geologists Guidebook, 221-235.

- Decker, David A., Close, Jay C., and McBane, Richard A., 1989, The use of remote sensing, curvature analysis and coal petrology as indicators of higher coal reservoir permeability: proceeding of the 1989 Coal bed Methane Symposium, The University of Alabama/Tuscaloosa, Alabama.
- DiSiena, James P., Gaiser, James E., and Corrigan, D., 1981, Three-component vertical seismic profile: Orientation of horizontal components for shear wave analysis: Presented at the 51st Annual International SEG Meeting, Los Angeles, Expanded Abstracts.
- Gal'perin, E.I., 1974, Vertical seismic profiling, SEG special publication No.12, Tulsa, Ok.
- Gas Research Institute Topical Report, 1989, Western Cretaceous coal seam project: Evaluation of the cooperative research well Hamilton #3, unpublished report.
- Humphrey, J.R., and Wong, I.G., 1989, Contemporary seismicity, faulting, and the state of stress in the Colorado plateau: Geological Society of American Bulletin, 101, 1127-1146.
- Johnson, R.D., 1991, The control of structure and stratigraphy on differential compaction of the Fruitland coal bearing intervals, Cedar Hill Field, San Juan County, New Mexico: Masters thesis T-4095, Colorado School of Mines, Golden, Colorado.
- Kramer, D.K., 1991, Multicomponent vertical seismic profiles for reservoir characterization, South Casper Creek Field, Natrona County, Wyoming; Ph.D. thesis T-3939, Colorado School of Mines, Golden, Colorado.
- Kramer, D.K., 1991, Three-component Vsp investigation in coal bed methane formations, Cedar Hill Area, New Mexico: Presented at the Reservoir Characterization Meeting, April 12, Golden, Colorado.
- Martin, Marshall A., 1987, Three-component seismic investigation of a fractured reservoir, Silo Field, Wyoming, Ph.D. Thesis, Colorado School of Mines, T-3339.

- Martin, Marshall A. and Davis, Thomas L., 1987, Shear-wave birefringence: A new tool for evaluating fractured reservoirs: Geophysics, The Leading Edge of Exploration, 6,22-28.
- Mueller, M.C.,1992, Seismic Interpretation 33: Using shear waves to predict lateral variability in vertical fracture intensity: Geophysics, The Leading Edge of Exploration, 11,29-35.
- Naville, Charles, and Crampin,Stuart,1986, Detection of anisotropy using shear-wave splitting in VSP surveys: Requirements and applications: Presented at the 56th Annual International SEG Meeting,Houston,Expanded Abstracts, 1133-530.
- O'Rourke, T.J.,1986, Shear and compressional analysis of Vsp in Silo Field,Denver Julesburg Basin: Masters thesis T-3198, Colorado School of Mines, Golden, Colorado.
- TerraTek Core Services,1988, Fracture analysis of cores from Mesa Petroleum Ltd.'s hamilton No.3 Well,unpublished report, TTCS file No.88730.
- Way, S.C., Hydrologic characterization of coal seams for optimal dewatering and methane from coal seams Technology 4,42-43.
- White, J.E., and Sengbush, R.L., 1983, Underground sound: Elsevier Scientific Publications,New York.
- Winterstein, D.F., and Meadows, M.A.,1990, Shear-wave polarization and subsurface stress directions at Lost Hills Field: Expanded Abstracts, 60th Annual International SEG meeting, San Francisco, California, pp 1431-1434.